博士論文

High-Speed and Reliable Indoor Communication System by Two-Dimensional Communication Tile

（二次元通信タイルによる高速・高信頼な屋内通信システム）

岡田　明正

Abstract

In this thesis, we propose an indoor communication system by a two-dimensional communication (2DC) tile. This system enables a high-speed and reliable communication with ultra-wideband (UWB) signals. Moreover, device positioning with high-accuracy is feasible by utilizing the physical characteristic of the system. This system addresses the issue on the establishment of an indoor communication system due to increase of the number of communication devices and growing demand of applications like device-control and presentation of information based on the position.

This thesis contains three contents on the establishment of the tile system and one content on the position detect. First, the concept of the 2DC tile system is proposed as a method for extension of a 2DC area and the feasibility of the system is verified. This tile is typically 50-cm square that is a standard carpet size, and includes a sheet-like waveguide called a 2DC sheet and some electrical components. The system is established by connecting the tiles with non-contact manner. Standing waves generated in the tile heightens a signal-to-noise ratio (SNR) and this property enables stable communication even with low transmission power of the UWB radio that is available of a few GHz bandwidth. Preliminary experiments show that a sufficient margin to the thermal noise is ensured in the bandwidth more than 80% over the UWB high-band at six measurement points.

Then, a delay and a SNR in the tile, which are essential properties to design a physical layer protocol, are modeled and evaluated. A signal propagation model based on the geographic property of the sheet is proposed and is well matched to electromagnetic simulations. The results of measurements with a single tile show that a root-mean-square (RMS) delay spread is less than 5.76 s in 80% of the sheet area and SNR is more than 20 dB at all the single sheet area. A RMS delay spread value of the entire system where multiple tiles are connected is also modeled. The model discloses that the delay spread of the entire system is 1.4 times longer than that of a single tile regardless of the system size. Thus the delay spread value of the tile system is at most 8 ns, which is smaller than that of aerial communication under the condition of the same propagation area.

A suppression method of radiation from the 2DC sheet is presented as the final content on the establishment of the tile system. Unlike an infinite length sheet, radiation into space is generated in the case of a finite length sheet. Suppressing the radiation enables the tile system to achieve reliable communication for safety-critical applications for example, factory automation. From the radiation model, magnetic field at far-field zone corresponds to a Fourier transform of an amplitude of an electric-evanescent field. A smooth transition of the electric field yields suppression of the radiation. Two transition patterns are examined and a cosine-shape transition whose length is 100 mm results in 30-dB suppression.

The positioning method with the tile system utilizes the physical property that the tile system consists of multiple separated units. Distinguishing the tile where a device is put on achieves the position detection with the accuracy of the inverse of square root of a tile length. The preliminary experiment is conducted to verify the principle and the device position is successfully detected.

These results indicate that the 2DC tile system achieves high-speed and reliable communication with high-accuracy position detection.

Contents

Chapter 1

Introduction

1.1 Indoor communication system

1.1.1 Present communication technologies in an indoor environment

A communication technology enables people that are apart to easily communicate with each other by transmitting information as electric signals. In 2014, communication data traffic reached about 14.5 EB (1E=10^{18}) [1] that is 9 times in 9 years. This fact indicates that the communication technology is indispensable to modern daily life. Development of the communication technology enables a large amount of data like video data to be transferred in a short time and popularization of communication devices increases its frequency. In addition to human-to-human communication, machine-to-machine one in a sensor network and Internet of Things (IoT) has been increasing and yielding valuable information with a high-performance computer.

Applications with the sensor network and IoT, for example building monitoring, appliance control depending on person movement, temperature control with ambient information, and so on, are expected to provide more convenient and safe environment especially in an indoor environment where people spend much time with work or living. One of key enablers of such applications is establishment of a communication system among devices. The applications require deploying devices densely across a wide area. In practice using wireless communication is the realistic way instead of wiring one.

At the present, representative schemes of the wireless technologies used in an indoor environment are IEEE 802.11 and IEEE 802.15. IEEE 802.11 is a standard for wireless local area network (WLAN). The standards, IEEE802.11a/b/g/n, are widespread schemes all over the world. Devices that pass the Wi-Fi alliance interoperability certification test is called as a Wi-Fi product or simply as Wi-Fi [2]. IEEE802.11 standards operate in unlicensed bands, 2.4 GHz and 5GHz: the carrier frequency of IEEE 802.11b/g is 2.4 GHz and that of IEEE 802.11a is 5 GHz. IEEE802.11n operates in both the frequencies. The bandwidth of IEEE 802.11 series is 20MHz except IEEE 802.11n that can also operate in 40MHz with channel bonding technology. Recently IEEE 802.11 ac that enables about 7 GHz has been standardized and products including IEEE 802.11 ac are commercially available.

IEEE 802.15 is a standard for personal area network (PAN). PAN is a network where devices around a person are connected. Its network area is about ten meters while the network of WLAN is available to a range of a few tens meters. Although PAN is established with wired connection like IEEE1394 [3], wireless PAN (WPAN) technology like Bluetooth[4], ZigBee[5], and ultra-wideband (UWB) are more widespread.

The summary of each technology is following.

- Bluetooth

Bluetooth is standardized as IEEE802.15.1 and operates in 2.4 GHz band. A channel bandwidth and maximum data rete are 1 MHz and 24 MHz, respectively. Since the frequency band is the same as that of Wi-Fi, frequency-hopping spread spectrum (FHSS) is implemented in Bluetooth technology to avoid interferences with Wi-Fi. Recently Bluetooth low energy (BLE) that achieves lower power consumption is paid attention as a technology for Internet of Things (IoT).

- ZigBee
  The physical layer and MAC layer of ZigBee is standardized as IEEE802.15.4. ZigBee is mainly expected to be implemented in a sensor network and operates in either 2.4 GHz band or 920MHz band. Its channel bandwidth and maximum data rate are 2 MHz and 250 kbps.

- UWB
  UWB is a promising technology to solve a conjecture of ISM band by allocating such a wideband from 3.1 GHz to 10.6 GHz [6]. In Japan, the spectrum from 3.4 GHz to 4.8 GHz as a low-band and from 7.25 GHz to 10.25 GHz as a high-band is available[7]. The transmission power density is restricted under -41.3dBm/MHz. This transmission power is very small and equivalent to the noise emitted by electrical devices like PCs. Multi-band orthogonal frequency division multiplexing (MB-OFDM) is one of UWB communication schemes and its bandwidth is 500 MHz. Fig. Communication with impulse signal is also one of the schemes. Fig. 1.1 shows the spectrum of UWB and Wi-Fi. The bandwidth of IEEE802.11b/g is 20 MHz and that of IEEE802.11ac that is expected to realize data rate of a few Gbps is 160 MHz. The bandwidth of UWB is much wider than that of IEEE802.11b/g and the UWB device can transmit only 0.5 mW even with bandwidth of 7 GHz while the Wi-Fi device transmits 10 mW with bandwidth of 20 MHz.

A visible light communication (VLC)[8], is also available in an indoor environment. In VLC, light from LEDs is modulated at a very fast rate that a person is unable to perceive, then a receiver demodulates the signals detected by a photodiode. Data rate is up to 96 Mbps in IEEE 802.15.7 standard[9] and a few Gbps is achieved in [10][11]. Since visible light cannot propagate over a wall or floor, range where light can reach is considered as a communication channel. Therefore, VLC creates geographically independent channels .

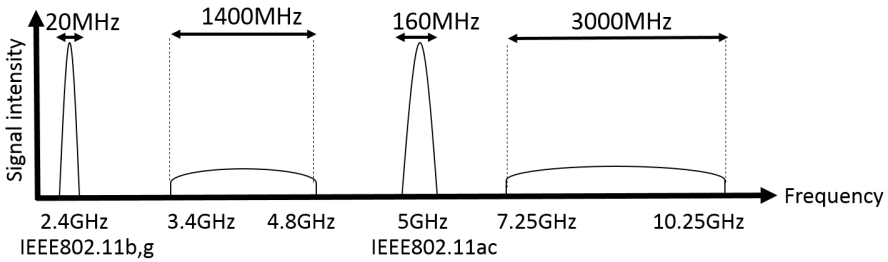

Fig. 1.1. Spectrum of UWB and IEEE802.11. In UWB, the wider bandwidth is available while transmission power density is restricted under -41.3 dBm/MHz. In Wi-Fi, the bandwidth is narrower while the transmission power is much bigger than UWB.

1.1.2 Issues of the indoor communication system

A large number of devices, which are deployed densely bring disadvantages to a network. In the ISM band, the allocated spectrum is so narrow that interferences among devices easily occur and data rate is decreased.

The interferences also decrease reliability of a network. Reliability is an important factor especially for safety critical application like an industry-related one[12]-[18]. As industry 4.0 [19] and industrial network [20] have been proposed, many devices are expected to be connected to a network. At the present, devices are connected with cables whose connection enables a reliable network in factories. However, since connecting a large number of devices with cables will suffer from cost and difficulty in implementation and maintenance, wireless connection are demanded in factories.

Therefore, the requirements of indoor communication system is to overcome the shortage of the bandwidth and achieve a high-speed and reliable network.

1.2 UWB two-dimensional communication

As mentioned above, the UWB radio has a potential to solve the shortage of a bandwidth with such a wide bandwidth. On the other hand, the restricted transmission power causes an unstable connection. "UWB two-dimensional communication (2DC)", which is focused on in this thesis, has been proposed in [21] to solve the physical connection problem and is a combination of UWB radio and 2DC technology, which enables a two-dimensional network, not either wired or wireless network. In this section, a classification of networking technologies is described from the viewpoint of signal-propagation dimension to introduce two-dimensional network then the summary of the 2DC and properties of UWB 2DC are presented.

1.2.1 Classification of networking technologies from the viewpoint of signal-propagation dimension

There are many technologies for the data link layer of the OSI reference model, with which devices in an identical network are connected, for example Ethernet and IEEE 802.11 series. These technologies can be classified from the viewpoint of signal propagation dimension as shown in Fig. 1.2. Since signals propagate along a cable in a wired network like Ethernet, this kind of technologies are considered as one-dimensional communication whereas wireless communication is classified as three-dimensional communication because signals propagate in the space.

Although one or three dimensional communication are widespread, communication where signals propagate in a two-dimensional plane as shown in Fig. 1.3 is also possible. Characteristics of two-dimensional communication are considered in the following: signals propagate in a sheet-like medium; devices are connected to the network when they touch anywhere on the medium although implementation of the medium is necessary. Since signals are not emitted into space, interception of communication is difficult and no interferences with aerial radio signals occur. Communication with two-dimensional signal propagation has intermediate properties of both the wired and wireless communication.

In this thesis, we focus on two-dimensional communication (2DC) [22] that is one of the communication technologies with two-dimensional signal propagation. The brief summary of the 2DC is described in 1.2.2 and other technologies are introduced in 1.4.2.

1.2.2 Two-dimensional communication

In the 2DC, signals propagate in a sheet-like waveguide called a 2DC sheet as shown in Fig. 1.4. Although the 2DC sheet is a kind of a surface waveguide[30][31], its structure is similar to a parallel plate waveguide (PPW). The sheet consists of three layers: an inductive layer with a conductive mesh, a dielectric layer, and a ground layer. The guided EM wave is also similar to the PPW guided mode. Fig. 1.5 shows the microwave propagation in the vicinity of the sheet. The lowest order transverse magnetic (TM) mode wave propagates inside the sheet. Most energy is localized in the sheet and an evanescent field is generated above the sheet when a signal wavelength is shorter than the mesh pitch. The connection between a device and the sheet is established via a specialized coupler that is embedded in the device. This coupler is put on the sheet to transmits/receives signals to/from the sheet by proximity connection as shown in Fig. 1.6.

The characteristics of the 2DC are following

- Easy access to a network
- High immunity against signals in the midair
- Availability of both signal transmission and power transmission[26]
- Secure communication

Table 1.1 shows the characteristics of three communication forms except those described in 1.2.1, although the evaluation is subjective and rough. The 2DC has the intermediate characteristics of both wired and wireless communication.

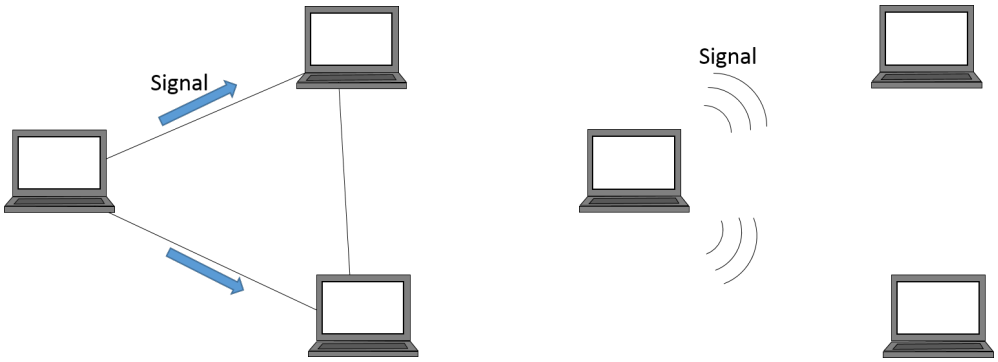

Fig. 1.2. Conventional communication form regarding signal propagation dimension. (a). One dimensional communication (wired network). (b). Three dimensional communication (wireless network).

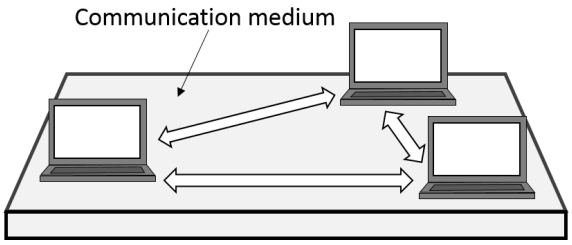

Fig. 1.3. Concept of communication with two-dimensional signal propagation.

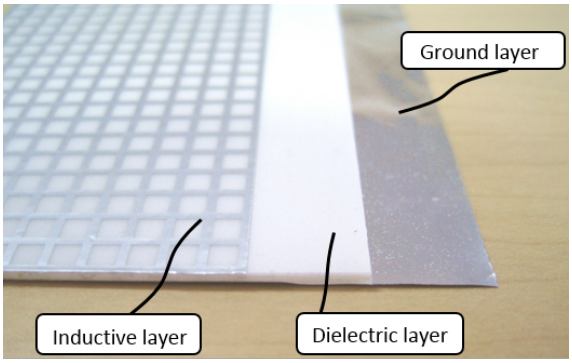

Fig. 1.4. Photo of a two-dimensional communication (2DC) sheet. Its structure is similar to a parallel plate waveguide and consists of three layers: an inductive layer, a dielectric layer, and a ground layer. The inductive layer has a mesh structure.

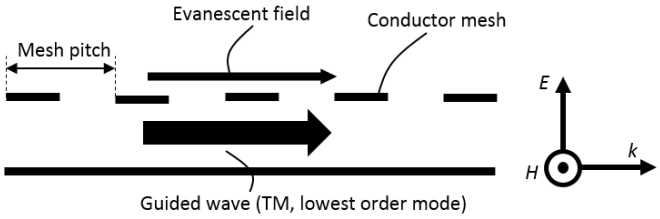

Fig. 1.5. Microwave propagation in the vicinity of the sheet. The microwave propagates as the lowest order mode TM wave in the sheet and an evanescent field is generated above the sheet.

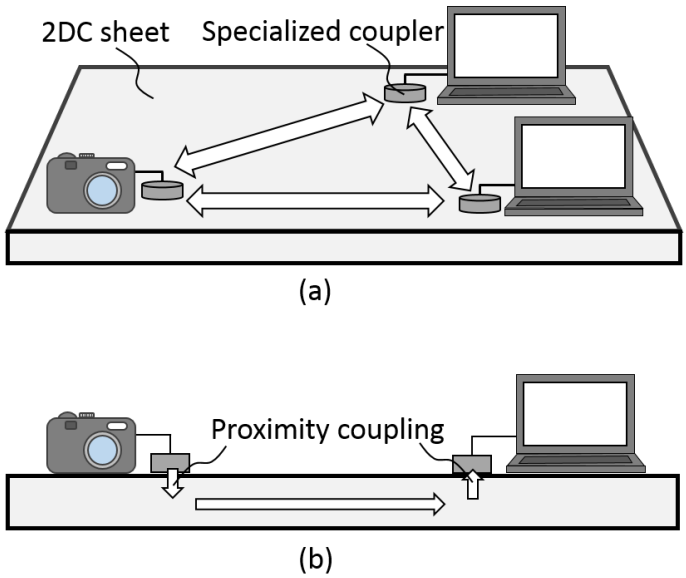

Fig. 1.6. Concept of the 2DC. Devices put on the 2DC sheet connected via a specialized coupler that is embedded to them. The sheet and the coupler are coupling with proximity connection. The connection is kept everywhere on the sheet. (a). Overall view. (b). Cross-sectional view.

Table 1.1. Comparison of the three communication forms

	Wired network	2DC network	Wireless network
Data rate	High	Mid	Mid
Available bandwidth	High	Mid	Low
Power consumption	Low	Mid	High
Immunity	High	Mid	Low
Communication path redundancy	Low	Mid	High

1.2.3 History of two-dimensional communication

Originally 2DC is aimed at a robot skin, in which many sensors are included and form a network [23]. The development of 2DC was started by connecting pieces of conductive fabric with a specialized IC chip, which is called "cell bridge system" [24]. However, extending the network area is difficult because manufacture and implementation of the chips are necessary.

Then, the method using electromagnetic waves has been developed. The principle was ensured with a waveguide that consists of two conductive plates with some halls to stick an adapter [25], then, a waveguide that generates an evanescent field shown in Fig. 1.4 was developed [22].

As mentioned above, one of the characteristics of the 2DC is that the 2DC sheet enables both signal transmission and power transmission. Low-leakage and high-efficiency coupler was developed in [26] and an phased array system to achieve high-efficiency transmission was reported in [27].

Since the 2DC sheet is a kind of a PPW, available bandwidth is wide. A coupler for the UWB band was researched to achieve communication with UWB signals[21]. As an application viewpoint, position detect of a device on the 2DC Sheet was researched in [28][29].

These are the brief history of two-dimensional communication.

1.2.4 Combination of 2DC and UWB

As mentioned in 1.1.1, UWB is a promising technology for an indoor communication due to such a wide bandwidth. UWB, however suffers from the following three connectivity problem.

- Restricted transmission power density under -41.3 dBm/MHz.
- Easy obstruction by general objects in a room
- Interference with aerial narrowband signals

On the other hand, 2DC has the following characteristics that can compensate for the physical connection problems.

- Signals in the sheet are more gradually attenuated than that of free-space propagation.
- A transmitter and a receiver are always in line-of-sight (LOS) as shown in Fig. 1.6(b).
- High immunity against the signal in the air is achieved.

The combination of the 2DC and UWB technology, therefore, has the possibility to achieve the high speed communication with such a wide bandwidth as well as the easy access to the network.

1.3 Goal of the thesis

The goal of the thesis is to propose a method to establish a high-speed and reliable indoor communication system by UWB 2DC. An indoor communication system is required to cover a whole room area. A conventional 2DC is achieved with a desk-top size single sheet. Establishing a room-size network with the single sheet is difficult from the viewpoint of manufacturing, implementation, and maintainability. From the viewpoint of the 2DC history, this thesis establishes the 2DC as a communication technology. Although the principle and the power transmission were ensured, the 2DC has the following restrictions as a communication technology; extension of a networked area, design of a physical layer protocol, and a power management. This thesis will address these restrictions.

Our approach is to establish a communication area by connecting tile-like units called a UWB 2DC tile. Unit-based constitution enables easy implementation and flexible extension of the network area. As a communication technology, signal transmission properties, delay and signal-to-noise ratio is essential to design a physical layer protocol like a modulation scheme and a symbol data rate. Modeling and evaluation of these properties become possible by employing the unit-based architecture and is a part of the goal.

Multiple tiles are implemented in the tile system. This configuration will increase radiation into the air because undesirable emitted energies from each tile [32] are added by the number of the tile. Since this property decreases the immunity against aerial signals and reliability of the system, development of the method to suppress the radiation from the sheet is also a significant purpose of the thesis.

Moreover, position detect of a device, which is strongly demanded to the indoor communication system, is presented. The method utilizing the physical property of the tile system with high accuracy is the goal.

1.4 Related Works

In the thesis, the method to establish a high-speed and reliable communication system with the 2DC UWB is related to the following issues.

- Improvement of physical connection with UWB radio
- Two-dimensional area network technology
- Establishment of a reliable network.

The related works are introduced along the above points.

1.4.1 Improvement of physical connection with UWB radio

The combination of multiple-input multiple-output (MIMO) and UWB is a viable way to compensate for the limitation of the transmission power. In [33], the general framework to characterize the performance of UWB-MIMO system with MB-OFDM is proposed and the advantage of the combination between space-time-frequency coding [34]-[36] and band hopping techniques are shown. In [37], the connectable range at 110 Mbps is extended to approximately a factor of three by using MIMO technology. Some techniques to avoid NBI in indoor UWB communication have been examined. In [38], the effect of NBI is analyzed. The method to detect and mitigate NBI is proposed with compressive sensing

[39] and energy detection [40]. These researches contribute to improve the performance of UWB communication with the assumption that signals propagate in midair.

1.4.2 Two-dimensional area network

In Networked Surface [41], power transmission and communication is conducted by devices touching the surface of metal plates deployed regularly on a two dimensional plane. A position and attitude estimation is also possible by detecting the plate where the device is put. Because this system requires electrical connection between surface pads and devices, corrosion must be prevented.

Pushpin computing [42] and Pin & play [43] are power-supply method by sticking an electrode into the communication medium like a parallel plate waveguide. These methods allow the top layer of the medium to be an insulator for protection. In Pin & play the devices communicate with each other via the identical medium.

CarpetLAN [44] is one of human body communication methods by put carpet-like unit with electrodes side by side on a floor. The unit and the device that a person holds are connected via a human as a communication medium and the midair and the signals that the unit detects are transmitted to an access point by hopping the units. Position detection is possible by identifying the carpet that connects the device the most strongly. The carpet size is about 1 m square.

IntelliMat [45] is the position-detect system. In this system, tile-like units that includes RFID tags are placed side by side. An antenna attached to the back of slippers receives information of the tags. Although the tile-like unit is the same as our approach, aerial radio signals are used.

Free access mat [46] is a communication system with a sheet-shaped waveguide and is aimed at a body-centric communication. It consists of a ground layer and two thin layers of patch array. Microwave energy whose frequency is matched to a resonant frequency of the patch is confined in the mat. An interface between a device and the mat is a dipole antenna. Although microwaves are emitted into the air, this system enables devices to transmit signals with lower power by heightening the transmittance between the devices via this system and interferences caused by devices are reduced.

1.4.3 Establishment of a reliable network

In order to improve the reliability of the wireless network, some researches are conducted. A wireless PROFIBUS [48], an extensive communication system of an existing field bus, is one of solutions. Moreover, the coexistence of multiple wireless networks is also desired in the use of unlicensed band [49][50] from the viewpoint of usability. The IEC standard for coexistence management of wireless industrial system has been developed [51]. In a railway industry, reliable communication is also required. In [52], the scheme to ensure reliability is standardized.

1.5 Organization of the thesis

The organization of the thesis is following. In Chapter II, the concept of the UWB 2DC tile and preliminary experiments are conducted to ensure the feasibility. Chapter III presents the signal propagation model in the 2DC tile is proposed and the communication characteristics of the sheet that is clarified with the model to design a physical layer protocol and also describes those of the entire system where the multiple tiles are connected. Then the suppression method of the radiation from the tile is presented in Chapter IV.

After position detect with the proposed system is described in Chapter V, we will finally conclude the thesis in Chapter VI.

Chapter 2

UWB 2DC tile system

In this chapter, a UWB 2DC tile system is presented as a method to establish a high-speed and reliable indoor communication system with 2DC. Preliminary experiments are conducted to ensure the feasibility of the system.

2.1 Concept of a 2DC tile

2.1.1 UWB 2DC tile

The UWB 2DC tile system adds a function of a communication infrastructure to a surface like a floor, a ceiling, a wall. The conceptual diagrams of the 2DC tile system in the case of a floor application are shown in Fig. 2.1. The tile system is established by placing tile-like communication units side by side. This unit is called a 2DC tile. The network are is freely extended and a whole floor can be covered with this system. A specialized coupler embedded in devices is put on the tile system and devices are connected via the system. Although the size of the 2DC tile is not restricted, a standard carpet tile size like 50 cm in Japan is useful.

The appearance of the tile is similar to an ordinal raised-floor system unit and the tile consists of three layers: a surface layer, the 2DC sheet, and a base layer with mechanical and electrical connectors. The surface layer is a dielectric material, for example, a carpet tile. The second layer is the 2DC sheet mentioned in 1.2.2. The sheet-edge design is important because it affects the radiation from the sheet. In the system where multiple tiles are installed, the radiation from the tile should be suppressed. In Chapter 4, suppression method is described in detail. Typically the sheet edges are shorted between the inductive layer and the ground layer like Fig. 2.2 to avoid connection to the neighboring tiles by the radiation from the sheet gap. The open boundary like Fig. 2.2 is useful because of easier fabrication than the shorted one if the isolation performance is acceptable. The base layer includes some electric devices and relays signals between the neighboring tiles. The body of the base layer is a plastic hollow block commercially available as a component of an ordinary indoor raised floor system.

The signal path between the devices are in the following. One device, device A transmits a signal to the tile via the coupler, then a part of the signal propagate to the neighboring tile via the base layer. The other device receives the signal from the tile by using the coupler.

The expected characteristics of the tile system are following.

- Low power-consumption communication
  The shorted edge causes the standing waves and strengthens the signal intensity in the tile. This property enables the low power-consumption communication and stable connection even under the transmission-power restriction like UWB.

- Small delay property compared to the aerial communication
  The reflective boundary-condition of the 2DC sheet causes many multipath signals and since signals propagate in a two-dimensional plane, path loss in the tile is smaller than that in the air. The longer delay, thus, is expected to single 2DC-sheet propagation than to free-space propagation with the same dimension. In the tile system, however, the smaller delay property is expected than the aerial communication because the whole communication area is divided to tile-size and the actual propagation area becomes smaller. In addition, the delay property is independent of the entire network area. These characteristics enable higher communication speed by optimizing a symbol rate.
- Easy installation and maintenance
  In practice, easy installation and maintenance of the system is important. Special skills and tools are not necessary when the tiles are connected with non-contact manner, and installation and replacement cost is the same as the ordinal raised-floor system that is inevitable in the modern office when the tile function is embedded to raised-floor system in advance.
- Increase of radiation into the air
  Although no radiation theoretically occurs with an infinite-length 2DC sheet, some energy are emitted into space from the tile because of its finite length. Since the tile system includes multiple 2DC sheets, the radiation increases along with the expansion of the system area.

Except the increase of the radiation, these characteristics are favorable for the high-speed and reliable communication. Therefore, our goal will be achieved by developing the

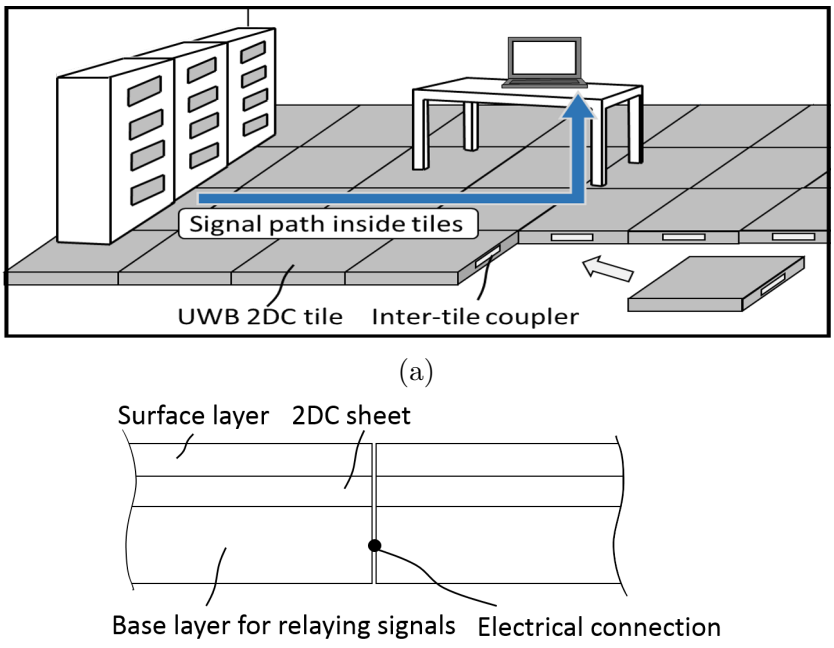

Fig. 2.1. Concept diagram of the 2DC tile system. (a). Perspective view. (b). Cross-sectional view.

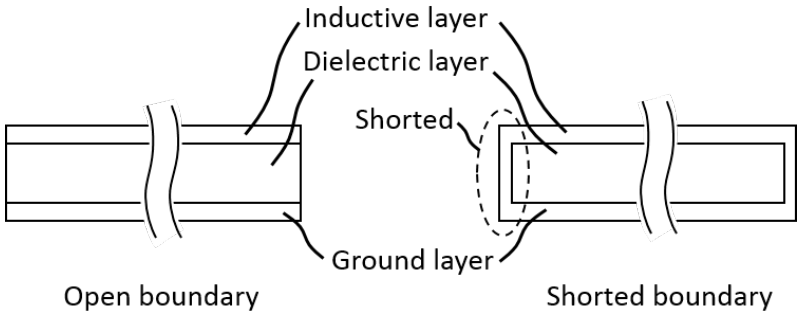

Fig. 2.2. Boundary condition of the UWB 2DC tile. The difference is whether the inductive layer and the ground layer of the 2DC sheet is shorted at the boundary or not.

2DC tile system. The following three materials are necessary to be developed. One is the base layer. Since the base layer relays the signals in the sheet, it is the significant device in the system. Other is the evaluation of communication characteristics. A physical layer protocol that determine the maximum data rate is strongly involved in the delay property and transmittance, which are dependent on the communication medium[53]-[55], thus these properties is necessary to be clarified. The other is the suppression method of the radiation from the sheet. As mentioned above, the radiation from the sheet will increase in the tile system, the suppression method, therefore, is needed to strengthen immunity against aerial radio signals.

2.1.2 Base layer design

As mentioned in 2.1.1, the tiles are connected at the base layer level and signals from a device are relayed via the base layers. The base layer design, therefore, is one of the most important factors to achieve the tile system. The base layer need to satisfy the following requirements.

- Connection to the peripheral components
  Since the base layer relays the signal to neighboring components, the 2DC sheet or the neighboring base layer, the connector for them are necessary. The proximity coupler enables the easy connection.
- Uniform signal-intensity
  Signal intensity decreases due to a tile-tile and tile-sheet transmission. A repeater circuit is necessary to maintain the signal intensity uniform across the tiles.
- Prevention of oscillation
  A single tile has at most four connection ports with the neighboring tiles. Multiple connection topology makes redundant signal paths. On the other hand, these paths can form undesirable loop path while the communication reliability is improved. The protocol to avoid such an oscillation is necessary.

Fig. 2.3 is one of the base layer designs that includes a repeater circuit and two specialized proximity couplers. Fig. 2.4 shows a design of the prototyped repeater circuit [56].

The repeater circuit compensates for the attenuation of tile-tile and sheet-tile transmission and maintains the uniform signal intensity across all the tiles.

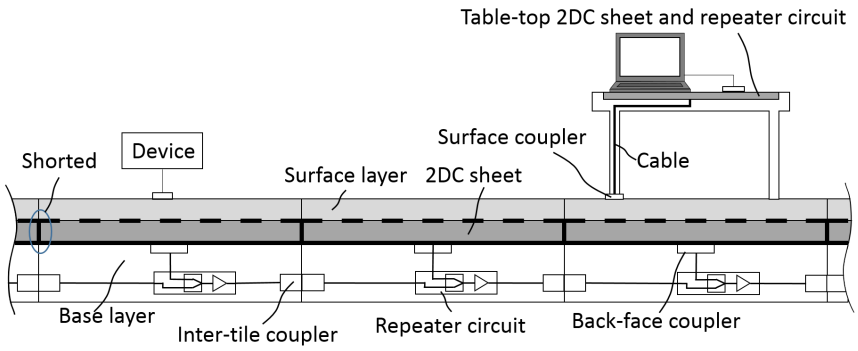

Fig. 2.3. Cross-section diagram of the tiles. Signals are transmitted through inter-tile couplers.

The two specialized proximity couplers in the base layer are named as a back-face coupler and an inter-tile coupler. The back-face coupler connects the 2DC sheet and the repeater circuit. It is fixed at the center on the top of the base layer and contacts to the back-side of the sheet, where a circular aperture is formed on the ground plane (a circular aperture is removed from the ground). The inter-tile coupler is implemented at side faces of the base layer and connects the neighboring base layer as shown in Fig. 2.3. Fig. 2.5 shows a prototyped inter-tile coupler with the insertion loss of 10 dB [57].

In the 2DC system, another type of non-contact coupler is used to allow a transceiver device to be connected with the tile system. We call it as a surface coupler. This coupler is embedded in a transceiver device, and is put on the tile thus enables the connection between the device and the 2DC sheet. It is designed to enable the wideband connection anywhere on the tile through the mesh surface of the sheet. These coupler designs depend on the frequency range of the application.

The signal can reach a device on a table as well as on the floor. Such a signal path is shown in Fig. 2.3 and is established as an expansion of the floor path with the same component used in the tile [56][58]. In this case, we assume that the repeater circuit and the 2DC sheet are embedded in the table. The repeater circuit on the table and the surface coupler attached to the bottom of one of table legs are connected with a cable. This configuration enables users to move the desk freely on the floor while keeping the connection between the tile and the table.

In [59], the loop-avoidance method is proposed. The concept is similar to frequency division multiplexing (FDM). The separate frequencies are allocated to an uplink signal and a downlink signal. Fig. 2.6 shows the design of a frequency conversion circuit.

Based on these base-layer components, the prototype tile system is developed in [58].

2.2 Electromagnetic simulation of signal propagation inside the 2DC sheet

The feature of the 2DC tile is that the 2DC sheet is shorted at the edge and the standing wave caused by the shorted edge is used to heighten the SNR and compensate for the transmission-power limitation of UWB radio. In this section, an electromagnetic (EM) is conducted to examine the signal propagation in the sheet.

2.2.1 Setting

Fig. 2.7 shows the overview of the simulation model. The dimensions of the 2DC sheet are 500 mm in side length and 1 mm in thickness. The mesh pitch of the inductive layer is 4 mm and the line width of the mesh is 1 mm. The thickness of the mesh is 0.01mm. The mesh material is assumed to be aluminum. The dielectric layer is 1-mm thick, and its relative permittivity is set at 2.1. These are the typical values in the previous 2DST (2DC) system [26]. We apply an electric boundary condition to all the boundaries except the mesh-layer side as the shorted edge or the ground layer. Input signals are excited at

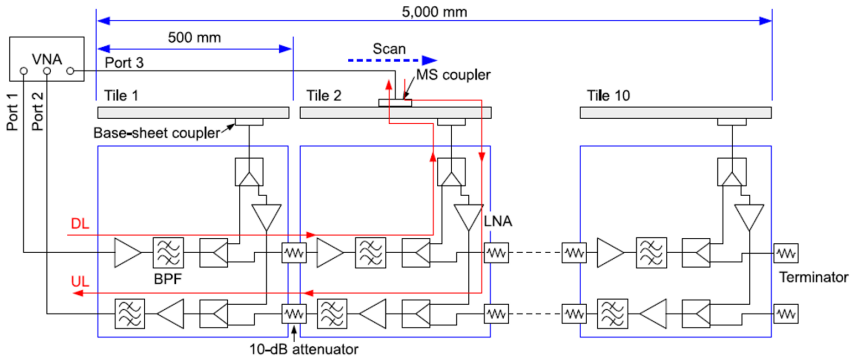

Fig. 2.4. Prototype base layer design [56] ©2015 IEEE.

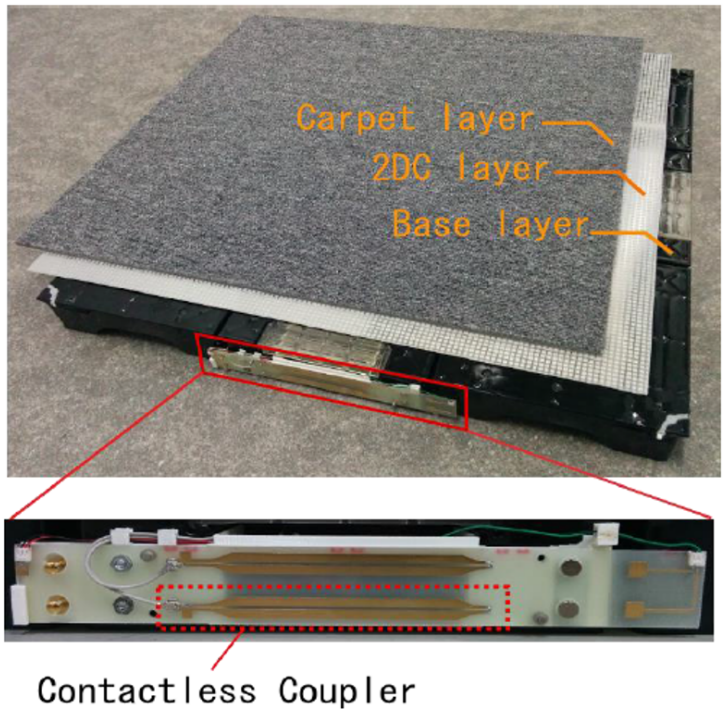

Fig. 2.5. Prototyped inter-tile coupler [57] ©2015 IEEE.

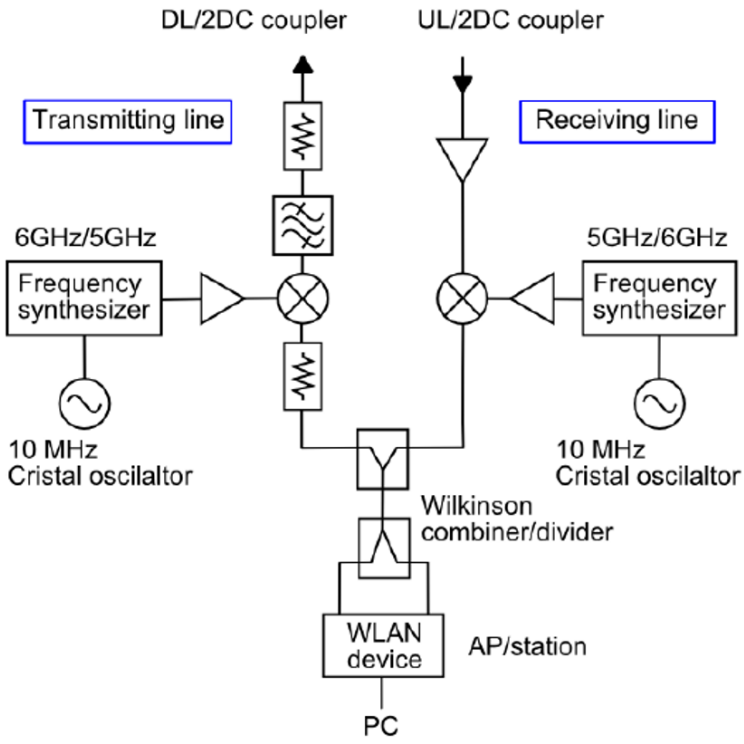

Fig. 2.6. Prototyped inter-tile coupler [59] ©2015 IEEE.

the waveguide port set at the boundary. The waveguide port size is 100 mm for the lower frequency bound of 3.1 GHz. Signals are observed at six points in consideration of the sheet symmetry. The simulation is conducted with CST Microwave Studio [60].

2.2.2 Result

Fig. 2.8 shows the amplitude distribution of the electric field at the center height of the dielectric layer, for frequencies f = 3 GHz, 6 GHz, 8 GHz and 10 GHz. The distribution at each frequency has the pattern. These results indicate that the standing waves are generated inside the sheet. Orthogonal frequency-division multiplexing (OFDM) is one of proper modulation methods to maintain the quality of communication under the rich multipath environment like the sheet.
Fig. 2.9 shows the intensity of the electric fields at the six points of 1–6 shown in Fig. 2.7. Position 5 is located at the origin of the xy coordinate. The vertical line of the figure shows the normalized values by the largest value in the 2DC sheet. The lowest value is about -35 dB at$(x, y) = (0, 0)$ and $f = 3.8$GHz. The lowest value among the high-band (from 7.25 GHz to 10.25 GHz in Japan) is about -32 dB at $(x, y) = (126, 126)$ mm and $f = 10.2$ GHz in our spatial resolution of simulation. These results show the frequency range of UWB is well covered.

2.3 Preliminary Experiment

In this section, the feasibility of the connection between the tile and the coupler is examined with two experiments. In a practical use, a dielectric material is put on the 2DC

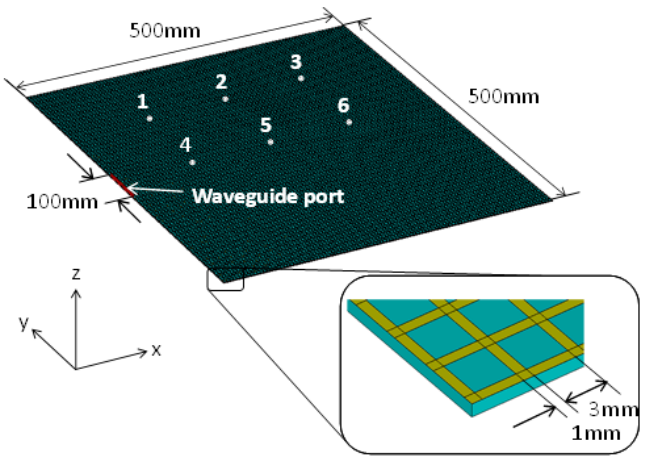

Fig. 2.7. The overall simulation model of 2DC sheet (upper) and the magnified figure of the mesh configuration (lower right). The 2DC sheet model consists of an inductive layer and dielectric layer. The back-side boundary condition of the dielectric layer is "electric" since a conductive layer, ground layer, exists on the back of the dielectric layer. The side boundary condition of the dielectric layer is also "electric" since the sheet edge is shorted as shown in Fig. 2.2(b). Signals are inputted from the 100mm-wide waveguide port.

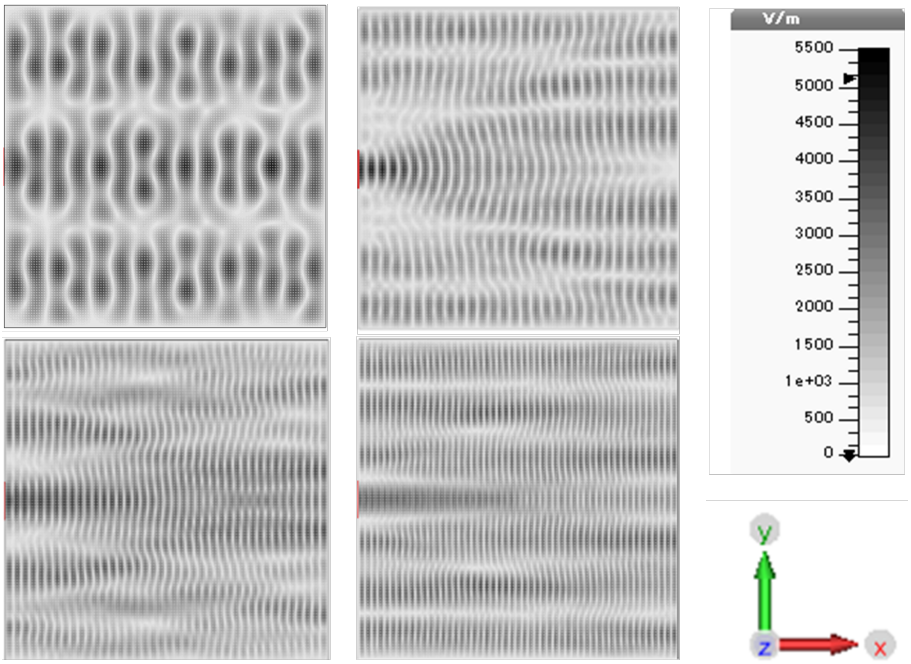

Fig. 2.8. The amplitude distribution of electric field at the center height of the dielectric layer for f = 3 GHz (upper left), 6 GHz (upper right), 8 GHz (lower left), and 10 GHz (lower right). Each figure shows that a standing wave is generated.

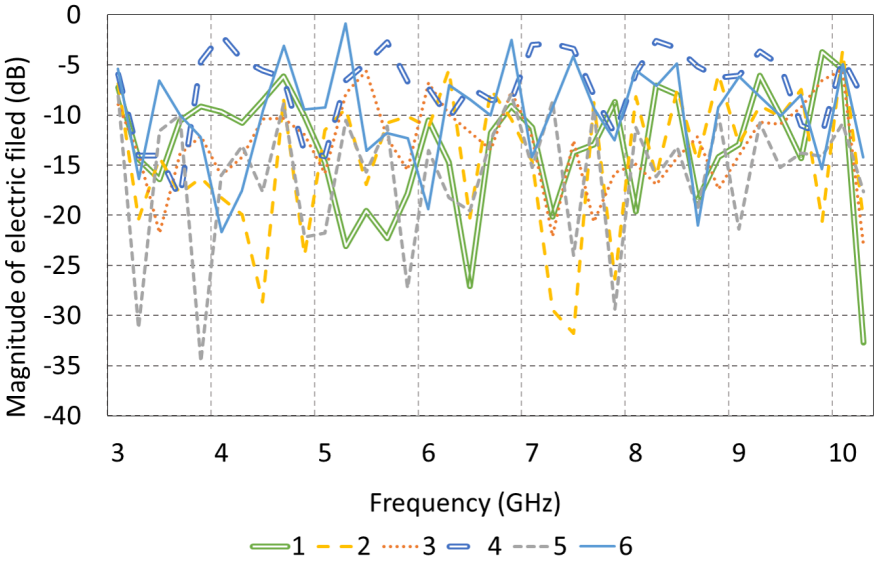

Fig. 2.9. The amplitude of electric field at the six sample points in a 2DC sheet. The amplitude is normalized by the maximal value in the 2DC sheet at each frequency.

tile as the surface layer. The thickness of the material has an effect to the connection because the coupler and the sheet are connected with proximity connection. The relation between the thickness of the surface layer and the connectivity is examined. In addition dependency on a coupler position to the connectivity is also examined because the communication property is different among the coupler position due to standing waves generated in the sheet.

2.3.1 Received power ratio

The bandwidth of UWB is so wide that the communication property is different among the frequencies. The statistical analysis, therefore, is effective to evaluate properties of the bandwidth. In order to express an average property across the UWB bandwidth and calculate the SNR, we define a ratio of a received power to a transmission power as the received power ratio P_R as follows.

$$P_R \equiv \frac{P_{Rx}}{P_{Tx}}, \tag{2.1}$$

where P_{Tx} and P_{Rx} denote the transmitted and received signal power, respectively. They are calculated by integrating the power spectral densities, p_{Tx} and p_{Rx} through the bandwidth of interest B.

$$P_{Tx} \equiv \int_B p_{Tx}(f)df. \tag{2.2}$$

$$P_{Rx} \equiv \int_B p_{Rx}(f)df. \tag{2.3}$$

By using the transfer function from the transmitter to the receiver, P_{Rx} is expressed as

$$P_{Rx} = \int_B |H(f)|^2 p_{Tx}(f)df. \tag{2.4}$$

Suppose that the transmitted power density is constant across the bandwidth because transmitted signal power in UWB technology is defined as −41.3 dBm/MHz.

$$p_{Tx}(f) = \bar{p}_{Tx}, \tag{2.5}$$

where $\bar{p}_{Tx}$ denotes the constant value. By substituting Eq. (2.4) and Eq. (2.5) to Eq. (2.2) and Eq. (2.3), we obtain

$$P_{Tx} = B\bar{p}_{Tx}. \tag{2.6}$$

$$P_{Rx} = \bar{p}_{Tx} \int_B |H(f)|^2 df. \tag{2.7}$$

Substituting Eq. (2.6) and Eq. (2.7) into Eq. (2.1), we finally obtain

$$P_R = \frac{1}{B} \int_B |H(f)|^2 df. \tag{2.8}$$

Therefore, the received power ratio P_R is calculated by averaging intensity of the transmittance between a transmitter and a receiver over the bandwidth of interest.

2.3.2 Effect of the surface layer

In the tile system, a surface layer is installed as a top layer of the tile. For example, carpet clothes in a floor application and a decorative laminate in a desk-top application. Since a 2DC sheet and a specialized coupler installed in a device are connected with proximity connection, a thickness of the surface layer weaken their connectivity. For evaluating the effect of the surface layer, the transmittance between the coupler and the sheet is measured under the following conditions.

Setting

An experimental setting is almost the same as the former experiment as shown in Fig. 2.10. The size of 2DC sheet is the same configuration as the simulation model in 2.2. The sheet length is 500 mm. The pitch of the mesh is 4 mm and the line width is 1mm. The thickness of the mesh is 10 μm. The material of the mesh is aluminum. The dielectric layer is made of a 1mm-thick polypropylene plate. In this experiments, the inductive layer and the ground layer are open not shorted since they are both reflective and the difference is not critical in this basic experiment. Input signals are excited in the sheet through the 0.1 mm-thick copper plates attached to the inductive layer and the ground layer as shown in Fig. 2.11. A horn-shaped pattern is used at the connection between the cable and the 2DC sheet for avoiding reflection. The widths of horn pattern are 80 mm in the sheet side and 12 mm in the cable side, and it forms an exponential horn. The UWB coupler proposed in [21] for covering the UWB high band is used to receive/send signals from/to the sheet. The coupler is a simple rectangular plate of 32 mm by 14 mm as shown in Fig. 2.11, with simple patterns of two copper layers.

In this experiment, the thickness and a material of the surface layer is changed. The two kinds of foaming insulators and two commercial carpet tiles are examined. Relative permittivity of the insulators, Insulator A and Insulator B is 1.5 and 2.1, respectively. Their thickness is changed from 0 mm to 12 mm by 1 mm. In the case of the distance 0 mm, there is only the protection film between the sheet and the coupler. The carpet tiles, the model number YS1004 and CT1420 manufactured by Teijin Limited are used as Carpet A and Carpet B. Size of both carpets are 500 mm × 500 mm × 6 mm.

The transmittances for the UWB high-band are measured at the center of the sheet with a vector network analyzer (VNA), Rohde & Schwarz ZNB-20. The VNA is calibrated with

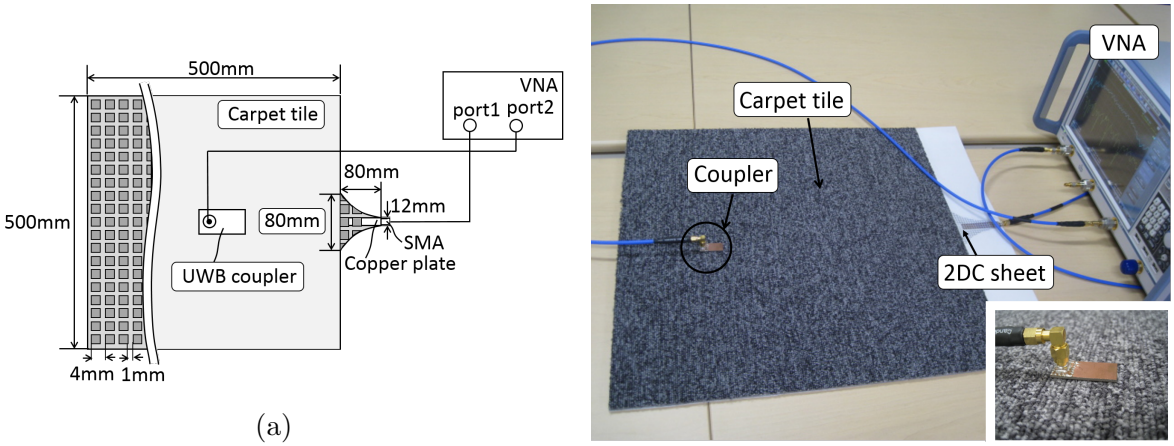

Fig. 2.10. Experimental setting. (a) The schematic diagram of the setting. Two commercial carpet tiles whose size is the same as the 2DC tile are examined in addition to two foaming insulators. (b) The photo of the experiment.

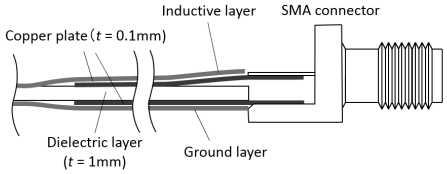

Fig. 2.11. Cross-section diagram of the feeding point at the sheet edge. Two 0.1 mm-thick copper plates connected to a SMA connector are attached to the inductive layer and the ground layer.

unknown-open-short-match (UOSM) mode. This mode is also used in all the following experiments.

Result

Fig. 2.12 shows the received power ratio calculated with Eq. (2.8). The received power must be higher than power of noise signals to communication with each other. Given that a noise source is only thermal noise, the signal-to-noise ratio (SNR) is expressed below.

$$SNR = \frac{P_{Rx}}{kBT} \tag{2.9}$$

$$= \frac{P_R \bar{p}_{Tx}}{kT} \tag{2.10}$$

where k and T denote Boltzmann constant, $1.386 \times 10^{-23}\mathrm{JK}^{-1}$ and a temperature in kelvin respectively, and kT is -114 dBm/MHz at a room temperature, $T = 300$ K.

If SNR of more than 20 dB is required, P_R must be -52.7 dB or more under the condition that p_{Tx} is -41.3 dBm/MHz. The result shows that such a SNR is achievable when an insulator thickness is under 10 mm and the examined commercial carpets also satisfy this requirement.

Fig. 2.13 shows that a stacked bar graph concerning the transmittance at 6-mm gap. The ratios of the S21 data number of $-n$ dB - $-(n + 10)$ dB to the total number of

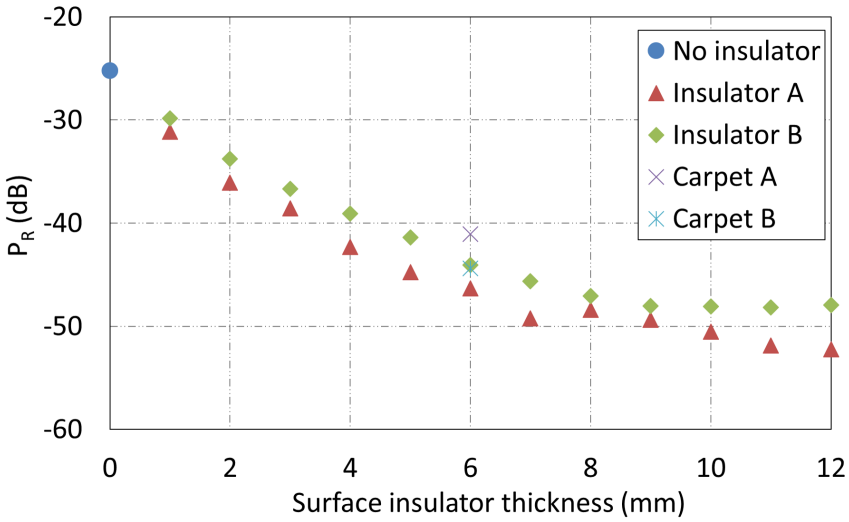

Fig. 2.12. Received power ratio. SNR is kept more than 20 dB up to10-mm thickness. SNR is corresponding to 20 dB when P_R is −52.7 dB.

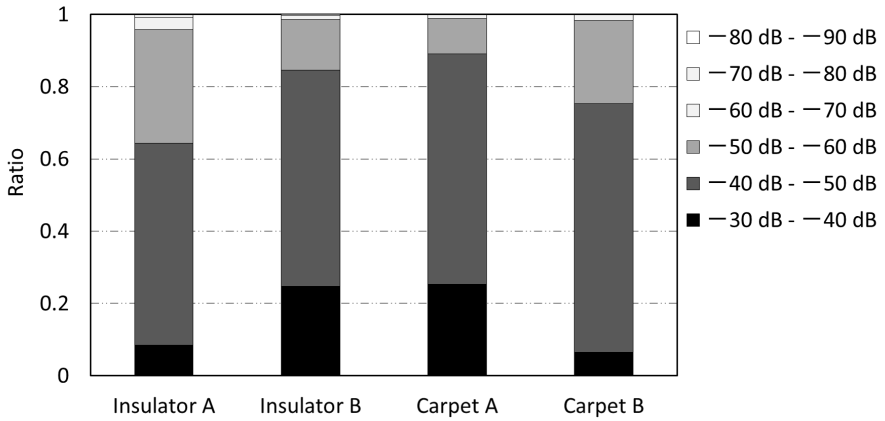

Fig. 2.13. The stacked bar graph about S21 at 6 mm. This figure shows that S21 is larger than −50 dB in more than 60% of the high-band. In the case of Insulator B and Carpet A, S21 is larger than −50 dB in 80% bandwidth.

the data are shown when n is from 30 to 80. All the data are sampled at every 1 MHz. The result shows that S21 is larger than −50 dB in more than 60% bandwidth of the high-band. In the case of Insulator B and Carpet A, S21 is larger than −50 dB in 80% bandwidth. Therefore, Carpet A is more suitable as a surface layer than Carpet B. In the following experiments, Carpet A is used as a surface layer.

2.3.3 Dependency of coupler position

Setting

Fig. 2.14 shows a schematic diagram of the experimental system and an overview photo. The constitution of the 2DC sheet is the same as that of the former section and Carpet A is used as a surface layer. In this experiment, the coupler proposed in [61] is used. This coupler has a circular shape and its diameter is 80 mm. The extraction efficiency

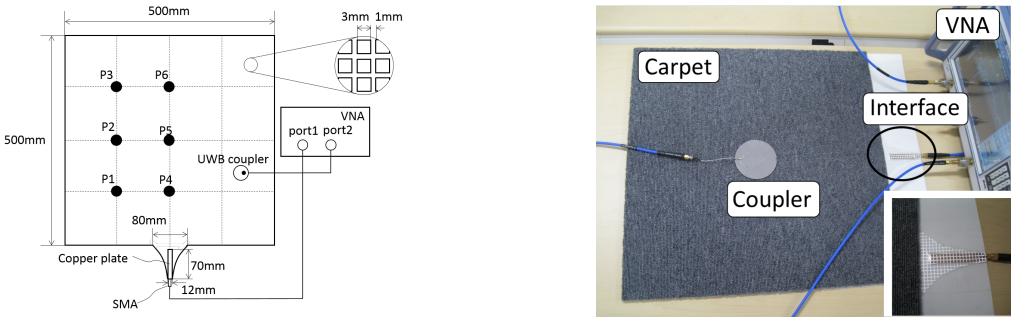

(a) (b)

Fig. 2.14. Experimental settings. (a). Schematic diagram. The transmittances between the UWB coupler and the feed point of the 2DC sheet at the six sample points of 1–6 are measured with a VNA. (b). Photo of the experimental settings. The coupler proposed in [61] was used as the UWB coupler. Carpet A used in the former experiment is put on the 2DC sheet as a surface layer.

is improved compared to the coupler used in the former experiment. In this experiment, the transmittances at the six sample points of 1–6 that are the same as those of the simulation are measured by using the VNA to clarify the dependency of coupler positions. The feeding point to the sheet and the coupler are connected to port 1 and port 2 of the VNA, respectively.

Result

Fig. 2.15 shows S11 (reflection) at the feed point of the 2DC sheet and S21 (transmittance) for each coupler position. Since S11 is less than −5dB, the major signal power is successively inputted to the 2DC sheet in the high-band. The value of S21 is fluctuating

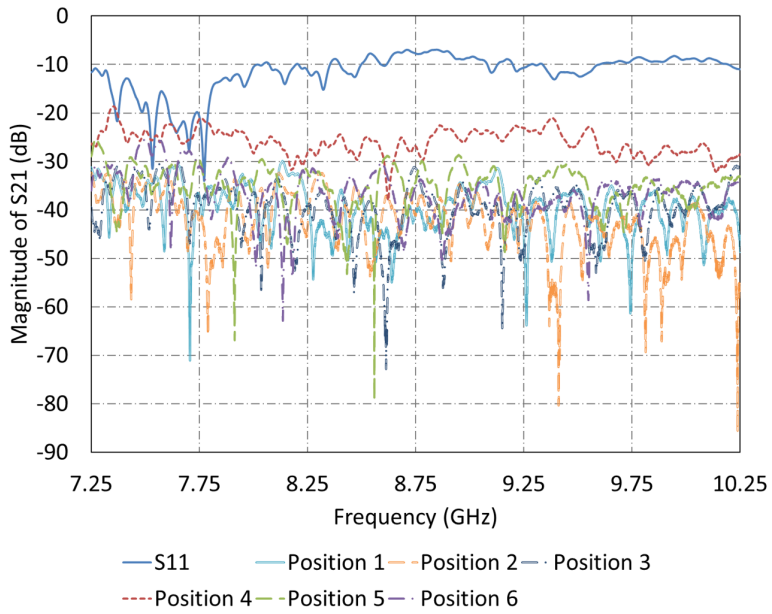

Fig. 2.15. S-parameter S21 (transmittance) and S11 (reflection) through the high-band. S21 is fluctuating mainly between −20 dB and −40 dB. S11 of port1 (the feed point) is smaller than 5 dB through the band.

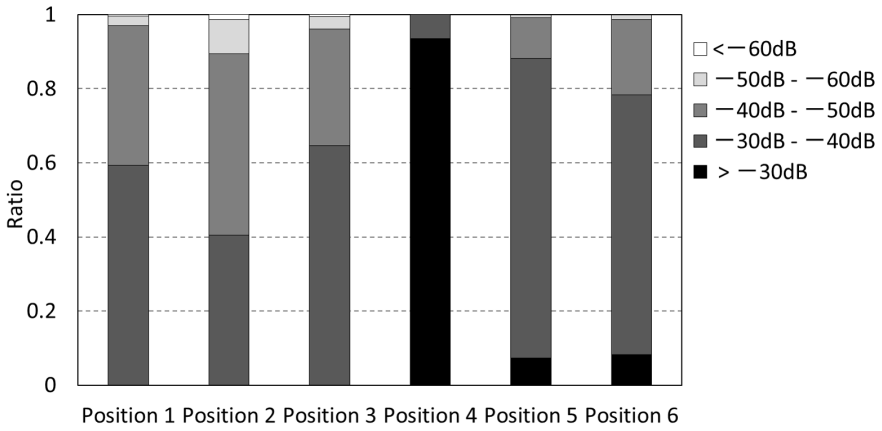

Fig. 2.16. Stacked bar graph on the experimental data of S21 at each position. This figure shows S21 is larger than −40 dB in more than 90% bandwidth of UWB high-band.

due to standing waves mainly between −20 dB to −40 dB in the band.

Fig. 2.16 shows the stacked bar graph for S21 at each sample point to present the total bandwidths for well-conditioned communication. All the S21 data are sampled with 1 MHz interval for each point. The ratios of the S21 data number of n dB – −(n+10) dB to the total data number are shown for n = 30, 40, 50, and 60. The result shows that S21 is larger than −50 dB in more than 80% bandwidth of the UWB high-band. The transmission coefficient of −50 dB can be considered to enable stable UWB communication under the signal-amplitude restriction of −41.3 dBm/MHz in OFDM-based UWB communication because SNR is equivalent to more than 20 dB. Therefore, SNR necessary for stable communication can be ensured with the tile system although null points are generated due to standing waves. Since the measurement points are limited because of a preliminary experiment, detail measurements for communication properties of the tile system is conducted in Chapter 3

2.4 Signal transmission experiment

The results in the former section shows UWB communication with the UWB 2DC tile is physically feasible. In this section, signal transmission using a pair of UWB communication devices is examined. The devices were developed by Apollo Giken Co.,Ltd.

2.4.1 Principle of OFDM

OFDM is one of the most widespread communication schemes and employed in Wi-Fi (IEEE802.11a/g/n), a digital television, a cellular networks like 4G, WiMAX and so on. Its characteristics are high-tolerance to the delay and the high-efficiency of spectrum. The delay-tolerance property is also suitable for the 2DC tile system due to its rich multipath environment.

The principle of OFDM is briefly described as below. An OFDM signal in frequency domain consists of multiple orthogonal frequencies as shown in Fig. 2.17. A frequency gap of neighboring subcarriers is equal to the basic frequency in base band. Although many carriers are modulated, they do not interfere with each other because of orthogonality. In addition, since the bandwidth of the single subcarrier is narrower than the total

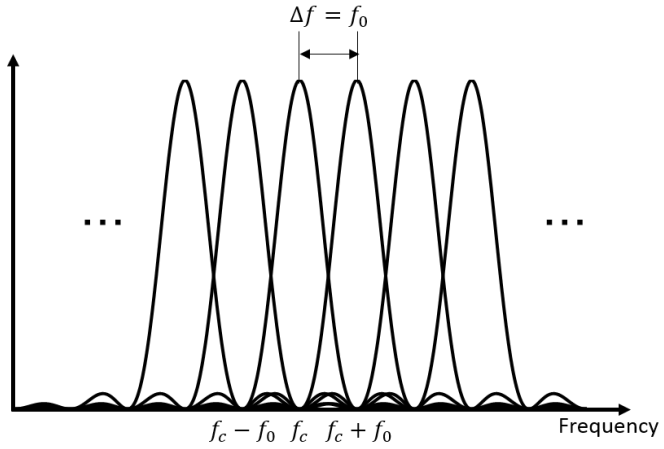

Fig. 2.17. Spectrum of OFDM. An OFDM signal consists of multiple subcarriers. The subcarriers are allocated by the bandwidth of a single subcarrier. The orthogonality of the subcarriers generate no interference between the subcarriers.

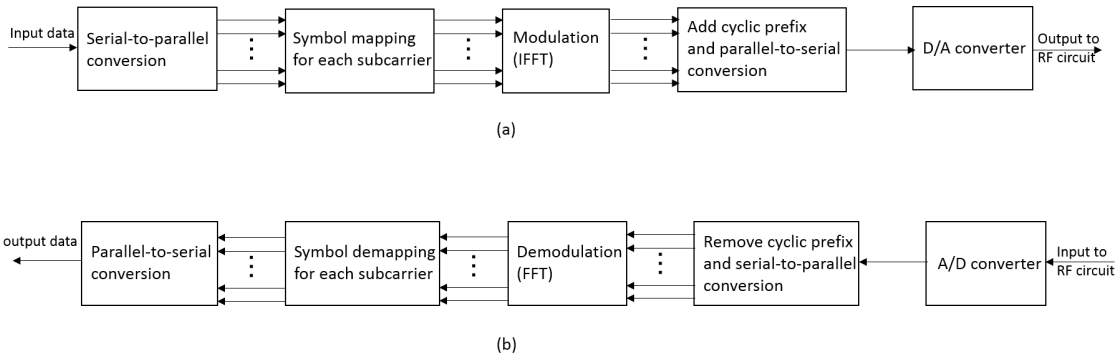

Fig. 2.18. Block diagram of modulation and demodulation process. (a). Modulation process. (b) Demodulation process.

bandwidth, the OFDM signal has the immunity to delay signals.

The baseband OFDM signal $s_B(t)$ is described as follows

$$s_B(t) = \sum_{k=1}^{N} \{a_k \cos(2\pi f_0 t) + b_k \sin(2\pi k f_0 t)\} \tag{2.11}$$

where a_k and b_k denote an I-axis component and a Q-axis component. f_0 is the basic frequency and N is the number of carriers. Suppose that $c_k = a_k - jb_k$, Eq. (2.11) becomes

$$s_B(t) = \mathrm{Re} \sum_{\mathrm{k=1}}^{\mathrm{N}} \mathrm{c_k e^{j2\pi k f_0 t}} \tag{2.12}$$

This expression is interpreted as the inverse Fourier transform of c_k. An OFDM signal, therefore, is obtained by applying an inverse Fourier transform to spectrum constituting by transmission data. A Fourier transform is used in the case of demodulation. The flows of the modulation and demodulation process are described shown in Fig. 2.18.

Although the OFDM signals have immunity to multipath signals of the same symbol, the interference can occur with different symbols. Guard interval (GI) is added to avoid

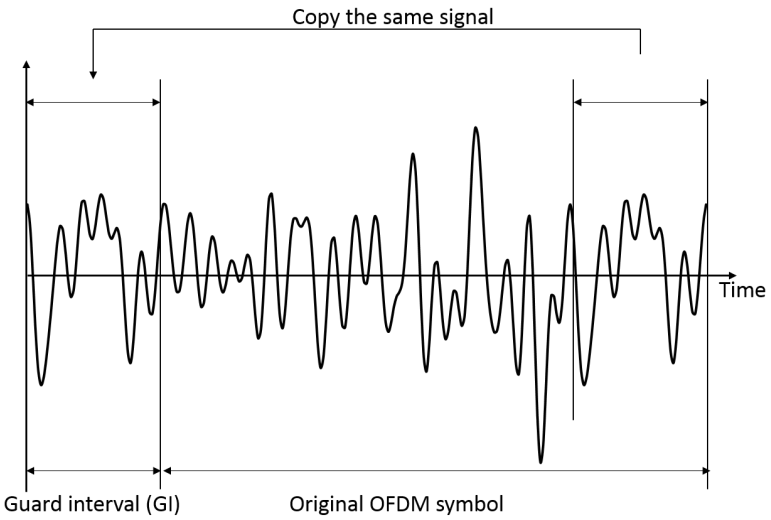

Fig. 2.19. Concept of guard interval (GI). The guard interval is the copy of the part of the last OFDM symbol. The sufficient length of GI, which is longer than the longest delay time avoid the interference between the symbols.

the interference. GI is a part of the last symbol and is added at the beginning of the symbol as shown in Fig. 2.19. The length of GI is necessary to be longer than the expected delay time.

2.4.2 Setting

Fig. 2.20 shows the experimental diagram and the overall picture. Signals are inputted to the 2DC sheet and received via the coupler put on a carpet tile. The carpet is Carpet A used in 2.3.2. The coupler is the one proposed in [61]. This coupler can extract more power from the 2DC sheet for the high-band than the coupler used in the former section. The transmitter outputs OFDM signals whose carrier frequency is 8 GHz and bandwidth is

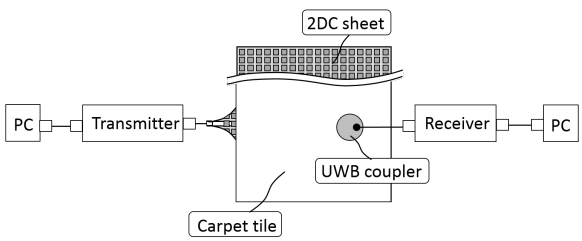

(a)

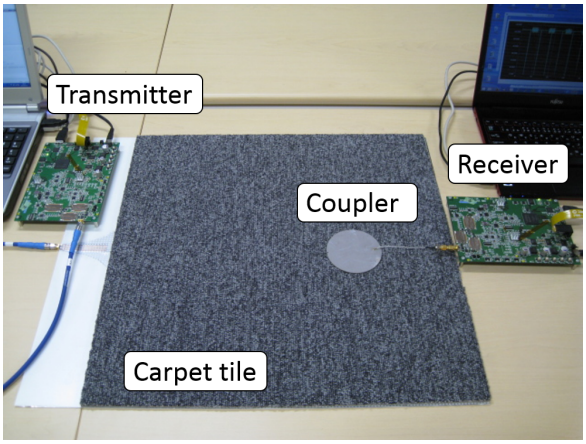

(b)

Fig. 2.20. Setting of OFDM signal transmission experiment (a) The schematic diagram. (b) Photo.

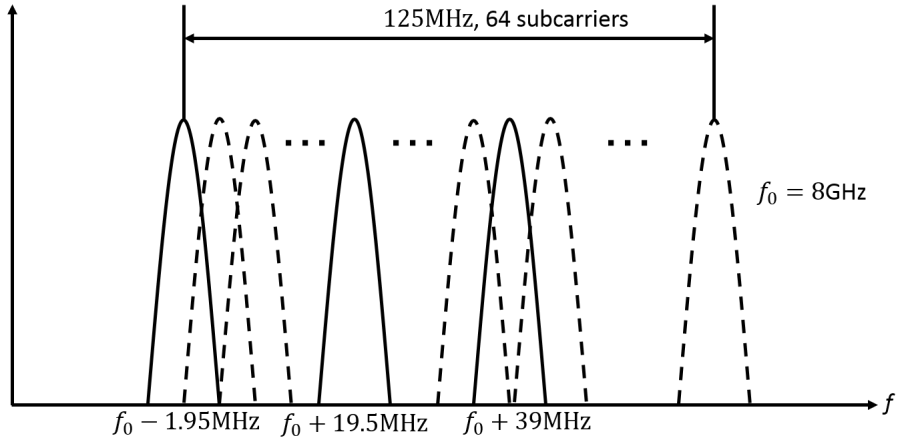

Fig. 2.21. Spectrum of transmitted OFDM signal. The bandwidth is 125 MHz and the number of the subcarriers is 64. Three subcarrier frequencies: 8.00195 MHz, 8.0195 MHz, and 8.039 MHz are examined.

125 MHz and the number of the subcarriers is 64 as shown in Fig. 2.21. The specifications of OFDM signals are as follows. The number of FFT point is set as 64. Therefore the bandwidth of a subcarrier is about 1.95 MHz. The length of a guard interval (GI) is 64 ns. No signals are transmitted for 1,024 ns after one symbol whose length is 576 ns is transmitted to distinguish signals clearly. In this experiment, only one of the subcarriers is used so that it can be easy to understand a waveform of signals. Three subcarrier frequencies, 1.95 MHz, 19.5 MHz, and 39 MHz in the 125 MHz bandwidth are examined.

2.4.3 Result

Fig. 2.22 shows one symbol of the transmitted waveform and the received one whose frequencies of the subcarrier are 1.95 MHz, 19.5 MHz, and 39 MHz, respectively. The amplitudes of both waveforms are normalized by the maximum one. Some noises are added to signals, but almost all the signals are received correctly.

In the UWB 2DC tile, multipath signals are generated. However, that influence is negligible since the signal duration time in a tile is just several nanoseconds which is corresponding to a few times reflections in a tile. The length of the guard interval is much longer than the storage duration.

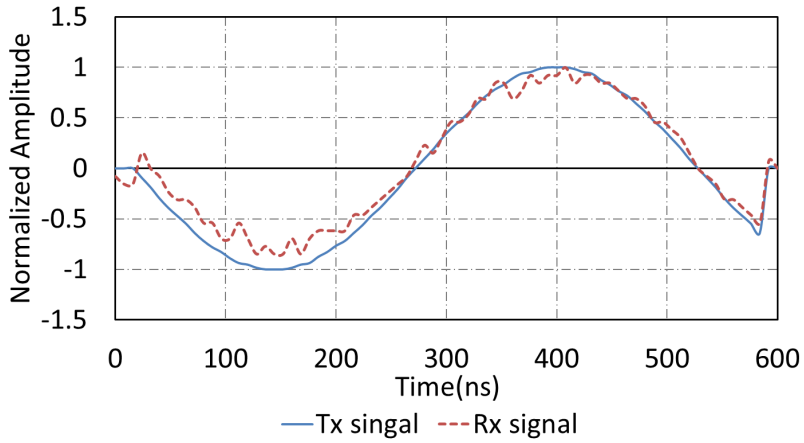

(a)

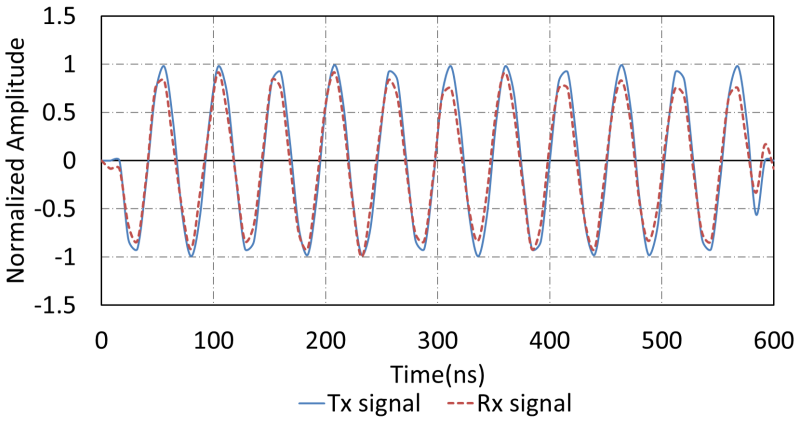

(b)

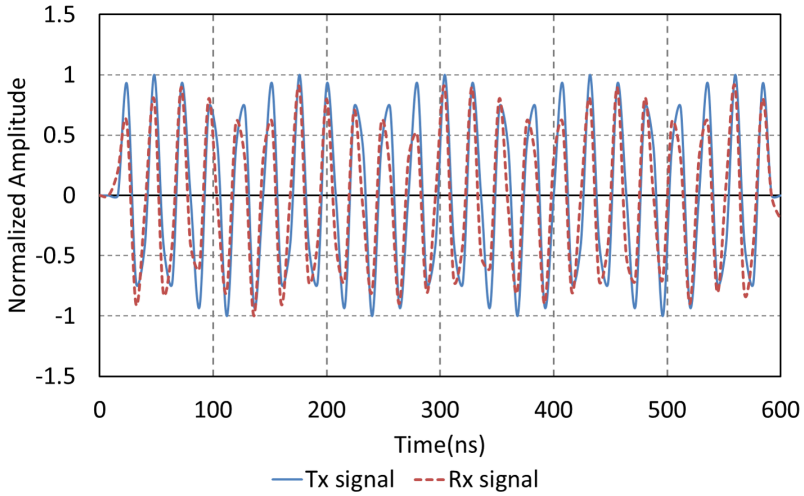

(c)

Fig. 2.22. Waveform of Tx and Rx signals. (a) 1.95 MHz. (b) 19.5 MHz. (c) 39MHz.

2.5 Conclusion

In this section, the 2DC tile system was proposed to establish the room-size 2DC network. This tile is a kind of the raised floor system and includes the 2DC sheet as the waveguide and the base layer for the signal relay. The tile network is easily extended by connecting the tiles with non-contact manner. The expected characteristics were described and are favorable to the high-speed and reliable communication system.

The three materials to achieve the tile were described. The base layer is one of them and the prototype design is described. The others are presented in the following chapters.

The EM simulation were conducted to examine the signal propagation property in the sheet and the preliminary experiments are also conducted to ensure the feasibility of the tile communication in the UWB high-band. The simulation results showed that standing waves are generated in the sheet: This property indicates that signal intensity in the sheet is strengthened while long delay and null points in frequencies are generated. The results of the preliminary experiments suggested that a received power ratio between the coupler and the tile rapidly decreases as the gap distance of them becomes larger, but SNR of 20 dB or more is achieved when the thickness of the gap is smaller than 10 mm. In addition, SNR of 20 dB or more is ensured in more than 80% of the UWB bandwidth at all the measured six points.

The OFDM signal transmission was also examined. The results showed that the signals are transmitted to a receiver via the 2DC tile successfully. Added noise was small enough to be negligible.

From these experimental results, the feasibility of stable communication via the tile system is ensured.

Chapter 3

Signal transmission properties of the 2DC tile

In the former chapter, the measured SNRs at the six points on the tile show that the UWB 2DC tile has the sufficient margin to the thermal noise and enables the stable communication with UWB radio. As the next step, communication characteristics of the entire tile is clarified to design a physical layer protocol in this chapter. Especially, a root-mean-square (RMS) delay spread and a SNR is focused on. These properties enables the physical layer protocol design, the configuration of a symbol rate that can avoid an inter-symbol interference and the selection of a modulation scheme. First, the signal propagation model in the signal tile is presented after the communication characteristics are briefly explained. Then it is verified with an electromagnetic (EM) simulation. An experiment is also conducted to obtain the two properties. In addition the RMS delay spread of the entire system where the multiple tiles are connected is presented with the model and the experiment.

3.1 Communication characteristics

- Power delay profile
  The power delay profile $P(\tau, m, n)$ reflects the transition of the received signal power. Parameter τ represents the excess delay time, and m and n identify a coupler position in a 2D orthogonal coordinate system fixed on the 2DC sheet. The power delay is defined as the square of the amplitude of the impulse response $h(\tau, m, n)$, as follows:
  $$P(\tau, m, n) \equiv |h(\tau, m, n)|^2. \tag{3.1}$$
  In the experiment, the transmittance-which is equivalent to a transfer function $H(f, m, n)$ between the couplers-is measured with a VNA. The impulse response $h(\tau, m, n)$ is calculated from the measured $H(f, m, n)$ by an inverse Fourier transform.
- RMS Delay Spread
  The RMS delay spread is calculated from the power delay profile and is a major factor to determine the coherence bandwidth and data rate. A physical layer protocol designed based on the RMS delay spread can avoid inter-symbol interferences. The RMS delay spread τ_{rms} is calculated as follows [62].
  $$\tau_{rms} = \sqrt{\overline{\tau_m}^2 - \overline{\tau_m}^2}. \tag{3.2}$$

where

$$\overline{\tau_m} = \frac{\sum_k P(\tau_k)\tau_k}{\sum_k P(\tau_k)} \tag{3.3}$$

and

$$\overline{\tau_m^2} = \frac{\sum_k P(\tau_k)\tau_k^2}{\sum_k P(\tau_k)}. \tag{3.4}$$

$\overline{\tau_m}$ and $\overline{\tau_m^2}$ denote the mean excess delay time and the second central moment of the power delay profile, respectively, whereas τ_k and k respectively represent the excess delay time and the number of multipath signals.

- Signal-to-noise ratio (SNR)
  The SNR is an essential factor to determine channel capacity. It can be calculated from the measured $H(f, m, n)$, as explained below. We define the received power ratio P_R as

$$P_R \equiv \frac{P_{RX}}{P_{TX}} \tag{3.5}$$

$$= \int_{F_{min}}^{F_{max}} |H(f, m, n)|^2 df. \tag{3.6}$$

  In these equations, P_{TX}, P_{RX} and B are the transmitted and received powers and the bandwidth of interest, which is defined as $F_{max} - F_{min}$, respectively. On the condition that the signal attenuation between transmitter and receiver can be represented by the transmittance, the ratio of the signal to the thermal noise, SNR, at the receiver is calculated as follows.

$$SNR = \frac{P_R p_{TX}}{kT} \tag{3.7}$$

  where p_{Tx} is the received signal power density, k and T denote the Boltzmann constant ($1.386 \times 10^{-23}\mathrm{JK}^{-1}$) and the temperature in degrees kelvin, respectively; the value of kT is -114dBm/MHz at room temperature ($T = 300$K). The upper bound of the power density p_{Tx} is defined as -41.3dBm/MHz in UWB radio.

3.2 Signal propagation model

In this section, signal propagation is modeled and the communication properties of the tile are examined both with the theoretical model and via EM simulation.

3.2.1 Formulation of the 2DC sheet signal propagation model

Electromagnetic wave propagation in a 2DC sheet can be expressed as a superposition of multiple linear paths. The reflection model is simpler than in ordinary indoor aerial radio systems because the geometric form of the reflective boundary is the precise square form of the 2DC sheet. To calculate the superposed signal received by a coupler, we consider a square tiling of the sheets, as shown in Fig. 3.1 [63]. Each of the multi-reflected paths is expressed as a straight line between the source point and one of the couplers. We assume that the contribution of each path is individually calculated and independent from other paths. Some received signals consist of multiple reflected components that propagate the same distance along different paths. For example, a pair of reflective symmetric paths, from the source point to couplers at (x_0, y_1) and (x_1, y_0), are shown in Fig. 3.1. The

reflection number is the number of times the straight line connecting the source to the coupler crosses over the boundaries of the tiling shown in Fig. 3.1.

A signal received by the coupler, $y(t)$, can therefore be described as

$$y(t) = \sum_{i=0} a_i x(t - \tau_i) \tag{3.8}$$

where a_i and τ_i denote the amplitude and time delay of the ith reflected component and $x(t)$ is a source signal. The received amplitude a_i depends on many factors including path loss, dissipation by the dielectric and resistive losses in the sheet, reflections at the sheet edges, signal extraction by the coupler, and attenuation due to signal absorption by other couplers nearer from the source. The attenuation by couplers in the 2DC is illustrated in Fig. 3.2. The coupler extracts a portion of the microwave flowing beneath it, and reduces the microwave power available to couplers beyond it. We assume that signal absorption by the coupler at distance r_1 reduces the signal intensity received at distance $r_2 > r_1$ equally, regardless of the path direction, as shown in Fig. 3.3. This is different from the shadowing effect considered in [63], which assumes a direction-dependent signal attenuation, modeled with rectilinear, diffraction-free propagation paths. The assumption adopted here yields a simpler model, where the coupler size factor is eliminated.

From these considerations, a_i is described as

$$a_i = \mathrm{e}^{-\alpha\tau_i} \sum_j R^{p_{i,j}} \sqrt{\beta_i \prod_{l=0}^{i-1} (1 - \beta_l)} \tag{3.9}$$

The first factor ($e^{-\alpha\tau_i}$) represents the attenuation caused by the dielectric and the resistive

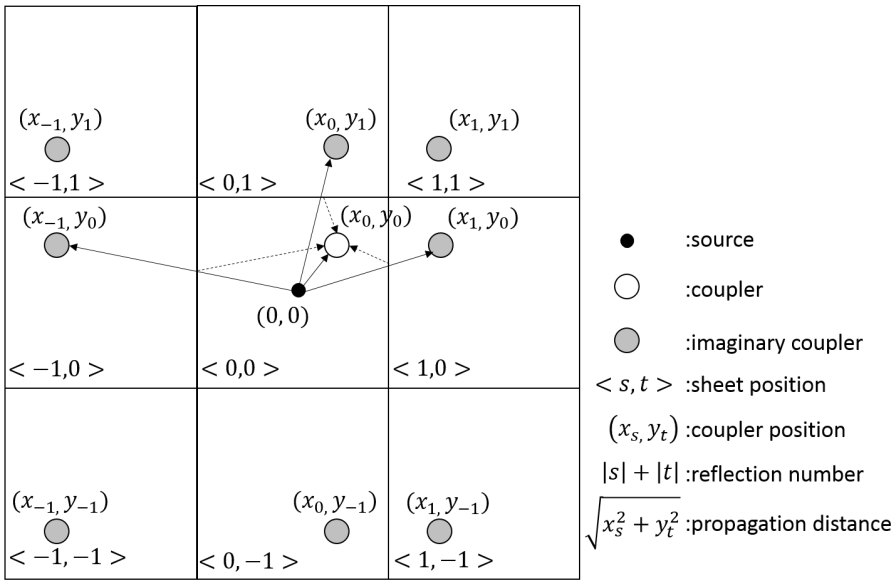

Fig. 3.1. Calculation method of the propagation distance and reflection number. The imaginary sheets are symmetrically put side by side and the signal is assumed to be propagate concentrically in the plane. The straight line between the source and one of the imaginary couplers corresponds to one of multi-reflected paths. Some received signals consist of multiple reflected components that propagated along the same distance along the different paths, such as like the paths from the source to (x_0, y_1) and (x_1, y_0).

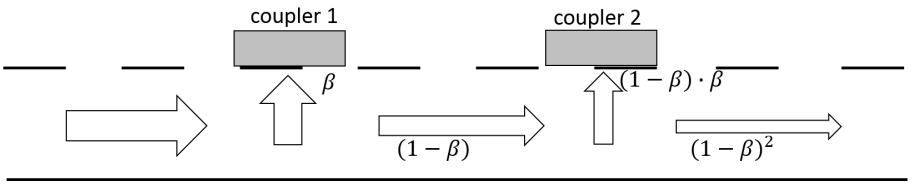

Fig. 3.2. Attenuation by the coupler. A part of microwave power is extracted by the extraction-power ratio β and the remaining part passes through the coupler.

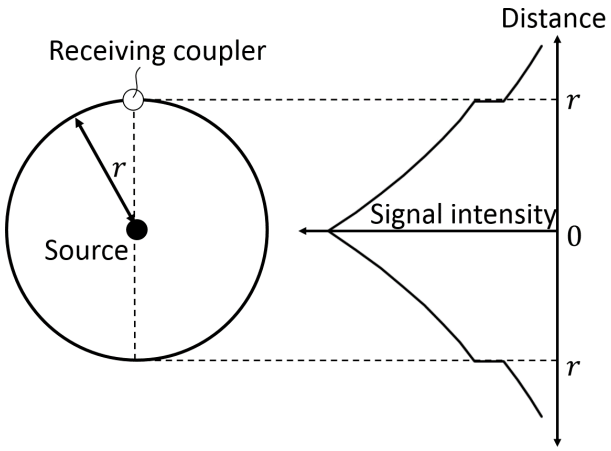

Fig. 3.3. Assumption of non-directional attenuation by the coupler extraction. The coupler reduces the signal intensity equally in all directions.

losses associated with the signal propagation in the sheet; α is an attenuation factor. The second factor ($\sum_i R^{p_{i,j}}$) represents the effect of reflection at edges, including attenuation and change in polarity. This factor is the total reflection coefficient of each signal in the ith multipath signal; R and $p_{i,j}$ represent the reflection coefficient, which is assumed to be independent of the reflection angle, and the number of the reflection, respectively; index j identifies the individual paths of the ith signal components. The third factor (β_i) is the ratio between the power extracted by the couplers in the ith path and the signal power integrated over a circle of radius d_i, d_i being the length of the ith path. This ratio depends on the frequency, and is described as follows.

$$\beta_i = c\frac{\lambda}{4\pi^2 d_i} \tag{3.10}$$

where c denotes the coupler efficiency (it is the ratio of the energy extracted by the single coupler from the sheet to the energy beneath the coupler), $\lambda/4\pi^2 d_i$ is the path loss of the two-dimensional signal transmission [25], and λ and d_i denote the signal wavelength and the distance between the source and receiving points. In the following section, β_i will be replaced with a constant value to simplify the model. This constant value is calculated as the average value over the bandwidth of interest; that is, the wavelength of the central frequency of the bandwidth is substituted into λ in Eq. (3.10). As mentioned in 3.4, radiation from the gap between the coupler and the sheet occurs in practice. The effect of the radiation can be included by replaceing c in Eq. (3.10) with $c+c_r$, where c_r represents the radiation efficiency. Eq. 3.10 is equvalent to the case of $c_r = 0$.

Given that the signal extraction by a coupler is assumed to decrease the power uniformly in all directions, as mentioned above, the total attenuation due to absorption by all the couplers within each path is the product of all the individual attenuations, as illustrated in Fig. 3.2. The attenuation caused by each coupler is the ratio of the power not extracted by the coupler at distance di from the source to the power arriving at the circle whose radius is di. Hence, the signal received at the receiving coupler is given by Eq. (3.8)-(3.10), and signal propagation is described by the electric parameters, α, R, and c, and geometrical parameters d_i and $p_{i,j}$.

3.2.2 Simulation setting

In this section, the dependence of the RMS delay spread and the SNR to the sheet length is analyzed with the numerical simulations.

To verify the above described propagation model, EM simulations are conducted with the following set of parameters: A single 2DC sheet is modeled, as shown in Fig. 3.4; the sheet length is changed from 200 mm to 800 mm. The line width and pitch of the inductive layer mesh are 1 mm and 4 mm, respectively. The material of the inductive layer and the ground layer is aluminum, whose conductivity is 3.56×10^7S/m. The dielectric layer is a 1-mm thick polypropylene layer, whose relative permittivity and loss tangent are 2.1 and 0.0005, respectively. The losses are assumed to be constant over frequency because the simulation is conducted to evaluate rough properties and they are experimentally examined. The materials described above are chosen from the viewpoints of performance and availability and are basically the ones used in our previous works. The sheet edges are shorted between the inductive layer and the ground layer. One discrete port is set at the center of the sheet and nine ports are set at regular intervals in one eighth of the area of the model, considering the sheet symmetric shape. Signals are transmitted from the center port and received at the other ports. The boundary conditions of the surrounding space are set as "open (add space)" at all of the boundaries, and the distances from the sheet to the top boundary and to the other boundaries are defined as 500 mm and 100 mm, respectively. The input signal is impulse shaped, with a bandwidth of 10.25 GHz. Nine

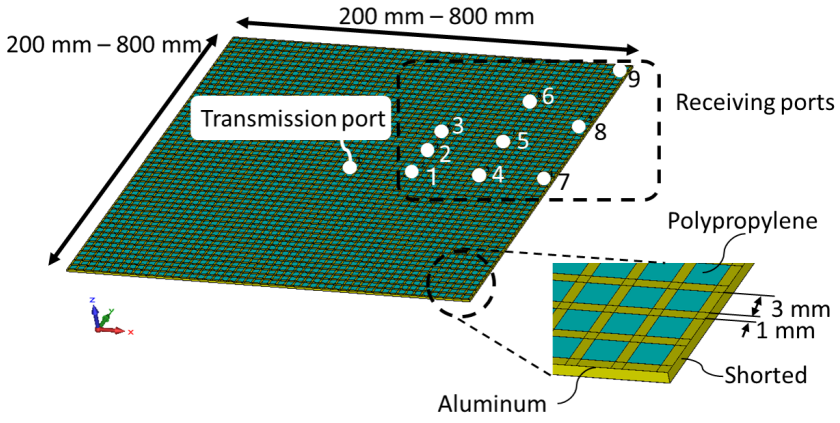

Fig. 3.4. Simulation model. The sheet length is changed from 200 mm to 800 mm. Input signals are excited at the discrete port of the sheet center. The nine discrete ports are monitored considering the symmetry of the sheet.

simulations are conducted for each sheet size, each one of them including the transmission port and one of the nine receiving ports. The simulations are conducted with the CST Microwave Studio EM simulation software.

3.2.3 Result

Fig. 3.5 shows the time-domain signals at position 5 of the 500 mm sheet. The input signal in the model is the same as the simulation. The model parameters shown in Table 3.1 are determined based on the simulation. The attenuation factor, 0.03ns^{-1}, corresponds to a loss of approximately 1 dB/m. The calculated average coupler efficiency is $c = 0.19$, and corresponds to a -19-dB transmittance of the direct signal at the receiving point 25 mm away from the source when the wavelength is 0.059 m (the wavelength of a 5.125 GHz signal). No radiation from the coupler is assumed, that is, $c_r = 0$. The timing of the signal

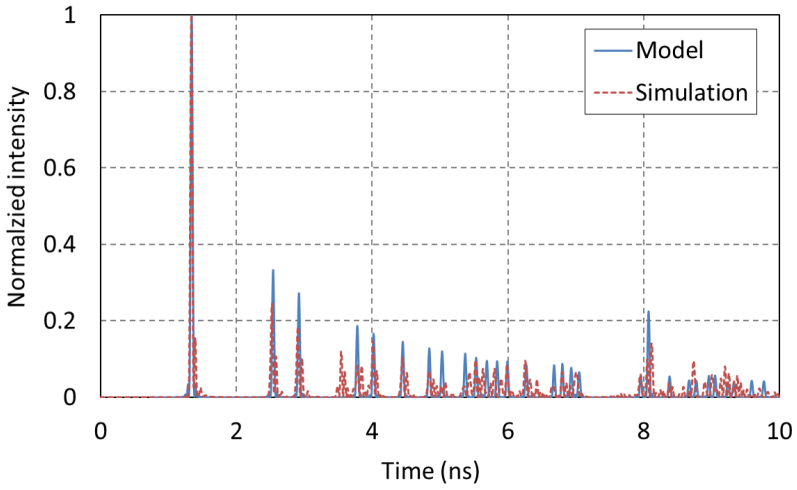

(a)

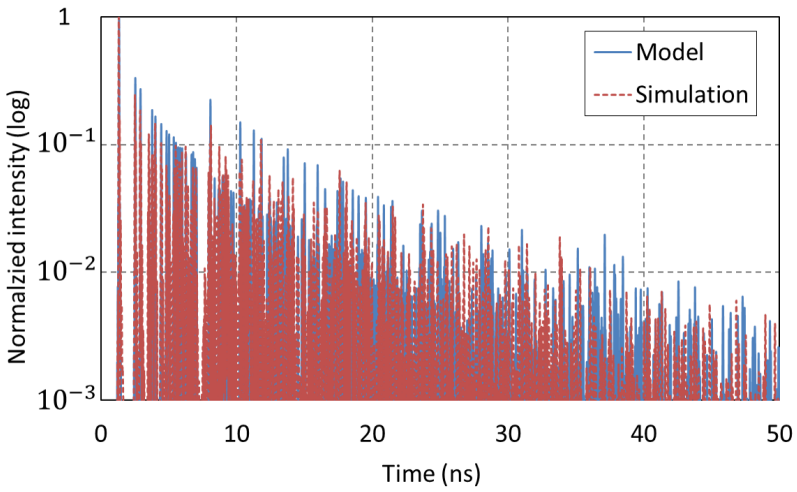

(b)

Fig. 3.5. Comparison of the time signals received at position 5 of the 500 mm sheet in the model and in the simulation. (a) Signals up to 10 ns. (b) Signals up to 50 ns. The timing and envelopes of the multipath signals are well matched.

Table 3.1. Parameter Settings of the Propagation Model in Fig. 3.5

Parameter	Value
Attenuation factor α (1/ns)	0.03
Reflection coefficient R	-0.99
Coupler efficiency c	0.19
Wavelength of the centroal frequency λ (m)	0.059

peaks and the intensity trends of the model are well matched to those of the simulation, as shown in Fig. 3.5(a). They are also compared in a longer time scale in Fig. 3.5(b) and again they show a good agreement. The results show that our model represented by Eq. (3.8)-(3.10) describes the signal propagation in the sheet with reasonable accuracy.

Fig. 3.6 compares the received signals generated by two different input signals: one is an impulse signal and the other is a band-limited Gaussian pulse, whose bandwidth is equal to the UWB high-band (from 7.25 GHz to 10.25 GHz). The results are obtained from the EM simulation. Although the latter result shows a bumpier envelope than the former, their macroscopic attenuation trends are in reasonable agreement. An impulse input was adopted in the following analyses because the difference was trivial.

The calculation results for the RMS delay spread are shown in Fig. 3.7. In addition to the parameters of Table 3.1, two coupler efficiencies, 1 and 0.019, are examined. Each plotted point represents the RMS delay spread value averaged over the nine receiving points. We set the dynamic range of the calculation to 20 dB; that is, the signal sequence after the last maximal intensity greater than −20 dB is discarded. The results show that the delay spread values are linearly related with the sheet size and variation regarding sheet size is from 4 ns to 8 ns within the settings.

The delay spread value of the smaller sheet is shorter than that of the larger sheet This is because the number of both couplers and reflections increases at the smaller sheet and the attenuations by coupler extraction and reflection shown in Eq. (3.9) therefore

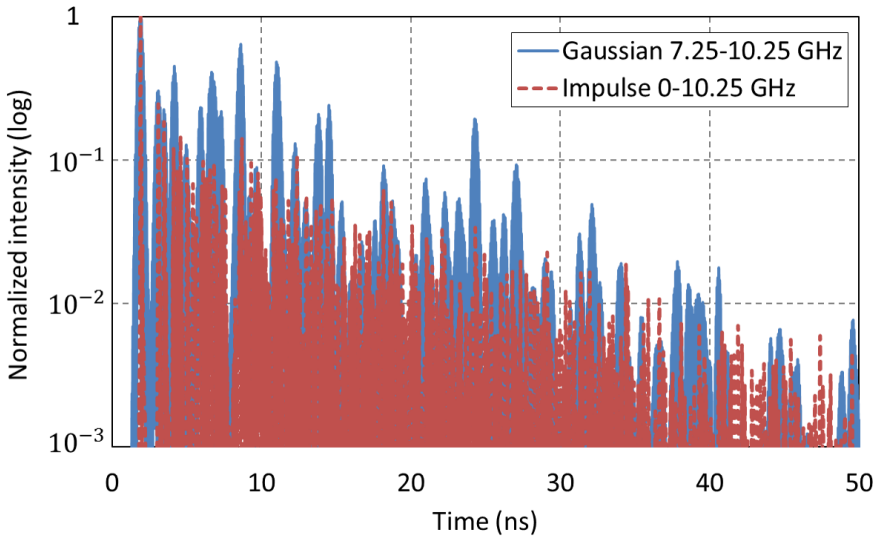

Fig. 3.6. Comparison of the received signals (impulse signal and band-limited Gaussian signal) at position 5 of the 500 mm sheet. The differences between them result from the bandwidth, but the attenuation trend is similar.

increase. The difference in delay spread value at each sheet length between the model (with the parameters shown in Table 3.1) and the simulation is at most 2 ns. The model achieves the estimation of the RMS delay spread value with reasonable accuracy.

Fig. 3.8 shows the average received power ratios, as defined as Eq. (3.6). Each plot is normalized by the value obtained for the 200 mm sheet. These values are calculated based on Parseval's theorem. The variation of the received power ratio for the 500 mm sheet is within ±7 dB. The received power ratio decreases as the sheet size increases and as the coupler efficiency decreases. This is because the dielectric and resistive losses are higher in relative terms for the larger sheet.

Fig. 3.9 shows a stacked bar graph of the obtained simulation results for the transmittance of the 500 mm sheet at each receiving port, from 7.25 GHz to 10.25 GHz. The number of frequency points in each range (as a fraction of the total number of points) is denoted by the color of the bar. The bar graph shows that the transmittance is −30 dB or more over 80% of the bandwidth at all receiving points and does not strongly depend

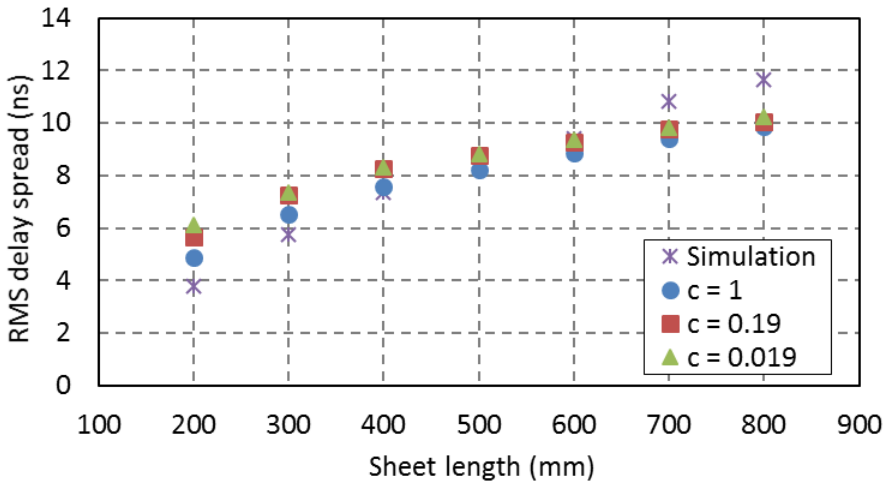

Fig. 3.7. Average RMS delay spread value at the nine points of each sheet length. The values are in a linear trend with the sheet size.

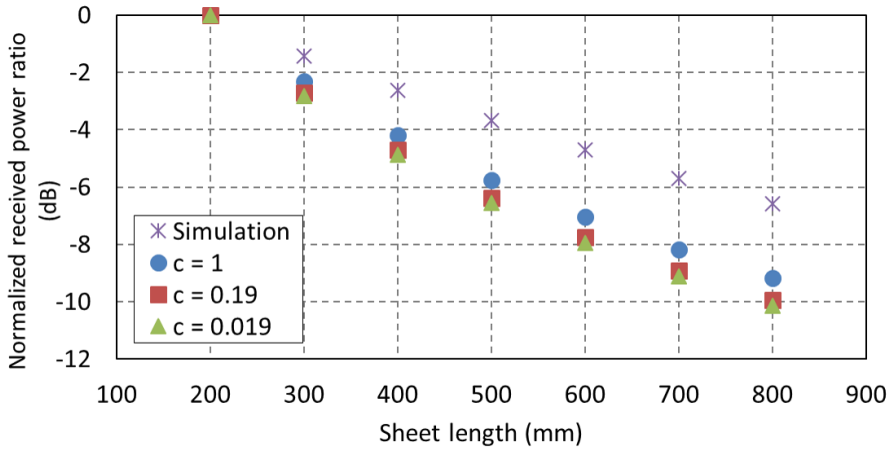

Fig. 3.8. Normalized average received power ratio. The ratio decreases with the sheet length. The deviation from the 500-mm sheet is within ±7 dB.

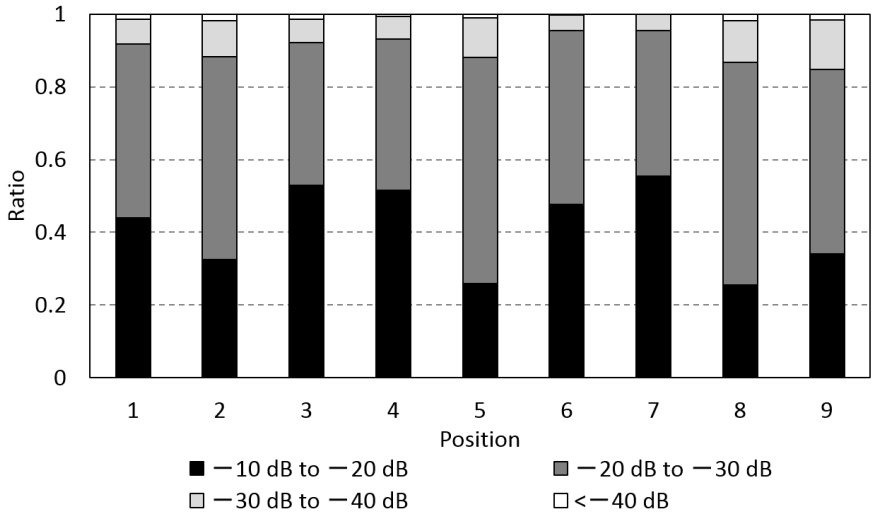

Fig. 3.9. Stacked bar graph of the transmittance of the 500 mm square sheet from 7.25 GHz to 10.25 GHz, at each position. The fraction of the number of frequency points at which the transmittance is within a particular range is denoted by the color of the bar.

on the receiving position. For example, the ratio composition of the position nearer to the center, position 1, is similar to the one of position 7, near the edge.

3.3 Experimental method

The transfer function between couplers was measured, to obtain the fundamental properties of the delay and SNR for the typical-composition sheet. The measurement method is described below.

Fig. 3.10 shows the cross-section diagram and a photograph of the experimental setup. A commercially available tile carpet (model number YS 1004, manufactured by Teijin Limited) is employed as the surface layer, with a 500 mm × 500 mm × 6 mm size. The 2DC sheet is also a 500 mm square. The mesh pitch and the line width of the inductive layer of the sheet are 4 mm and 1 mm, respectively. The material of the inductive layer and the ground layer is aluminum. The dielectric layer is a 1-mm thick polypropylene sheet. These parameters are the same as the ones used in the simulation presented in the previous section.

The inductive layer and the ground layer of the 2DC sheet are shorted at all sheet edges with a copper tape, as shown in Fig. 3.12. Even though the resistivity of the conductive adhesive layer included in the copper tape is a few orders of magnitude larger than the one of copper, we empirically confirmed that it does effectively create shorted-edges, for all practical purposes.

A circular planar coupler [56] is used as the surface coupler. The back-face coupler [61] is set under the sheet and the ground layer is in part removed around the back-face coupler to achieve a tight EM coupling between the sheet and the coupler, as shown in Fig. 3.11. These couplers are connected to the VNA (Rohde & Schwarz ZNB-20). The VNA is calibrated in unknown-open-short-match (UOSM) mode by an automatic calibration unit Rohde & Schwarz ZV-Z53. The reference planes are shown as dashed lines in Fig. 3.10(a). An inverse Fourier transform is used to obtain the time-domain data. The frequency range is 10 MHz to 10.25 GHz, which implies a delay resolution

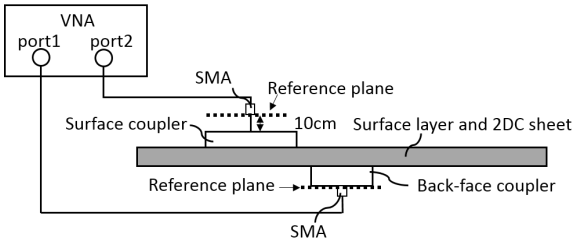

(a)

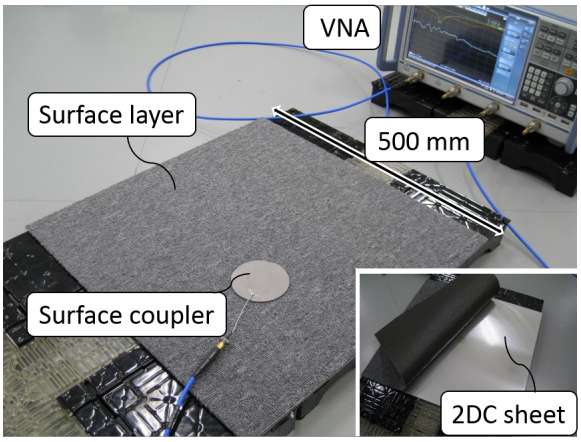

(b)

Fig. 3.10. Experimental setting. The transmittance between a surface coupler and a back-face coupler is measured at 1265 points by changing the surface coupler position and the coupler angle. (a). Cross-section diagram of the measurement setup. (b) Photo of the setup.

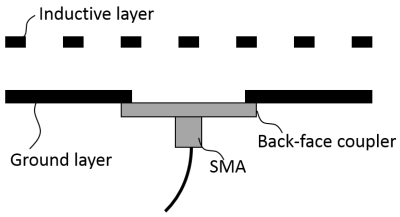

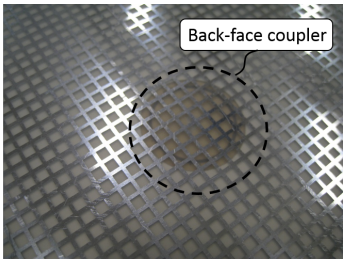

Fig. 3.11. (a) Cross-section of the back-face coupler implementation. The ground layer around the back-face coupler is eliminated to achieve resonance between the sheet and the coupler. (b) Photograph of the implementation of the back-face coupler.

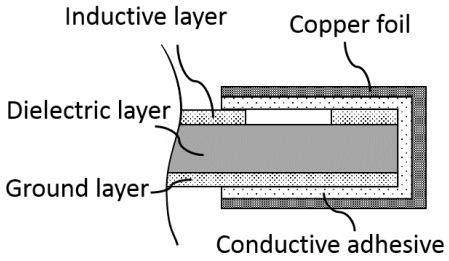

Fig. 3.12. Cross-section diagram of the shorted 2DC sheet with the copper tape.

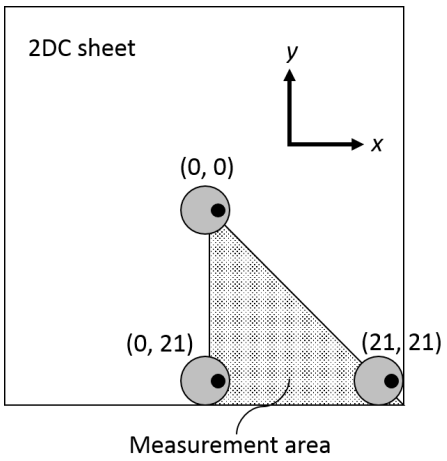

Fig. 3.13. Measurement area of the sheet. The measurement is conducted at one eight of the sheet from the point of the symmetry. The surface coupler position is changed by 10 mm and the five angles of the coupler is examined.

of 0.1 ns; in the frequency domain, 1001 measurement points are used. Considering the sheet symmetry, measurements are conducted in one eighth of the area of the sheet, as shown in Fig. 3.13. The position of the surface coupler is changed in steps of 10 mm and measurements are conducted at 253 points. Five angles of the coupler are examined, considering its directivity. The total number of measurement points is therefore 1265.

3.4 Experimental results

The impulse response of the tile at the measurement positions varies because of the sheet reflectiveness. The RMS delay spread and SNR are statistically analyzed to obtain the channel characteristics of the entire tile.

3.4.1 RMS delay spread

Fig. 3.14 shows two power delay profiles, at points $(m, n) = (0, 0)$ and $(21, 21)$. Each profile shows the exponential attenuation property. The peak in the profile of $(21, 21)$ is delayed relative to that of $(0, 0)$.

Fig. 3.15 shows the cumulative distribution function (CDF) of the RMS delay spread. The number of processed data is 1265, as mentioned above. The calculation range, 20 dB, is the same used in the simulation. In addition to the experimental result, the results based on the model with/without the radiation effect are superpositioned. The radiation effect is estimated from the additional EM simulation. The values of RMS delay spread at the CDF 0.1 and 0.9 points are 4.2 ns and 5.76 ns, respectively. These values are smaller than those obtained from the model and the simulation. The reason for this discrepancy may lie in the assumption that the signals propagate omni-direcitionally.

Table 3.2 shows the RMS delay spread values of the tile and other existing UWB channel models. In [64], the channel characteristics of three indoor environments, LOS (0-4 m), NLOS (0-4 m), and NLOS (4-10 m) are modeled. The respective RMS delay spread values are 5 ns, 8 ns, and 15 ns. In [55], the RMS delay spread ranges from 28 ns to 38 ns for LOS measurements and from 34 ns to 51 ns for NLOS measurements in an industrial environment. The measured value is therefore slightly larger than those of LOS (0-4 m) despite the smaller propagation area and LOS path. This indicates that

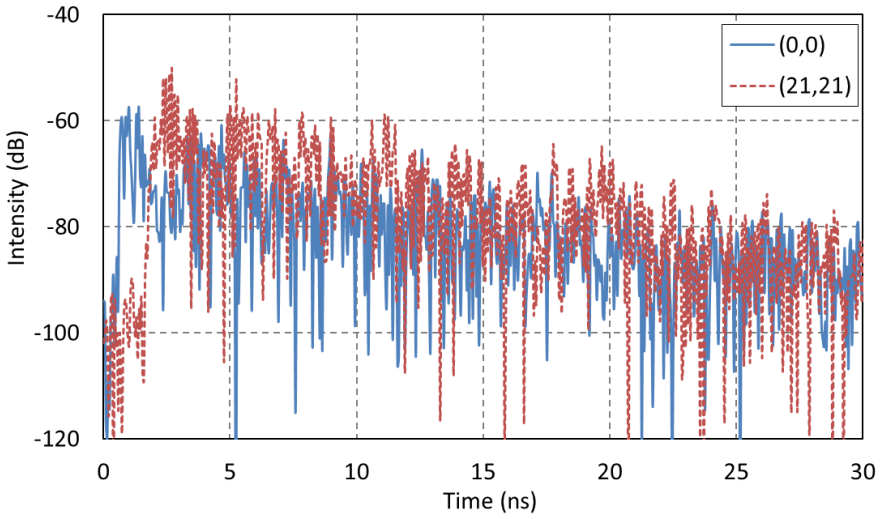

Fig. 3.14. Power delay profile of the two measurement points: (0, 0) and (21, 21). The signal arrival time reflects the distance from the signal source position.

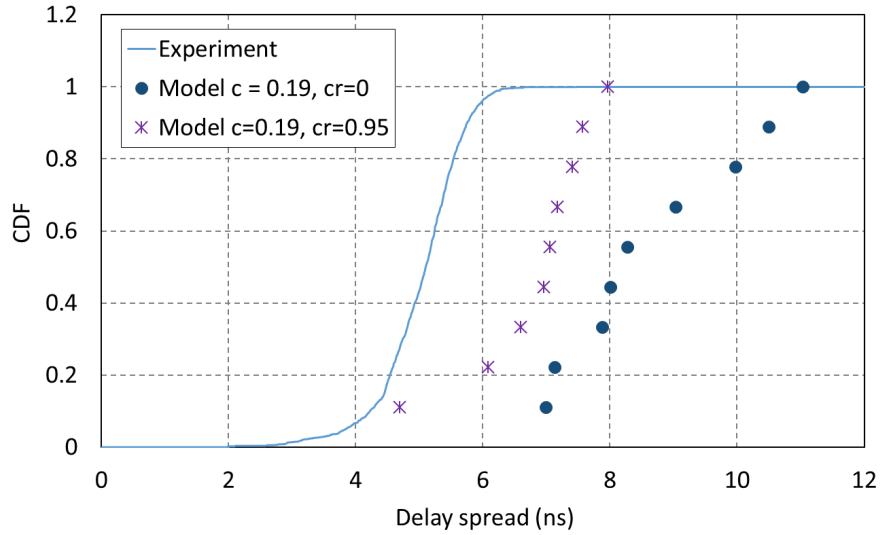

Fig. 3.15. Cumulative density function (CDF) of the RMS delay spread. The delay spread value is 5.76 ns when the CDF is equal to 0.9. The difference between the experiment and the model would be derived from the assumption that the signal attenuates omni-directionaly.

the path loss of the tile system is smaller than that of an aerial environment. On the other hand, the delay spread value of the tile is smaller than the ones of NLOS (0-4 m). In indoor communications where NLOS paths are inevitable, the tile system can provide higher-speed communications than aerial radio communications by optimizing the symbol rate.

The delay spread values of the entire system, when the multiple tiles are connected, can be estimated with that of one tile. The reason is the following. The signal transmission path from the transmitter on one of the tiles to the receiver on another tile has three parts: the source 2DC tile sheet with a transmitter, an inter-tile part with the repeater circuit,

Table 3.2. RMS Delay Spread of the UWB 2DC Tile and the Existing Channel Models

Communication environment	Delay spread
UWB 2DC tile (500 mm square, CDF=0.9)	5.76 ns
LOS (0-4 m, indoor)[64]	5 ns
NLOS (0-4 m, indoor)[64]	8 ns
NLOS (4-10 m, indoor)[64]	15 ns
LOS (industrial environment) [55]	28-38 ns
NLOS (industrial environment) [55]	34-51 ns

and the sink 2DC tile sheet with the receiver. Disregarding reflections at the inter-tile part, the delay spread of the total transmission path is therefore at most twice of that of the single tile. The transmission properties of the inter-tile part are out of the scope of this paper. In principle, we can design a non-reflective signal path for the inter-tile part, and the delay spread will then become independent of the number of the tiles.

3.4.2 Transmittance and signal-to-noise ratio

Fig. 3.16 shows the transmittances measured at three points, $(m, n) = (0, 0), (10, 10)$ and $(21, 21)$, and the simulated transmittances for the corresponding receiving points (transmission point, point 3 and point 9 in Fig. 3.4). The attenuations of free-space propagation-with the assumption of an antenna gain of 0 dB-are also shown. The measured transmittances are 20 dB lower than those of the simulation, because of the coupling losses of the back-face coupler and the surface coupler.

The results are comprehensible and consistent with the theoretical predictions, as follows. As expected, the transmittance in the tile decreases more gradually with distance than free-space propagation. This characteristic provides an almost constant SNR over the sheet surface. On the other hand, the significance of the multi-reflected components when compared with the direct path component depends on the receiver position. This is indicated by the frequency-selective fading shown in Fig. 3.16. Some deep fades are observed at $(10, 10)$, whereas no deep fades are generated at $(0, 0)$. This is because the direct signal at $(0, 0)$ is much stronger than the multipath signals and the intensity of the multipath signals becomes closer to the direct one when the receiving point is farther away from the source.

Fig. 3.17 shows the CDFs of the fraction of the sum of bandwidths where the SNR (the margin to the thermal noise calculated by Eq. (3.7)) is higher than 20 or 30 dB. The SNR is 20 dB or greater in 80% of the UWB high-band (7.25 GHz-10.25 GHz), over the entire tile. In almost 50% of the tile area, an SNR $>$ 30 dB is achieved in 70% of the entire bandwidth.

3.5 Time domain characteristics of multiple 2DC tiles

In this section, the time domain characteristics of the tile system where the multiple tiles are implemented. Signal flow of the tile system helps the estimation of the characteristics of the entire system. First, the system is modeled and simulated. The experiment, then is conducted to verify the model.

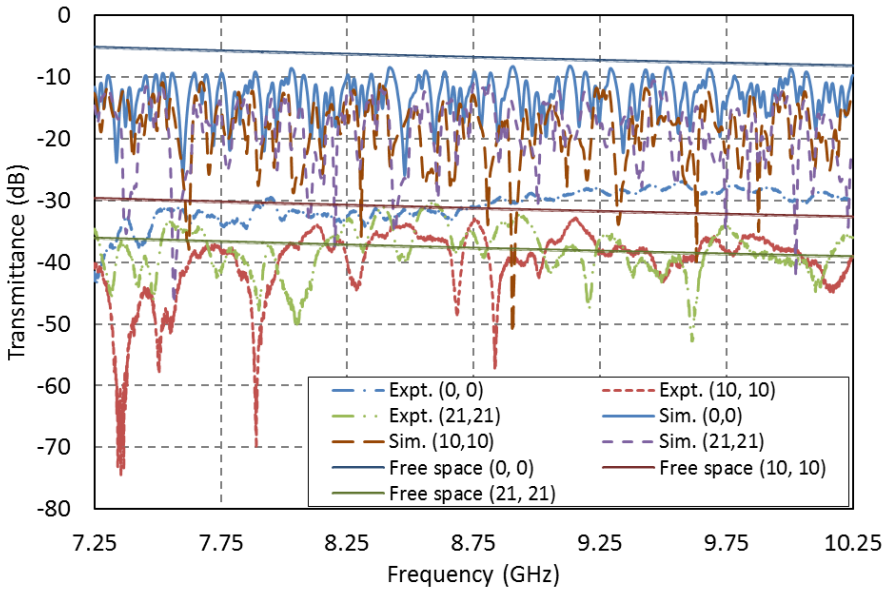

Fig. 3.16. Transmittance of the three measurement points: (0, 0), (10, 10), and (21, 21) and the attenuation of free-space propagation based on Frii's transmission equation and the assumption of an antenna gain of 0 dB at the same points. Dips are generated due to the standing wave. Transmittance decreases with distance more gradually than the free-space propagation.

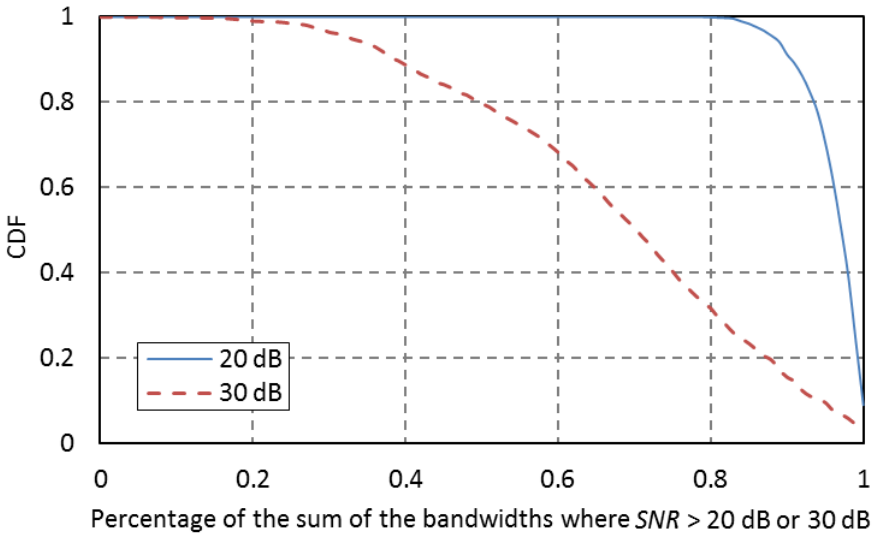

Fig. 3.17. Cumulative density function of the ratio of the bandwidths where SNR is more than 20 dB or 30 dB to all of the bandwidths. There is 20 dB margin in 80% of the UWB high-band at all most all the measurement points. This result indicates that a low BER communication in QPSK or 16QAM modulation is possible with sufficient bandwidth.

3.5.1 Signal propagation model

Fig. 3.18 shows the model of the signal propagation mentioned above. The input signal $x(t)$ to the tile system propagates in the source tile that corresponds to Tile 1 and some of them are transmitted to the sink tiles, Tile 2 and Tile 3, through the base layer. The received signal of another coupler at the source tile $y_{\mathrm{source}}(t)$ is described as follows.

$$y_{\mathrm{source}}(t) = x(t) * h(t). \tag{3.11}$$

$h(t)$ denotes an impulse response of the tile. For a simple and rough estimation, we assume that all of the following three types of paths show the same impulse response: 1) from the transmitter surface coupler (Tx coupler) to the receiver surface coupler (Rx coupler) on the source tile, 2) from the Tx coupler to the back-face coupler on the source tile, and 3) the back-face coupler to the Rx coupler on the sink tile. Because the input signal to each sink tile is $y_{\mathrm{source}}(t)$ and the tiles have the same impulse response, the received signal $y_{\mathrm{sink}}(t)$ of each coupler put on Tile 2 and Tile 3 is the same and expressed as

$$y_{\mathrm{sink}}(t) = h(t) * (x(t) * h(t)). \tag{3.12}$$

No reflections among the tile connections are assumed in Eq. 3.12. The number of the impulse response that the signals propagate from the source tile to the sink tile is the same among the sink tiles. Therefore, the communication characteristics of the overall system can be estimated with the one-tile property as shown in Eq. 3.12.

3.5.2 Numerical simulation of the RMS delay spread

The RMS delay spread is numerically simulated with the model to quantitatively evaluate a relation between the delay spread of the source tile and that of the total path. In the UWB 2DC tile, multipath signals are generated because the tile has reflective characteristics. Since the impulse response of the multipath environment is generally expected to have exponential-attenuation property [62], the impulse response in the simulation is assumed as

$$h(t) = \mathrm{e}^{-\alpha t}. \tag{3.13}$$

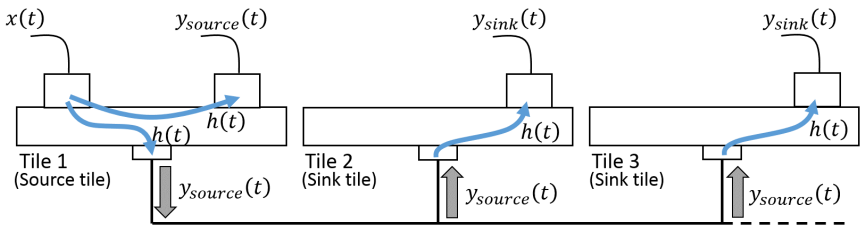

Fig. 3.18. Schematic diagram of the tile-system model. An impulse response of three paths: from the transmitter surface coupler to another surface coupler or the back-face coupler on the source tile and from the back-face coupler to the receiver surface coupler on the sink tile, is assumed to be the same. Input signals to each sink tile from the back-face couplers are the same. Therefore the received signals of each tile are also the same.

where α denotes decaying factor. If the input signal $x(t)$ is an ideal impulse and the impulse response is expressed as Eq. (3.13), $y_{\mathrm{source}}(t)$ and $y_{\mathrm{sink}}(t)$ can be numerically simulated as shown in Fig. 3.19. An important index of the channel characteristics in time domain is the RMS delay spread. It represents how long signals spread by propagating the communication environment and is considered to avoid ISIs when designing the physical layer protocol. The RMS delay spread is calculated with Eq. (3.2)-(3.4).

We define the RMS delay spread of the identical tile path, from the surface coupler to another coupler as τ_{source}, and that of the total path, from the surface coupler on the source tile to the surface coupler on another sink tile as τ_{sink}. τ_{source} and τ_{sink} are 182 time steps and 257 time steps respectively from the simulation results shown in Fig. 3.19. The delay spread of the entire system τ_{total} is equal to τ_{sink} because all of the sink tiles show the same delay spread. Therefore τ_{source} and τ_{total} are estimated to have the relation of

$$\tau_{\mathrm{total}} \simeq 1.41\tau_{\mathrm{source}}. \tag{3.14}$$

This result shows that the delay spread of the entire system is easily estimated if that of one tile is known.

3.5.3 Evaluation of RMS delay spread of multiple UWB 2DC tiles

In this section, the relation of the delay spread between the tiles is examined by the measurement of the time domain signals with two patterns to verify the simulation results. First, the source tile and the sink tile are measured, then two sink tiles are measured.

Source tile and sink tile

Fig. 3.20 shows the schematic diagram and the photo of the measurement setup. Two tiles are connected with the back-face couplers set under the ground layer of the 2DC sheet as shown in Fig. 3.11. The base layer are not implemented because influences of

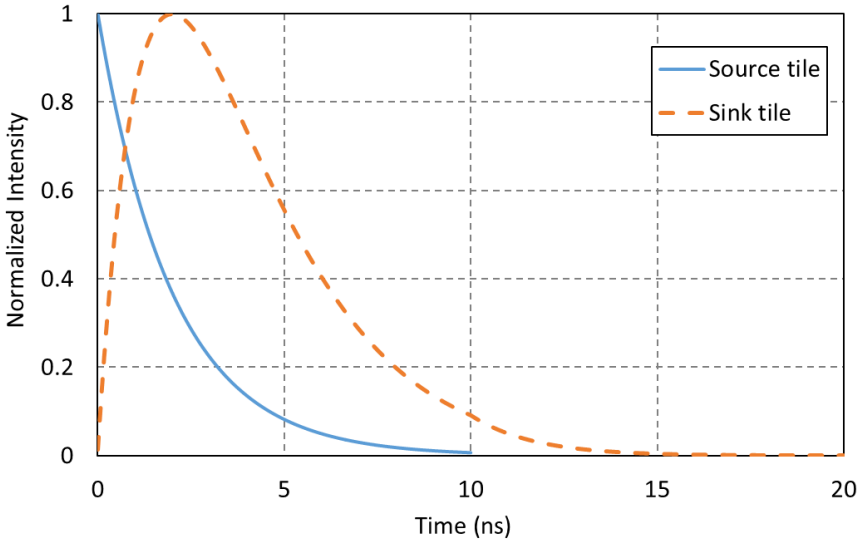

Fig. 3.19. Simulation result of received signal y_{source} at the source tile and y_{sink} at the sink tile. It is assumed that the input signal is be an ideal impulse and the impulse response of the tile has exponential-attenuation characteristics. α in Eq. (3.13) is 0.5.

the buffer circuit and the interfaces is avoided. The couplers [61] are used as the surface coupler. They are connected to a vector network analyzer (VNA), Rhode & Schwarz ZNB-20. The inverse Fourier transform technique is used to obtain time domain signals from the measurement results. A frequency range is from 10 MHz to 10.25 GHz and the number of sweep points are 1001. These settings indicate time resolution and available time span are about 0.05 ns and 50 ns, respectively. Two signal paths are examined, 1) from the surface coupler on the source tile to another surface coupler on the source and 2) from the surface coupler on the source tile to one on the sink tile. The five-hundred measurements are conducted at a half area of each tile in the consideration of symmetry of the sheet. A composition of the 2DC sheet is as follows. The sheet size is 500 mm square. A line width and a pitch of the inductive layer are 1mm and 4mm respectively.

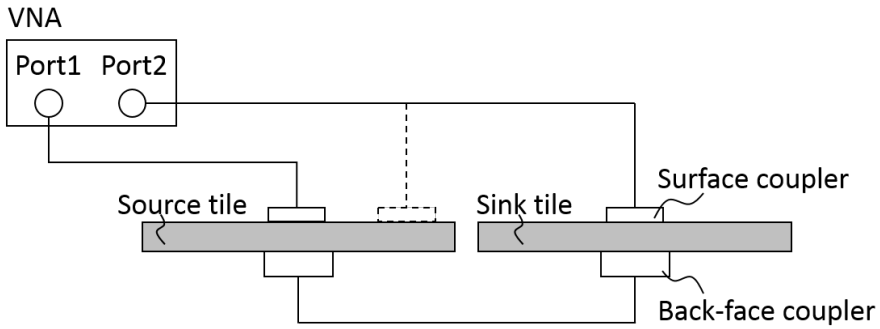

(a)

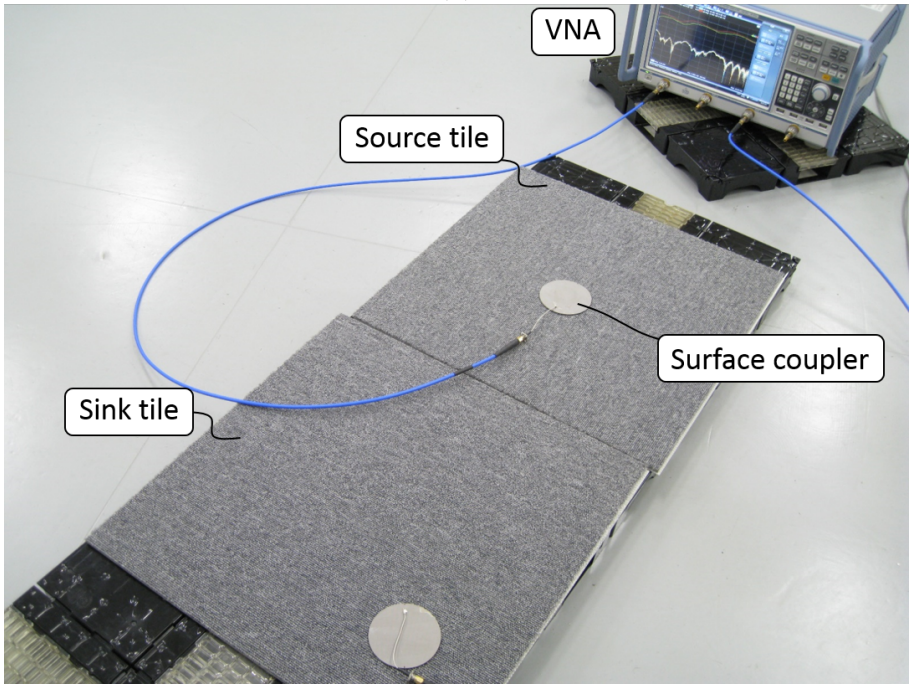

(b)

Fig. 3.20. (a) Schematic diagram of measurement setup. The measurement is conducted to obtain signal propagation data of two paths: 1) from the surface coupler on the source tile to surface coupler on the sink tile and 2) from the surface coupler to another surface coupler on the source tile. The tiles are connected with the back-face couplers under the ground layer. (b) Photo of the setup.

A material of the inductive layer and the ground layer is aluminum. Thickness and the material of the dielectric layer is 1mm and polypropylene whose relative permittivity is 2.1. These sheet settings are employed from the point of performance and availability and are typical in our previous works. In this experiment, the edge of the sheet is open. This is not critical because the open edge also has reflective property. The surface layer of the tile is a commercial carpet tile, the model number YS 1004 manufactured by Teijin Limited. The size is 500 mm×500 mm×6 mm.

Fig. 3.21 shows the examples of the measured power delay profile in dB unit. The signals of Source tile has exponential characteristics and the received signals of Sink tile are more gradually excited compared to Source tile. These properties match with the numerical simulation. Fig. 3.22 shows cumulative density function (CDF) of the RMS delay spread. Table 3.3 shows the statistical delay spread values and a ratio of the delay spread of Sink tile to that of Source tile. $\tau_{rms}, 10\%$, $\tau_{rms}, 90\%$, and $\tau_{rms}, 100\%$ denote the RMS delay spread values when the CDF is equal to 0.1, 0.9, and 1. The

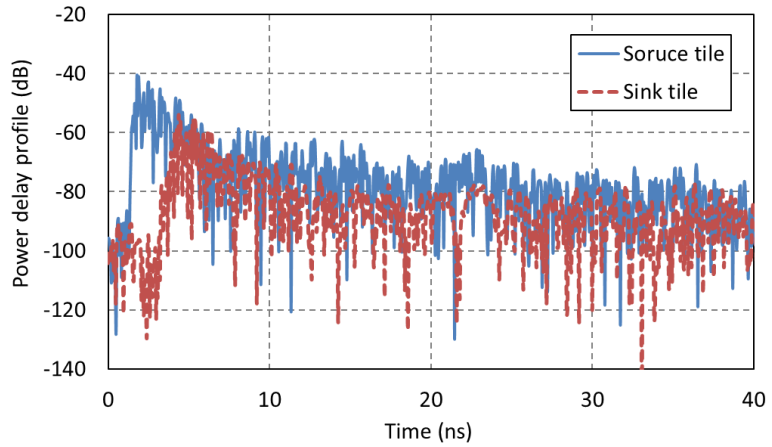

Fig. 3.21. Examples of the power delay profile of the two tiles. The signal of sink tile rises more gradually than that of source tile. This trend corresponds to the simulation result.

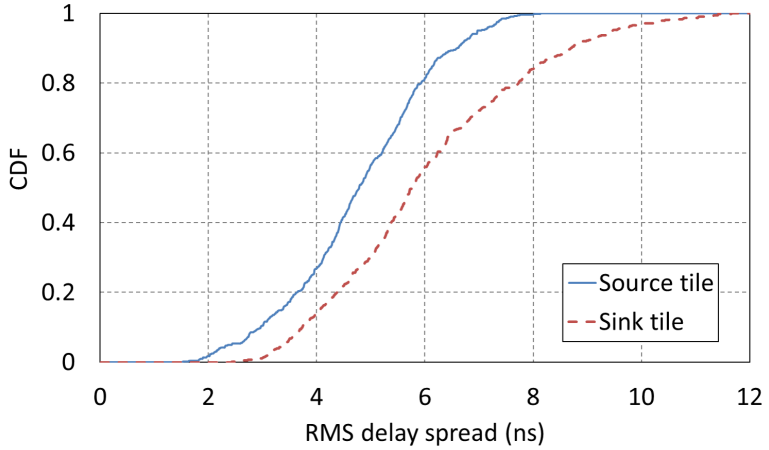

Fig. 3.22. Cumulative density function (CDF) of the RMS delay spread of source tile and sink tile. The delay spread values of source tiles is shorter than that of sink tile.

Table 3.3. Statistics of the RMS delay spread of the source tile and the sink tile

	$\tau_{rms}, 10\%$ [ns]	$\tau_{rms}, 90\%$ [ns]	$\tau_{rms}, 100\%$ [ns]
Source tile	2.97	6.6	8.14
Sink tile	3.74	8.7	11.67
Ratio	1.26	1.32	1.43

value of $\tau_{rms}, 100\%$ is almost the same as that of the simulation results and the other results are also comparable. These results show the consistency between Eq. 3.14 and the experimental results. Therefore, the relation of the delay spread between the source tile and the neighboring tiles are ensured.

Two sink tiles

This measurement is conducted to ensure the relation among the delay spread value of the multiple sink tiles. Because the signals among the sink tiles are theoretically the same, the RMS delay spread values are considered to be the same or comparable.

Fig. 3.23 and Fig. 3.24 show the schematic diagram and the photo of the measurement setup. Three tiles are used, one is the source tile and the others are the sink tiles. The same signal power is provided to Sink tile 1 and Sink tile 2 by using a divider.

The VNA settings and the composition of the tiles are the same as the former experiment. The transmittances between Source tile and Sink tile 1 and between Source tile and Sink tile 2 are measured at 500 points in the half area of each tile. Then the data are processed to time domain signals.

Fig. 3.25 shows examples of the measured power delay profiles at the same position of the two sink tiles. The similar profiles indicate the similar signals are input to the sink tiles. Fig. 3.26 shows the CDF of the delay spread. The trend is almost comparable with each other. Table 3.4 shows the statistical delay spread values. These values indicate that the delay spread of Sink tile 1 and 2 is almost the same and also indicate the consistency with the former experiment results. Therefore the delay spread values of the multiple sink tiles can be considered to be the same and have the same relation with the source tile.

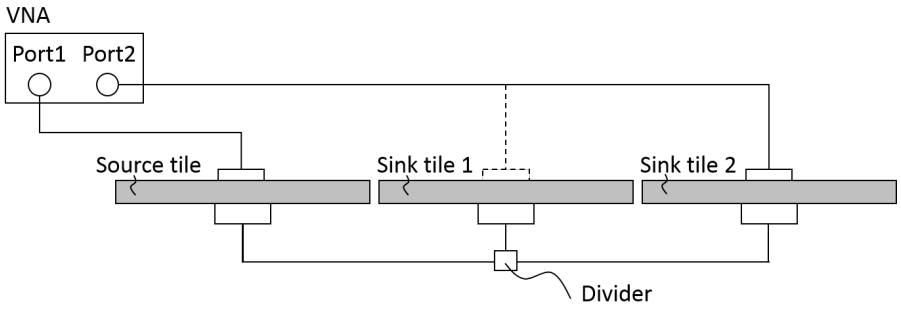

Fig. 3.23. Schematic diagram of the measurement setup. A divider is used to provide the signals to sink tile 1 and 2.

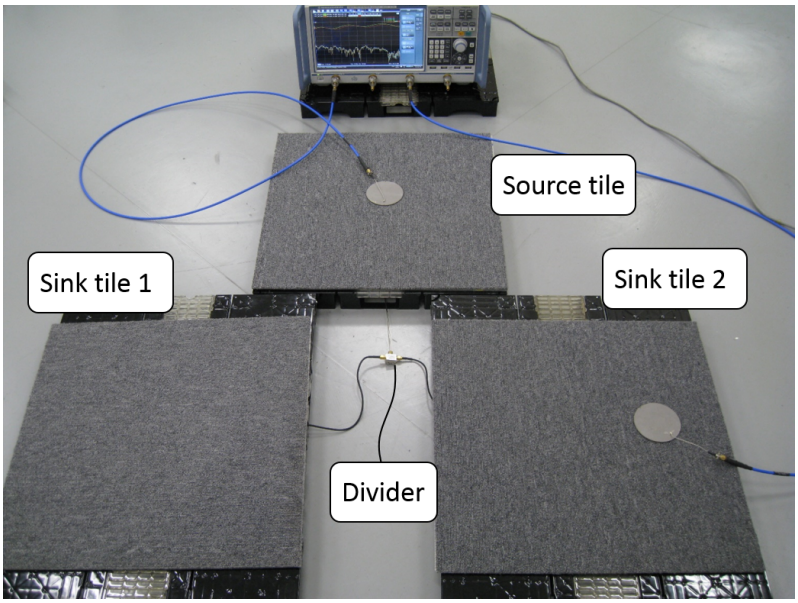

Fig. 3.24. Photo of the measurement setup.

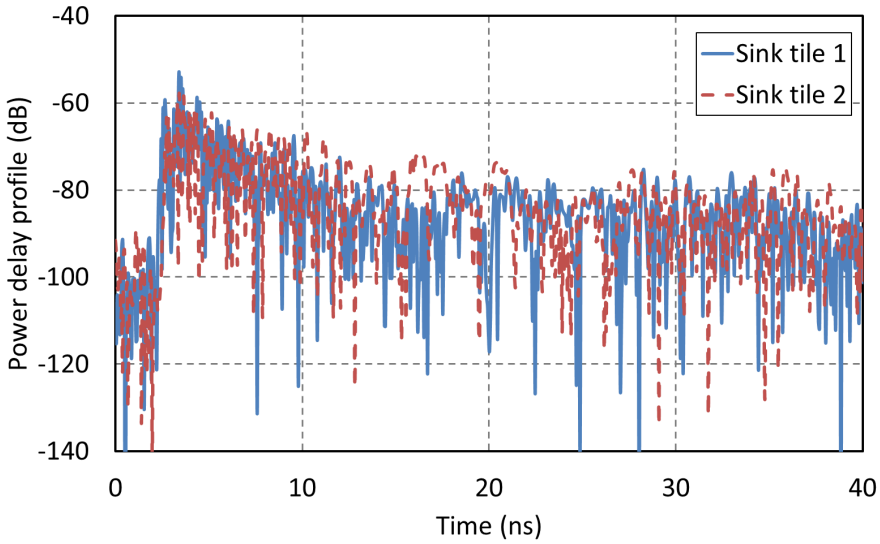

Fig. 3.25. Examples of the power delay profiles of the two sink tiles. The sample points on the tiles are the same. The similar trend indicates the same signals are input to the tiles.

3.6 Adaptability to existing protocols

The former sections clarified the fundamental properties of the tile system. The obtained properties enables to design an optimized physical layer protocol and evaluate adaptability of existing protocols to the tile system. The adaptability to existing protocols is evaluated by both the RMS delay spread and the SNR. One of the communication schemes in UWB technology is MB-OFDM. The length of the guard interval employed in MB-OFDM is 60 ns, and the delay spread must be shorter than this interval to avoid inter-symbol

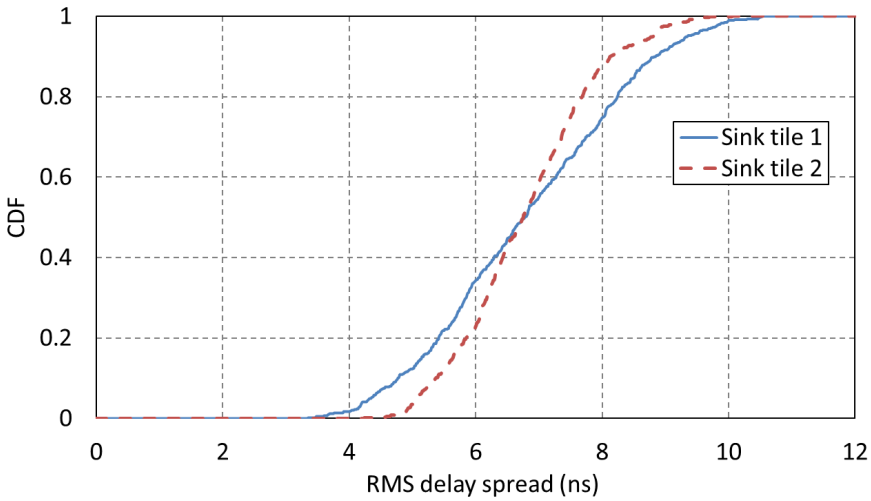

Fig. 3.26. Cumulative density function of the two sink tiles. The trend of both tiles is similar.

Table 3.4. Statistics of the RMS delay spread of the two sink tiles

	$\tau_{rms}, 10\%$ [ns]	$\tau_{rms}, 90\%$ [ns]	$\tau_{rms}, 100\%$ [ns]
Sink tile1	4.77	8.85	10.53
Sink tile2	5.37	8.13	10.06

interference. A delay spread smaller than 14 ns in total will be achieved by a multi-tile system using the available components presented in this paper.

One of advantages in OFDM is simple equalization. Unlike conventional equalization for a single-carrier modulation, equalizaiton in OFDM is one multiplication of a constant complex value. Bandwidth of subcarriers that is narrower than coherence bandwidth enables the simple equalization. The coherence bandwidth is a bandwidth where fading property of a communication environment is considered to be flat dispite a multipath environment. Since the 2DC sheet is multipath environment, frequency-selective fading is generated. In such an environment, evaluation from the viewpoint of coherence bandwidth is important for consideration of adaptability of protocols.

The 50 % coherence bandwidth is a criterion to evaluate the fading type and is expressed as below [65].

$$B_{c,50\%} = \frac{1}{5\sigma_{\mathrm{rms}}}, \tag{3.15}$$

where σ_{rms} denotes a RMS delay spread. In the case of the tile system, $B_{c,50\%} = 14\mathrm{MHz}$. Since a subcarrier bandwidth of MB-OFDM is 4.125 MHz, the fading occurred in each subcarrier is considered to be flat-fading.

The typical modulation in MB-OFDM is quadrature phase shift keying (QPSK). With an SNR $>$ 20 dB, the BER is expected to be less than 1×10^{-6} across the whole tile area with QPSK modulation. Although 16-quadrature amplitude modulation (16-QAM)-which has twice the number of bits per symbol of QPSK-requires a higher SNR to achieve the same BER as QPSK, its BER will also be lower than 1×10^{-6} under the SNR $>$ 20 dB condition. The data rate of the tile system, therefore, will be more than twice that of MB-OFDM if the modulation is changed to 16-QAM and the guard interval is adjusted

to the RMS delay spread of the tile system.

3.7 Conclusion

In this section, the communication characteristics of the UWB 2DC tile was clarified. These characteristics is necessary to design a physical layer protocol or determine availability of existing communication schemes. First, we modeled the signal propagation based on a geometrical property that the sheet is a precise square. A signal transition of the model indicates reasonable agreement with that of the EM simulation. A trend of the RMS delay spread with sheet length is in a linear trend and the deviation between a 200-mm sheet and a 800-mm sheet is about 8 ns.

As the next step, we statistically analyzed the fundamental properties of the 500-mm typical composition sheet with 1265-point measurements. The results show that the RMS delays spread is mainly distributed from 4.2 ns to 5.76 ns and the SNR is 20 dB or more at almost all the sheet area in 80% of the UWB high band. The RMS delay spread value of the sheet is longer than that of a comparable-area LOS environment, but is shorter than that of a comparable-area NLOS environment. These results enable the design of the physical layer protocol for a 2DC tile system with the currently available components and also indicate that the characteristics of the tile are acceptable for combination of QPSK and MB-OFDM modulations, which are one of the standard techniques for UWB radio.

Time domain characteristic of the entire 2DC tile system where multiple tiles are connected was also clarified. The signal propagation in the whole system was modeled and the RMS delay spread was calculated with a numerical simulation. On the condition that the reflection between the tiles are negligible, the delay spread value is calculated when signals propagate two tiles. The result shows that the RMS delay spread of the entire system is about 1.41 times longer that of one tile. To verify this relation, measurements were conducted with two settings: 1) the source tile and the sink tile, 2) the source tile and the two sink tiles. The experimental results showed the consistency with the numerical simulation result.

From these results, the delay property of the tile system is constant regardless of the system size is shorter when propagation area is a room-size. These properties indicate that high-speed communication is possible by designing the specialized physical layer protocol for the tile system.

Chapter 4

Suppression of radiation from the tile

In the 2DC, no energy is emitted into the air in the case of an infinite-length sheet. In practice, however, some amount of energy is emitted due to a finite sheet length. This radiation decreases signal-to-interference-plus-noise ratio (SINR). When each tile of the entire tile system receives signals in the air, SINR becomes lower. For reliable communication, high SINR is necessary and the radiation from the sheet should be suppressed. In this section, the radiation is modeled and the suppression method are presented.

4.1 Effect of the radiation to the communication

The SNR is one of index to represent a quality of a received signal. In the former chapters, thermal noise is taken into account as a noise source. Since all undesirable signals causes interferences, they are also regarded as noise sources. The index that includes radio signals as interference sources is called as signal-to-interference-plus-noise ratio (SINR) and is defined as below.

$$SINR = \frac{P}{I+N}, \tag{4.1}$$

where P, I, and N denote a received signal power, an interference signal power, and a noise power. Note that P includes I and N. High interference signal power decreases SINR, and bit-error-rate (BER) becomes lower. In the tile system, multiple tiles are deployed. Since each tile operates as a kind of an antenna, an interference power I becomes larger as the number of implemented tiles increases. Therefore, heightening the immunity of the tile, therefore, is important to achieve a reliable communication system.

4.2 Radiation from the tile

The transmittance between the sheet and an antenna in the air is measured to ensure the radiation from the sheet.

4.2.1 Vertical direction

Fig. 4.1 and Fig. 4.2 show a schematic diagram and a picture of the experiment. In this experiment, one tile is examined to clarify the tile property. The feeding coupler set to the tile and a whip antenna whose return loss at 8.2 GHz is about -12 dB are connected to the vector network analyzer, Rhode & Schwarz ZNB-20. The transmittance is measured by changing the vertical distance between the tile and the antenna from 0 mm to 1000 mm. The position of 0 mm from the tile corresponds to that of 6 mm from the 2DC sheet in the tile because thickness of the surface layer is 6 mm. Both the open boundary sheet and the shorted one shown in Fig. 4.3 are examined. The short boundary sheet is

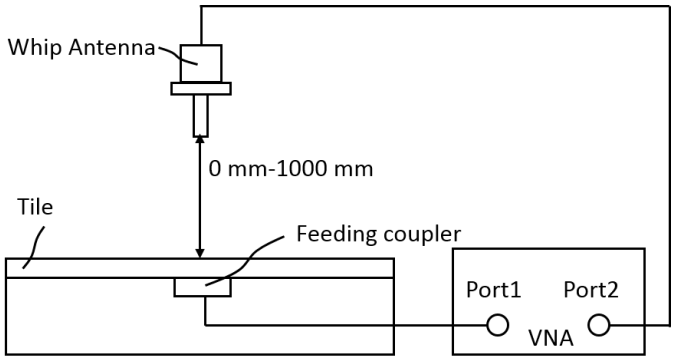

Fig. 4.1. Schematic diagram of the experimental setting. The gap distance between the sheet and the whip antenna is changed from 0 mm to 1000 mm. The attitude of the antenna is set so that the electromagnetic field of the antenna is matched to that of the sheet and the antenna is set at the center of the sheet.

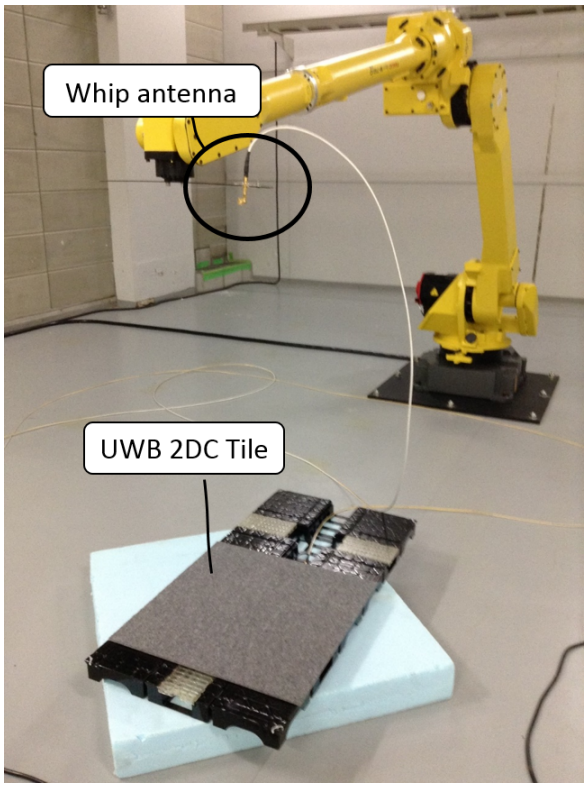

(a)

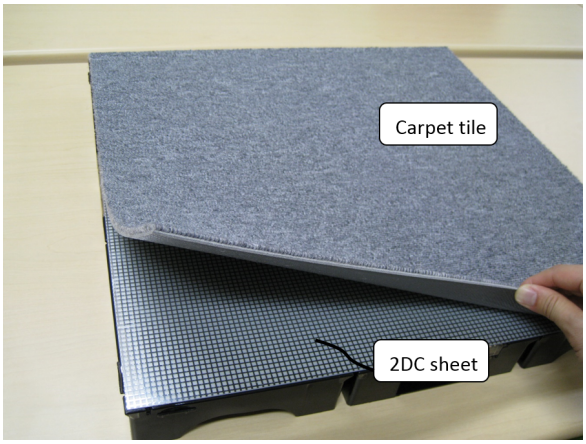

(b)

Fig. 4.2. Photo of the experimental setting. (a) The overview. (b) Enlarged picture of the tile.

experimentally fabricated by shorting the inductive layer and the ground layer of the open boundary sheet with copper tapes. In this experiment, the base layer is not implemented because only one tile is examined.

The composition of the 2DC sheet of the tile is as follows. The size of the sheet is 500 mm $\times$500 mm $\times$ 1 mm. The line width and the pitch of the inductive layer are 1mm and 4 mm respectively, which are the same as the numerical simulation. The material

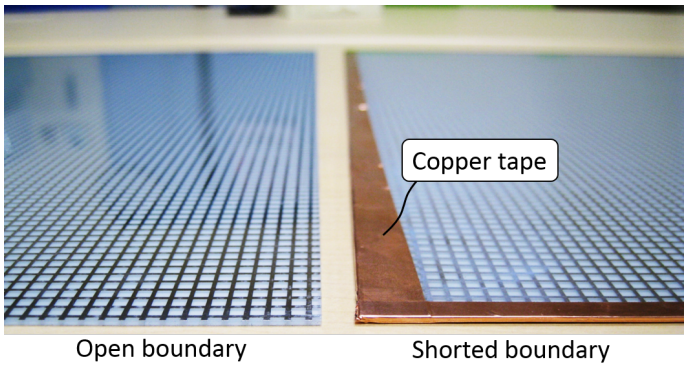

Fig. 4.3. Photo of the open-boundary 2DC sheet and the shorted one. Copeer taper are used to short the inductive layer and the ground layer.

of the inductive layer and the ground layer is aluminum. The 1 mm-thick polypropylene sheet is used as the dielectric layer. The feeding coupler is set under the ground layer to excite/extract signals to/from the sheet. The return loss at 8.2 GHz of this coupler is about −18 dB. The aluminum sheet around the feeding coupler is eliminated to establish the proximity connection between the sheet and the feeding coupler as shown in Fig. 8. The carpet tile, the model number YS 1004 manufactured by Teijin Limited, is employed as the surface layer. The size of this carpet tile is 500 mm×500 mm×6 mm. As the attitude of the antenna is shown in Fig. 4.1, a rod is perpendicular to the tile to match polarization so that the antenna and the sheet can be easy to resonate. The electric field $\boldsymbol{E}$ and the magnetic field $\boldsymbol{H}$ in the 2DC sheet are normal and tangential to the sheet, respectively and the direction of the wavenumber vector $\boldsymbol{k}$ is perpendicular to both fields as shown in Fig. 4.4.

Fig. 4.5 shows the experimental results. Each plot indicates an average of ten measurements. The transmittance decreases rapidly from 0 mm to 100 mm and gradually from 100 mm to 1000 mm in both boundaries. The former characteristics are derived from near field radiation and the latter are derived from far field radiation. The transmittance at more 600 mm gap distance is about −60 dB or less while about −20 dB at 0 mm. Based on Friis transmission equation, propagation loss of 8.2 GHz signals in free-space is −46.3 dB at 600 mm between measurement points. In the case that the directivity of the whip antenna is 0 dBi in a radiation plane, the antenna gain of the sheet is calculated as −13.7 dBi, which indicates the sheet has the high-isolation property.

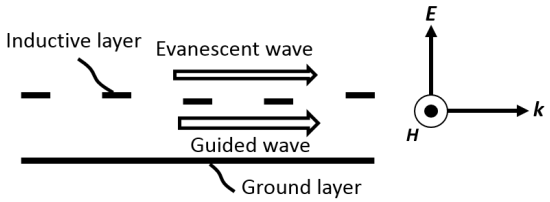

Fig. 4.4. Electromagnetic fields of waves propagated in the 2DC sheet. The electric field $\boldsymbol{E}$ of signals in the sheet is normal to the sheet and the magnetic field $\boldsymbol{H}$ is tangential. The wavenumber vector $\boldsymbol{k}$ is perpendicular to both fields.

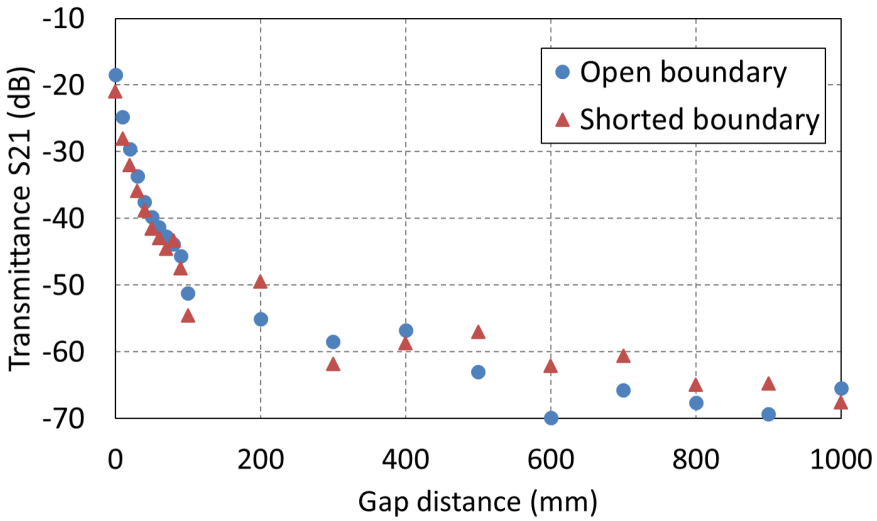

Fig. 4.5. Transmittance between the 2DC sheet and the antenna along vertical direction.

4.2.2 Azimuth and elevation angle

Fig. 4.6 shows the experimental condition. The antenna and the tile are the same as the former experiment. The connection of them to the VNA is also the same. The antenna is set at 1000 mm from the center of the tile where the radiation pattern can be considered as far field based on the result of the former section because the radio signals arriving to the tile via the air are the far-field signals. The attitude of the antenna is controlled so that the rod can be perpendicular to the line between the antenna and the center of the tile. Elevation angle θ is changed from 0 degree to 90 degree. Azimuth angle ϕ is set to 0

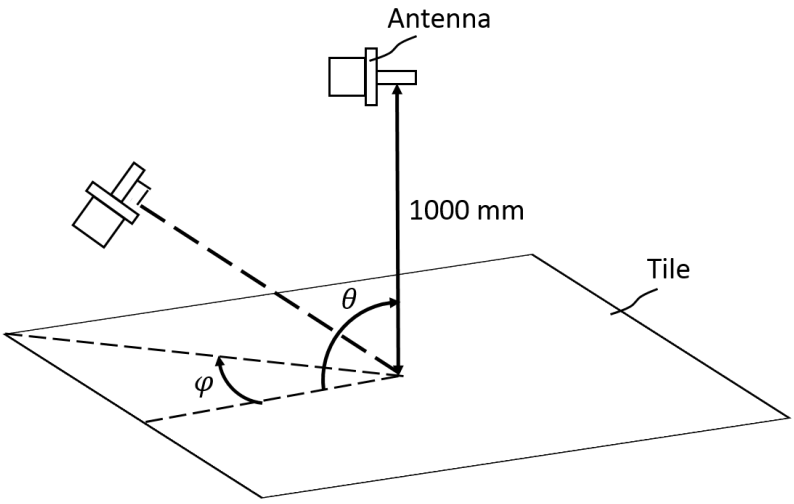

Fig. 4.6. Schematic diagram of the experimental setup. The antenna is set at 1000 mm from the center of the tile. The transmittance is measured with 0 degree and 45 degree of azimuth angle ϕ and elevation angle θ from 0 degree to 90 degree. The attitude of the antenna is changed so that the rod can be perpendicular to the line between the antenna and the center of the tile.

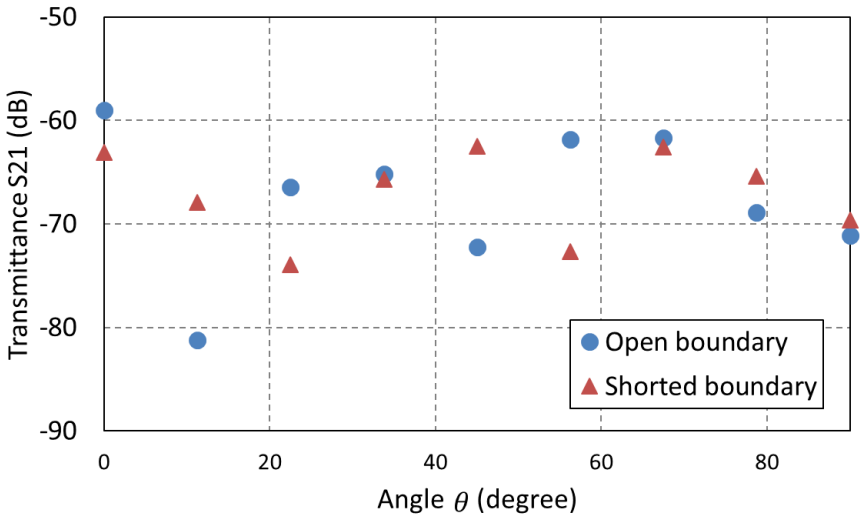

Fig. 4.7. Transmittance S21 between the 2DC tile and the antenna at $\phi = 0$ degree.

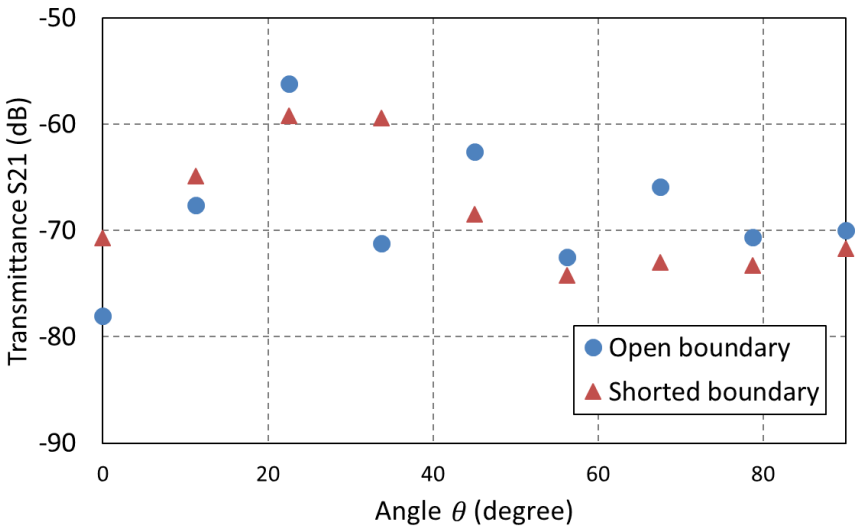

Fig. 4.8. Transmittance S21 between the 2DC tile and the antenna at $\phi = 45$ degree.

degree or 45 degree. The setting of more than 45 degree in azimuth angle is not measured due to the symmetric property of the tile.

Fig. 4.7 and Fig. 4.8 show the experimental results for $\phi = 0$ degree and 45 degree respectively. Both results show that there is not a strong relationship between the transmittance and the boundary condition, and the transmittance is about -60 dB or less at almost all angles in both boundaries. Therefore UWB 2DC tile also has high-isolation performance along azimuth and elevation angle with both boundaries.

4.2.3 Discussion

The experimental results show that there is not the clear difference of the isolation performance in the far field between both boundaries. This seems inconsistent with the simulation result that microwaves leak from the open boundary sheet in near field. The

reason should be clarified in our future work. The experimental results also show that the transmittance between the sheet and the antenna is −60 dB at 600 mm and −20 dB at 0 mm from the tile. Signals from the surface of the tile has the margin of 40 dB from the signals at 600m above the tile. If the dedicated coupler is put on the tile instead of the antenna, more margin can be obtained. This high-isolation property of the sheet makes coexistence with radio signals feasible. The tile system enables the coexistence but the far field characteristics as well as the near field are observed as shown in Fig. 4.5. In 2DC, theoretically little microwaves are radiated in the far field because only the evanescent field is generated from the sheet. This is considered that the sheet is finite size and has the edge.

4.3 Radiation model

The former section shows that some microwaves are emitted into the air from the sheet although the antenna gain of the sheet is low and that value is - 10dB. In this section, the radiation model from the sheet [67] is described.

The three variations of the radiation from the sheet are considered as shown in Fig. 4.9. One is the radiation from the gap between the inductive layer and the ground layer. This radiation is suppressed by shorting the two layers [32]. Other is the radiation at the edge of the inductive layer caused by impedance discontinuity between the periodic mesh and the sheet edge. The radiation by the impedance discontinuity is reduced by adding the gradual transition structure to the sheet edge [66]. The other is the radiation from the periodic mesh. The lowest TM mode wave guided in the 2DC sheet generates a surface current on the top layer. The surface current can be regarded as a set of a current element. Each current element constitutes a magnetic field at a far-field zone. The total of the magnetic field is expected to correspond to the radiation component.

In this section, the radiation derived from the periodic mesh, especially at the far-field zone, is focused on. Fig. 4.10 (a) shows an analytical model of the 2DC sheet. The EM wave is travelling in $+x$-direction and is constant in the y-direction, that is the EM wave propagation is treated as the two-dimensional problem. This assumption is reasonable because the sheet consists of multiple periodic mesh patterns. The electric field and the magnetic field inside the sheet are expressed as $\boldsymbol{E_s}$ and $\boldsymbol{H_s}$ and the evanescent electric field $\boldsymbol{E}$ and $\boldsymbol{H}$ are generated due to the EM field inside the sheet. No reflection at the sheet edge occurs with the impedance matching. Based on a property of the TM wave, the evanescent field is described as follows.

$$\boldsymbol{E} = \begin{pmatrix} E_x \\ 0 \\ E_z \end{pmatrix}, \boldsymbol{H} = \begin{pmatrix} 0 \\ H_y \\ 0 \end{pmatrix} \tag{4.2}$$

The original EM field shown in Eq. (4.2) corresponds to a magnetic field density $\boldsymbol{M}$, an electric field density J, and an electric charge density q on the ground as expressed as below.

$$\boldsymbol{M} = \boldsymbol{E} \times \boldsymbol{n} = \begin{pmatrix} 0 \\ -E_x \\ 0 \end{pmatrix} \tag{4.3}$$

$$\boldsymbol{J} = \boldsymbol{n} \times \boldsymbol{H} = \begin{pmatrix} H_y \\ 0 \\ 0 \end{pmatrix} \tag{4.4}$$

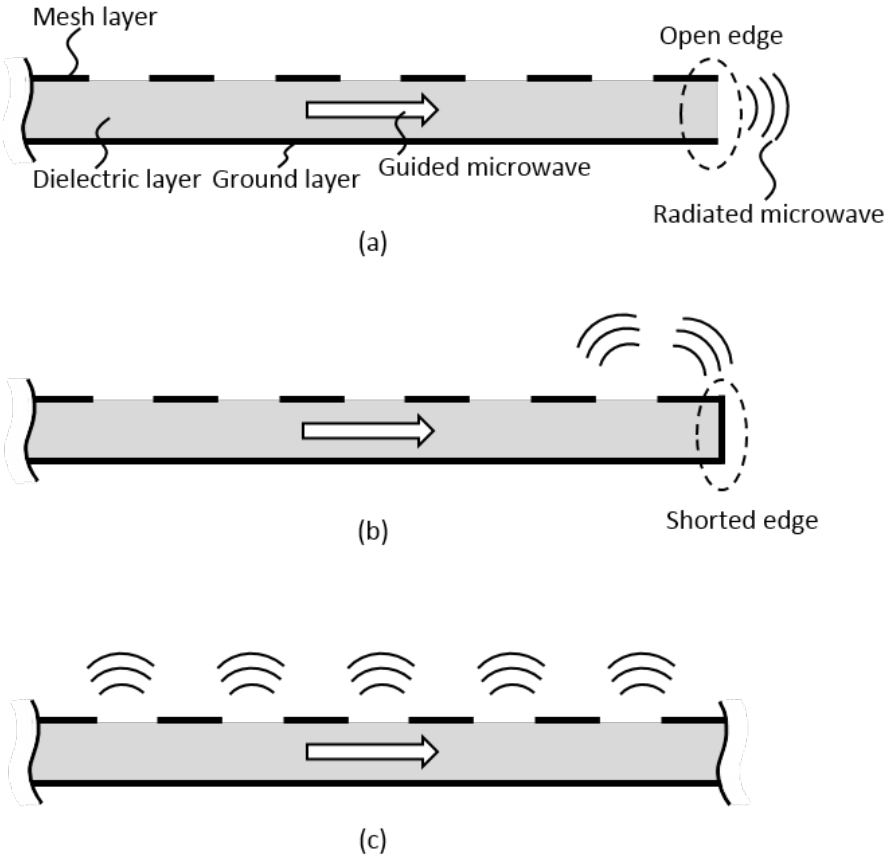

Fig. 4.9. Three variations of radiation from the 2DC sheet. (a). Radiation from the sheet gap. (b). Radiation due to an impedance discontinuity by the shorted sheet edge. (c). Radiation from a part of a periodic mesh.

$$q = \epsilon_0 \boldsymbol{n} \cdot \boldsymbol{E} = \epsilon_0 E_z \tag{4.5}$$

where n denotes a unit vector normal to the sheet surface. Note that the thickness of the sheet h is neglected because a distance between an observation point and the sheet is much larger than the sheet thickness.

$\boldsymbol{M}$, $\boldsymbol{J}$, and q are distributed on all over the ground plane and the ground plane is equivalent to their image components at the opposite side toward the ground layer as shown in Fig. 4.10(b). Since $\boldsymbol{J}$ and q are cancelled with their image components, they have no contribution for the far-field radiation. Only the doubled magnetic field density, thus, contributes to the radiation as shown in Fig. 4.10(c).

Since the sheet length is finite, the magnetic field at the far-field is generated by a line source of the surface magnetic current whose length is L as shown and is generally calculated by electric vector potential $\boldsymbol{F}$ as follows.

$$\boldsymbol{H} = -\frac{j}{\omega\mu\epsilon}\nabla(\nabla \cdot \boldsymbol{F}) - j\omega\boldsymbol{F} \tag{4.6}$$

$\nabla \cdot \boldsymbol{F} = (0, \partial F_y/\partial y, 0)$ and $\partial F_y/\partial y = 0$ under the 2-D model. Thus, Eq. (4.6) becomes

$$\boldsymbol{H} = -j\omega\boldsymbol{F} \tag{4.7}$$

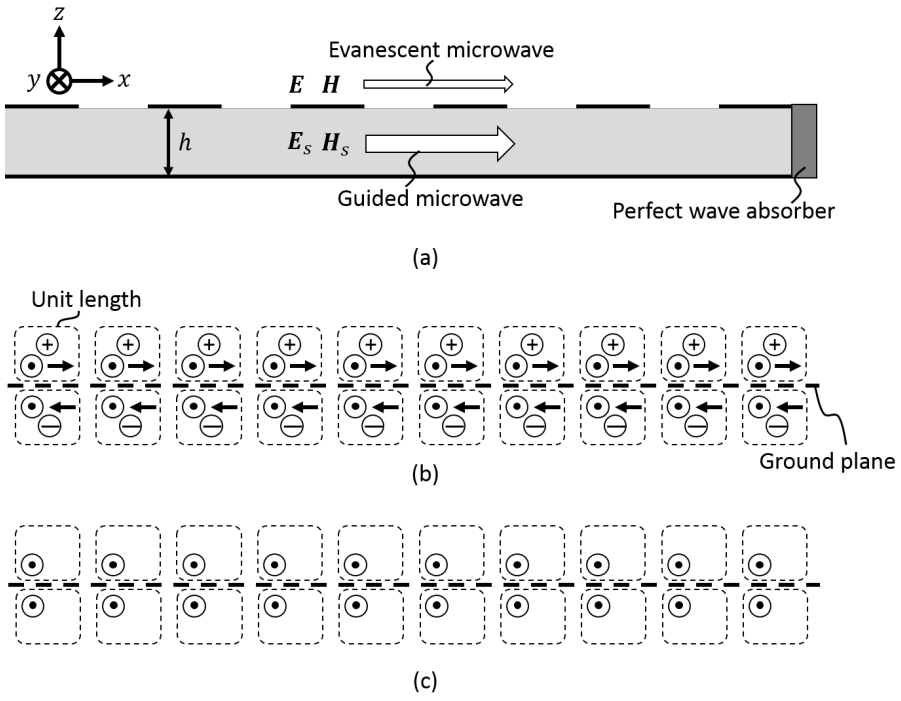

Fig. 4.10. Analytical model. (a). EM field in the vicinity of the sheet. (b). Distribution of surface electric currents, surface magnetic currents, and charges on the ground. The ground plane corresponds to the image component of each field at the opposite side of the ground plane. (c). Component contributing to generate the radiation at the far-field. That is the surface magnetic current.

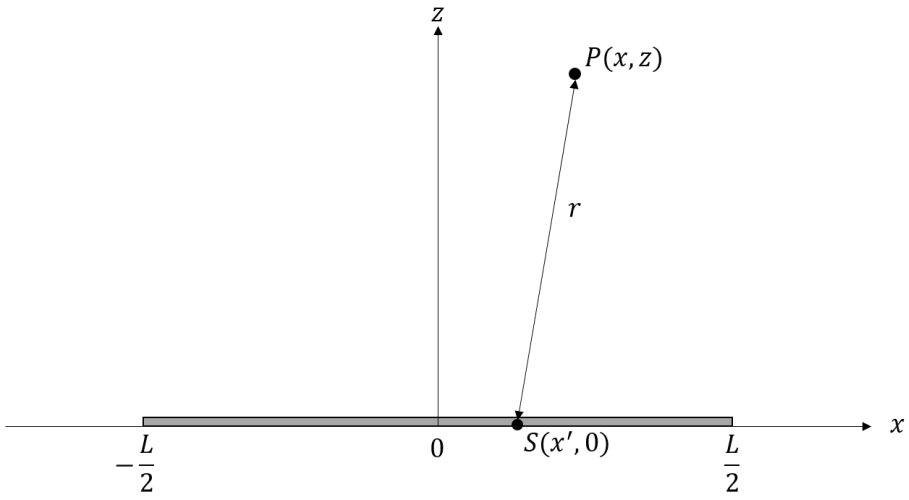

Fig. 4.11. Coordination System for the analytical model.

Based on a coordination system shown in Fig. 4.11(c), the electric vector potential with the line source is described with a Green's function as below.

$$\boldsymbol{F} = 2\int_{-\frac{L}{2}}^{\frac{L}{2}} G(x|x') \cdot \boldsymbol{M} dx'. \tag{4.8}$$

Although Eq. (4.8) is for the line source, the EM field is invariant in y-direction and is distributed in the two-dimensional plane. Hence, Green's function for two-dimensional radiation shown below [68] is applicable to Eq. (4.8).

$$G(r) = -\frac{j\epsilon_0}{4} H_0^{(2)}(k_0 r), \tag{4.9}$$

where k_0 and r denote an wavenumber in free space that is expressed as $2\pi/\lambda_0$ and a distance between the observation point and the source point. When the observation point is distant from the source, Eq. (4.9) is represented with the asymptotic expression of the Hankel function as below.

$$G(k_0 r) \simeq -\frac{j\epsilon_0}{4}\sqrt{\frac{j2}{\pi k_0 r}}\mathrm{e}^{-jk_0 r} = -\frac{\epsilon_0}{\sqrt{j8\pi k_0 r}}.\mathrm{e}^{-jk_0 r} \tag{4.10}$$

By substituting Eq. (4.10) to Eq. (4.8), we obtain

$$\boldsymbol{F} = -\frac{\omega\epsilon_0}{\sqrt{j2\pi k_0}}\int_{-\frac{L}{2}}^{\frac{L}{2}} \boldsymbol{M}\frac{\mathrm{e}^{-jk_0 r}}{\sqrt{r}} dx'. \tag{4.11}$$

We finally obtain the magnetic field in y-direction by substituting Eq. (4.4) and Eq. (4.11) to Eq. (4.7) as below.

$$H_y = -\frac{\omega\epsilon_0}{\sqrt{j2\pi k_0}}\int_{-\frac{L}{2}}^{\frac{L}{2}} E_x(x')\frac{\mathrm{e}^{-jk_0 r}}{\sqrt{r}} dx'. \tag{4.12}$$

4.4 Formulation for suppression

In this section, the suppression method is presented on the basis of the radiation model. When the distance between an observation point and a source point on the sheet is much larger than the sheet size, the distance r is approximated as

$$r \sim r' - x'\cos\theta. \tag{4.13}$$

where r' and θ denote a distance between the observation point and the origin and an angle of the observation point toward the x-axis as shown in Fig. 4.12,

Thus, H_y becomes

$$H_y(\theta) = \frac{\omega e^{-jk_0 r}}{\sqrt{j2\pi k_0 r}}\int_{\frac{L}{2}}^{-\frac{L}{2}} E_x(x')e^{jk_0 x'\cos\theta} dx'. \tag{4.14}$$

Note that in Eq. (4.14), the distance between the observation point and the origin r' is constant and H_y is a function of θ. The evanescent field E_x of the guided-mode wave traveling in +x-direction with the wavenumber in the sheet k_s is expressed as

$$E_x(x') = A(x')e^{-jk_s x'}, \tag{4.15}$$

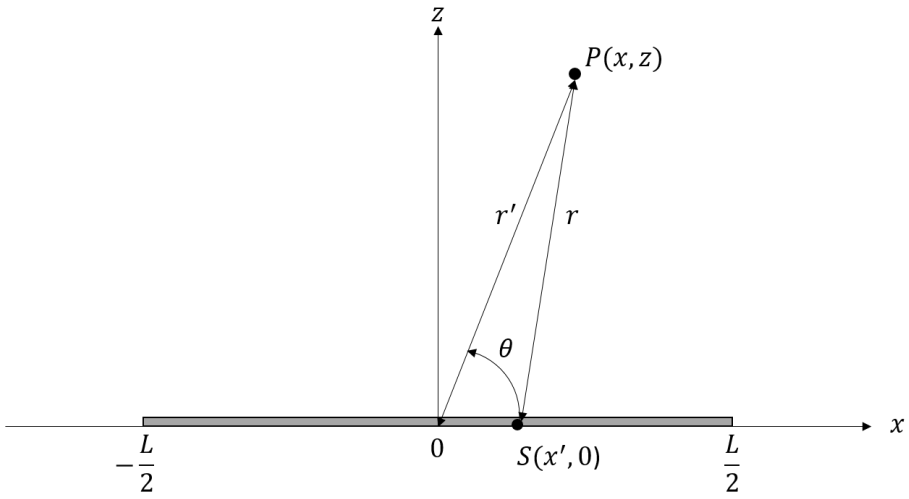

Fig. 4.12. Coodinate system for the suppression method.

where $A(x')$ represents an amplitude that is a function of the sheet position. $A(x')$ is constant when the sheet consists of only the periodic mesh. By substituting Eq. (4.15) to Eq. (4.14), we obtain

$$H_y = \frac{\omega e^{-jk_0 r}}{\sqrt{j2\pi k_0 r}} \int_{-\frac{L}{2}}^{\frac{L}{2}} A(x') e^{-j(k_s - k_0 \cos\theta)x'} dx'. \tag{4.16}$$

In Eq. (4.16), $A(x')$ can be interpreted as an window function that is zero except the range from $-L/2$ to $L/2$. When $A(x')$ is replaced with the window function $w(x')$, Eq. (4.16) becomes

$$H_y = \frac{\omega e^{-jk_0 r}}{\sqrt{j2\pi k_0 r}} \int_{-\infty}^{\infty} w(x') e^{-jkx'} dx', \tag{4.17}$$

where

$$k = k_s - k_0 \cos\theta. \tag{4.18}$$

Since the range of θ is from 0 to π, the corresponding range of k is

$$k_s - k_0 \leq k \leq k_s + k_0. \tag{4.19}$$

Eq. (4.17) is a Fourier transformation form regarding as $w(x')$. When $W(k) = \mathcal{F}[w(x')]$, Eq. (4.17) becomes

$$H_y = \frac{\omega e^{-jk_0 r} A}{\sqrt{j2\pi k_0 r}} W(k). \tag{4.20}$$

Eq. (4.20) indicates that the magnetic field above the sheet is calculated as an intensity of the window function $w(x')$ in wavenumber domain within an observable range that corresponds to the range of Eq. (4.19) as shown in Fig. 4.13.

Fig. 4.14 shows a Fourier transform result of the rectangular window that indicates the 2DC sheet consists of only the periodic mesh and a calculation result of Eq. (4.14) with Matlab. In Fig. 4.14, the horizontal axis is the angle θ that is transformed from wavenumber k based on Eq. (4.18). A signal frequency is 8 GHz and a radius from the sheet center is 4000 mm. The wavenumber in the sheet k_s is 261 (1/m). This value is calculated based on an EM simulation.

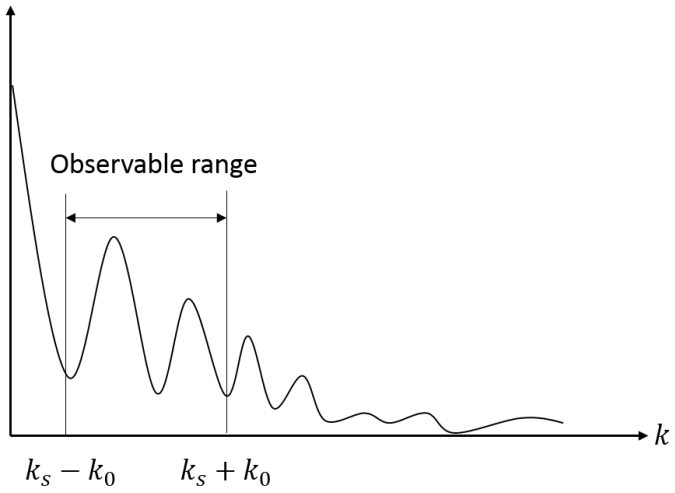

Fig. 4.13. Observable range of window function in wavenumber domain. Minimizing the intensity of this range leads to suppress the radiation.

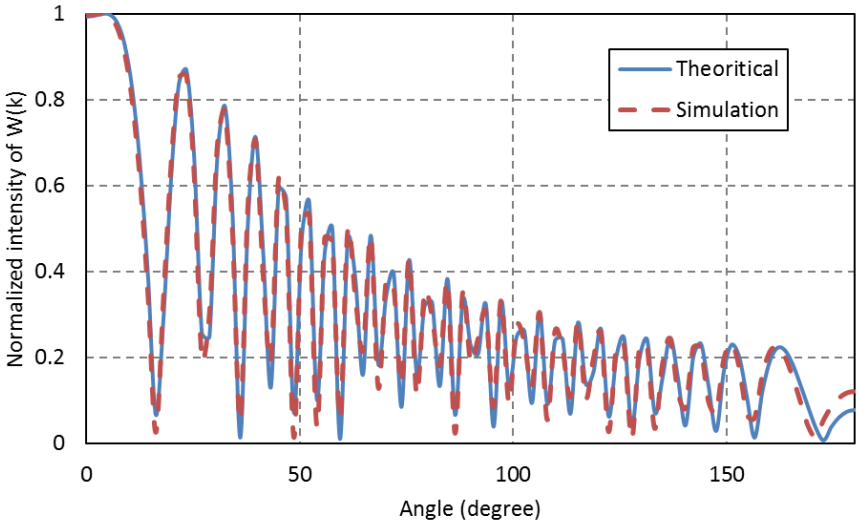

Fig. 4.14. Comparison between the Fourier transform of rectangular window and the calculation result of Hy with the radiation model. The intensity is normalized. The both result is almost matched along the range.

The approximation of Eq. (4.13) is reasonable because both the results are well matched. Therefore, controlling electric-field amplitude distribution whose intensity over the range shown in Eq. (4.19) in wavenumber domain is smaller leads suppression of the radiation from the sheet.

4.5 Suppression effect

4.5.1 Restriction of distribution pattern

The former section indicates that distributions of the electric-field amplitude whose spectrum is lower over the specific range can yield the low-emission from the sheet. Smooth

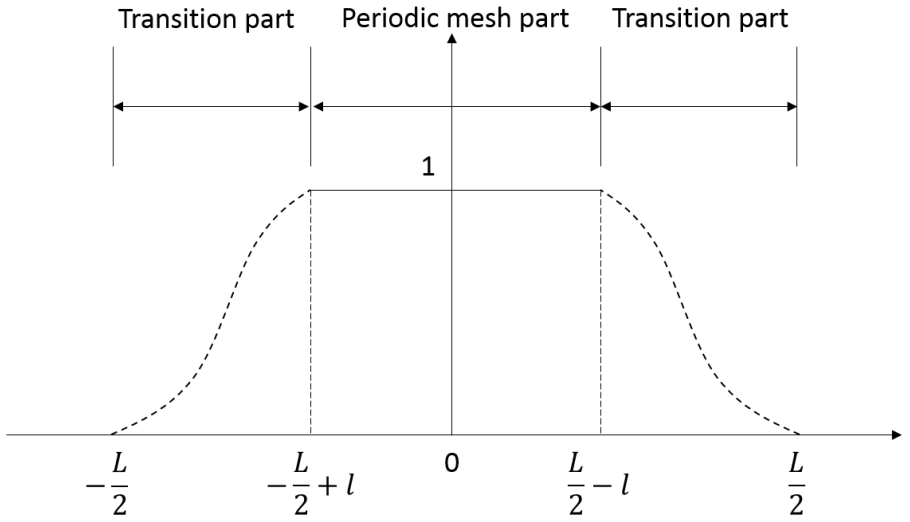

Fig. 4.15. Restriction of the amplitude distribution of the electric-evanescent field. The distribution is divided into three parts. The values of the two transition parts are controlled and periodic mesh part takes constant value. The distribution value is always positive.

transition at the ends of the sheet can enable such a spectrum according to knowledge of window functions in the signal-processing field.

Unlike the signal-processing field, the transition design of the sheet has the following restrictions: the value of distribution always takes a positive value; the constant part that corresponds to the periodic mesh part is necessary to couple the coupler and the sheet. The distribution pattern thus is divided into three section: the two transition sections and the constant-value section. These restrictions are described in Fig. 4.15.

In the following subsections, two types of patters are examined as a typical window patterns.

4.5.2 Straight transition

The straight transition is easy to make and useful when it has acceptable suppression effect. The distribution with the straight transition $w_s(x)$ is expressed as follow.

$$w_s(x) = \begin{cases} \frac{1}{l}(x+\frac{L}{2}) & -\frac{L}{2} \le x < -\frac{L}{2}+l \\ 1 & -\frac{L}{2}+l \le x \le \frac{L}{2}-l \\ -\frac{1}{l}(x-\frac{L}{2}) & \frac{L}{2}-l < x \le \frac{L}{2} \end{cases} \tag{4.21}$$

where L and l denote the sheet length and the transition length. Then the Fourier transform of $w_s(x)$ becomes

$$W_{\mathrm{s}}(k) = \frac{2}{k^2 l}(\cos k(\frac{L}{2}-l) - \cos k\frac{L}{2}). \tag{4.22}$$

Eq. (4.22) indicates that the intensity of $W_s(k)$ decreases in proportion to $1/k^2$ while $1/k$ with the rectangular window. Therefore, suppression effect is expected with the straight transition. Fig. 4.16 shows the intensity of $W_s(k)$ with the following settings: the sheet length is 0.5 m and the transition length is 0.1 m; the frequency is 8 GHz.

Compared to the rectangular window, the intensity is low over the angle θ and decreases more rapidly.

Fig. 4.17 shows radiated power regarding the length of the transition length with $L = 0.5$ m. When transition length is 0.25 m, there is no periodic mesh part. Suppression effect becomes larger as the transition length is longer and frequency is higher. This is because electric length becomes longer with higher frequency when a physical length is unchanged.

4.5.3 Cosine curve transition

Cosine curve windows that smoothly connect two points for example like Blackman-Nuttall window and Blackman-Harris window [69] yields low side-lobe level. Therefore,

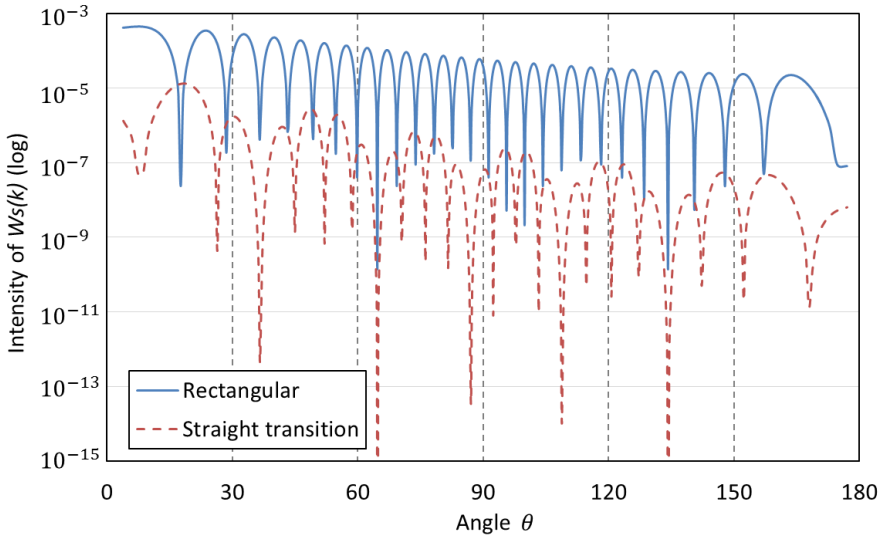

Fig. 4.16. Intensity of the Fourier transform of the distribution with the straight transition.

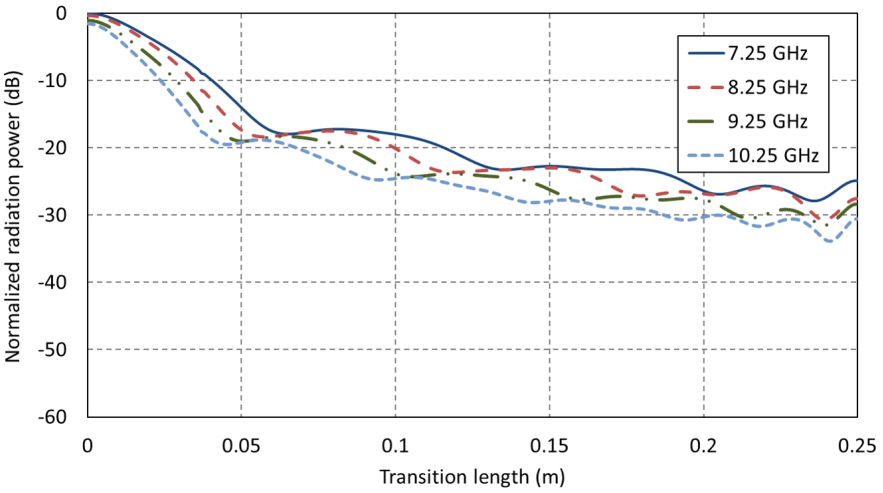

Fig. 4.17. Radiation power normalized by that of the rectangular window. Suppression effect becomes larger as the transition length is longer.

this type of window is also considered to be effective in the 2DC sheet design. Smooth transition with cosine curve is generally described as below.

$$w(x) = \sum_{n=0}^{N} a_n \cos(2\pi \frac{b}{x}), \tag{4.23}$$

where b is the length of the window. Based on Eq. (4.23) , we can describe the distribution pattern as follows.

$$w(x) = \begin{cases} \sum_{n=0}^{N} a_n \cos(\pi \frac{(x+\frac{L}{2})}{l}) & -\frac{L}{2} \leq x < -\frac{L}{2} + l \\ 1 & -\frac{L}{2} + l \leq x \leq \frac{L}{2} - l \\ \sum_{n=0}^{N} a_n \cos(\pi \frac{(x-\frac{L}{2})}{l}) & \frac{L}{2} - l < x \leq \frac{L}{2} \end{cases} \tag{4.24}$$

Note that $\sum(-1)^n a_n = 1$ and $w(x) \geq 0$ because the amplitude of electromagnetic field cannot take negative value. Then Fourier transform result $W(k)$ becomes

$$W(k) = \frac{2}{k} \sin k(\frac{L}{2} - l) + \frac{2}{k} \sum_{n=0}^{N} \frac{k^2 l^2 a_n}{k^2 l^2 - n^2 \pi^2} (\sin k\frac{L}{2} - \cos n\pi \sin k(\frac{L}{2} - l)) \tag{4.25}$$

$$= \frac{2}{k} \prod_{n=1}^{N} \frac{1}{(k^2 l^2 - n^2 \pi^2)} (\alpha(k) \sin k\frac{L}{2} + \beta(k) \sin k(\frac{L}{2} - l)). \tag{4.26}$$

Eq. (4.26) indicates that $W(k)$ consists of two terms. Both the factors except $\sin k\frac{L}{2}$ and $\sin k(\frac{L}{2} - l)$ should be minimized to decrease the intensity of $W(k)$.

As preliminary considerations, the upper limit of suppression is examined with $N = 1, 2$ in this thesis. These orders are commonly used in higher-order cosine windows, like Hanning-window and Blackman window [69].

When $N = 1$, each factor of $\sin k\frac{L}{2}$ and $\sin k(\frac{L}{2} - l)$ is described as below.

$$\alpha(k) = (a_0 + a_1)k^2 l^2 - \pi^2 a_0. \tag{4.27}$$

$$\beta(k) = -\pi^2(1 - a_0). \tag{4.28}$$

Constraint conditions restrict a value of a_0 to more than 0.5. Fig. 4.18(a) shows the intensity of $W(k)$ by changing the value of a_0 from 0.5 to 1. Parameter settings are as follows: The sheet length $L = 0.5$m; l=0.1m; the frequency is 8 GHz. When $a_0 = 0.5$, the radiated power is lowest. This is because the factor of $\alpha(k)$, $a_0 + a_1$, becomes zero and the intensity decreases in proportion to $1/k^3$. In the case of other values, that factor is not zero and the intensity decreases in proportion to $1/k$ whose value is the same as that of the rectangular window. Therefore, when $N = 1$, $a_0 = 0.5$ and $a_1 = -0.5$ is the most effective coefficient set. In this case the window function is the same as Tukey taper [69]. Fig. 4.18(b) indicates the normalized radiated power. As an overall trend, longer transition length and higher frequency signal yield higher suppression effect.

When $N = 2$, each factor is described as below.

$$\alpha(k) = (a_0 + a_1 + a_2)k^4 l^4 + (-5\pi^2 a_0 - 4\pi^2 a_1 - \pi^2 a_2)k^2 l^2 + 4\pi^4 a_0 \tag{4.29}$$

$$\beta(k) = (-5\pi^2(1 - a_0) - 4\pi^2 a_1 + \pi^2 a_2)k^2 l^2 + 4\pi^4(1 - a_0) \tag{4.30}$$

When the factor of $k^4 l^4$ in $\alpha(k)$, $a_0 + a_1 + a_2$, is zero, $a_1 = 0.5$ and $a_0 + a_2 = 0.5$. That indicates that the intensity of $W(k)$ decreases in proportion to $1/k^3$. Since both the

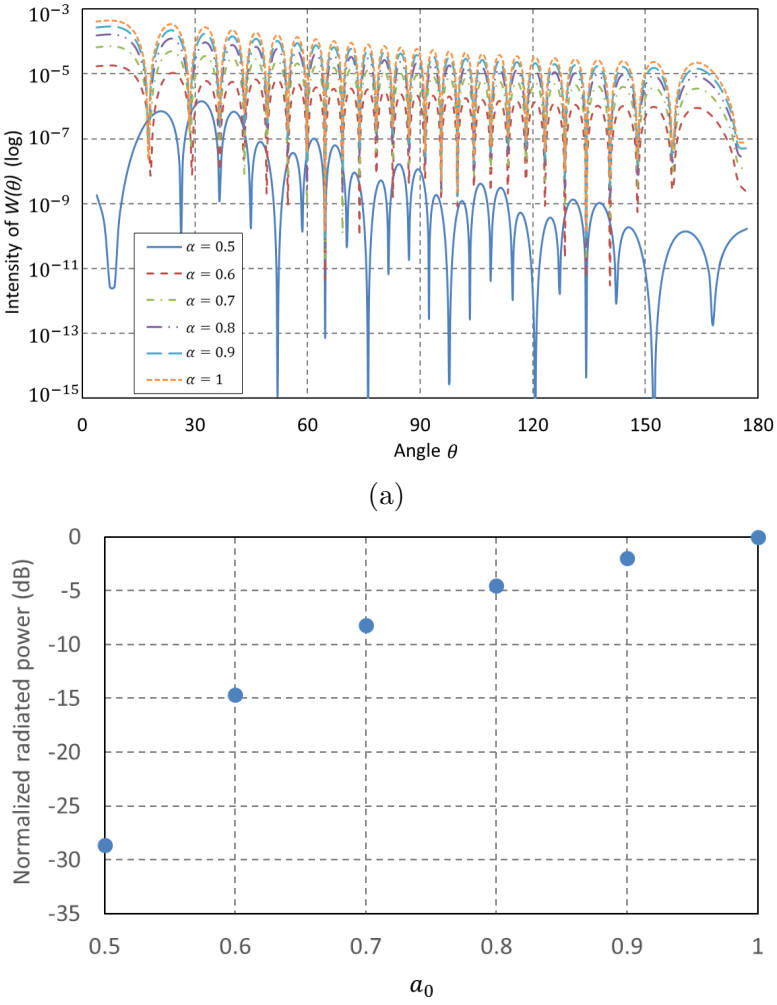

Fig. 4.18. Property of cosine curve transition with $N = 1$. (a). Intensity of $W(k)$. (b) Normalized radiated power with change of a value of a_0. When $a_0 = 0.5$, radiated power becomes lowest.

factors of k^2l^2 in $\alpha(k)$ and $\beta(k)$ does not become zero simultaneously, decrease rate $1/k^5$ is impossible.

Fig. 4.19 shows the intensity of $W(k)$ by changing the value of a_0 from 0.375 to 0.625. When $a_0 = 0.375$ or 0.625, the factor of k^2l^2 in $\alpha(k)$ and $\beta(k)$ is zero, respectively. Although there are no noticeable differences among plots, radiated power becomes lowest when $a_0 = 0.5$. This result is the same as $N = 1$. Therefore, Tukey window pattern is the most effective window in the case of $N = 1$ or 2.

Fig. 4.20 shows the intensity of Tukey window pattern with the change of the length of the transition section. As the straight transition, higher suppression effect is obtained when the transition length is longer and signals frequency is higher.

Compared to the straight transition, cosine transition has more suppression effect when the transition length is longer than a certain value, for example 0.05 m with 10.25 GHz signals as shown in Fig. 4.21. This is because the intensity of the distribution with cosine transition decreases in proportion to $1/k^3$ whereas $1/k^2$ in the case of the straight

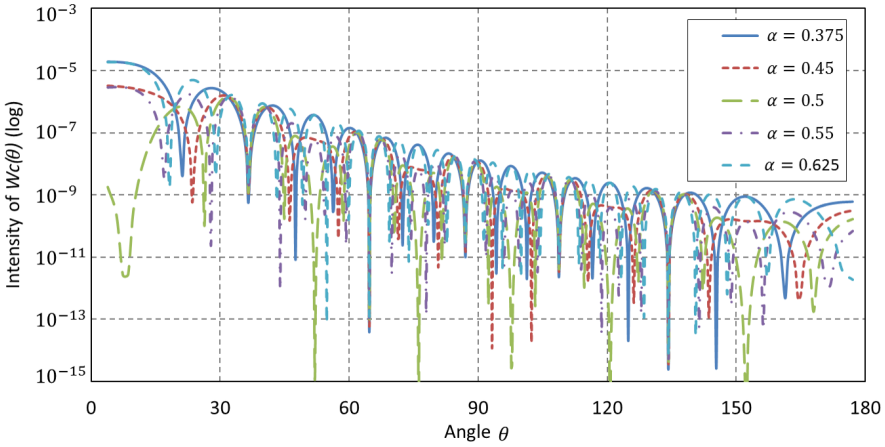

(a)

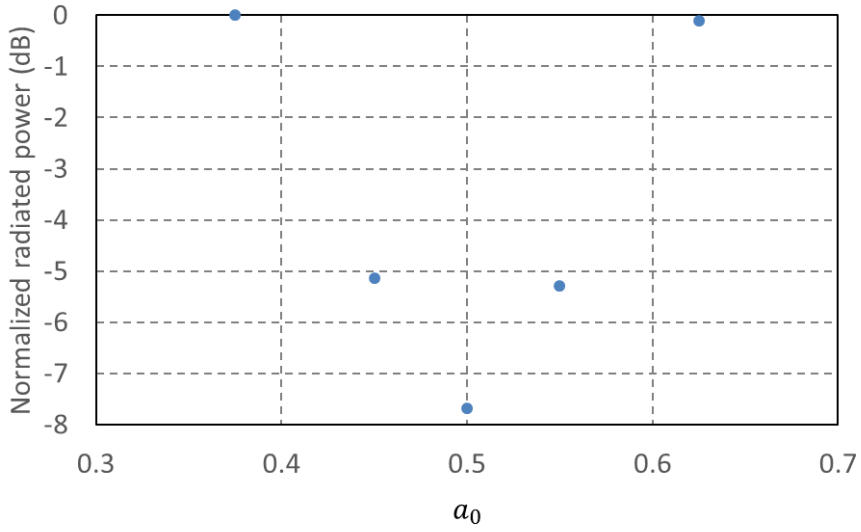

(b)

Fig. 4.19. Property of cosine curve transition with $N = 2$. (a). Intensity of $W(k)$. (b) Normalized radiated power with change of a value of a_0. When $a_0 = 0.5$, radiated power becomes lowest.

transition. Thus straight transition has more suppression effect when the length is short.

4.6 Possibility of complete suppression

As mentioned in 4.4, decreasing the intensity of the x-axis electric-field distribution in wavenumber domain over the observable range leads the suppression of the radiation from the sheet and the effect of the taper is ensured in the former section. The radiation, however, is still remained. In this section, the possibility of complete suppression is discussed.

The radiation is completely suppressed when $W(k) = 0$ in the observable range, from $k_s - k_0$ to $k_s + k_0$. Two kinds of spectrums that achieve such an condition are considered: a low-pass filter shape and a band-stop filter shape. The low-pass filter shape becomes a sinc function in space domain, which has an infinite impulse response. A part of the

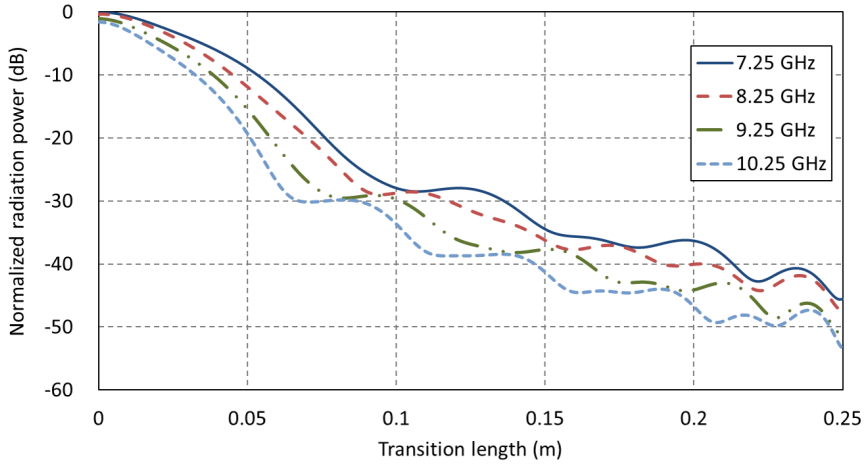

Fig. 4.20. Radiation power normalized by that of the rectangular window. Suppression effect becomes larger as the transition length is longer.

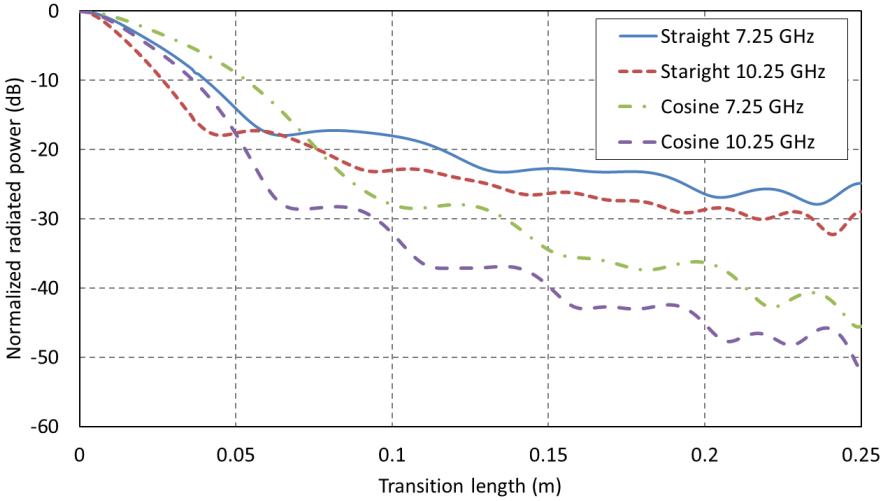

Fig. 4.21. Comparison of suppression effect between the straight transition and the cosine transition. The straight transition has more suppression effect when the transition length is short.

sinc function longer than the sheet is truncated due to the finite sheet length and this process is equivalent to applying the rectangular function to the sinc function. Therefore, $W(k)$ has values except zero over the observable range although the amount of emission considerably decreases.

In the case of the band-stop filter shape, the band-pass filter can be interpreted as a product of an arbitrary spectrum and the band-stop filter as shown in Fig. 4.22, that is, $W(k) = W_1(k) \times W_2(k)$, thus $w(t)$. This relation corresponds to the convolution in space domain as described below.

$$w(x') = w_1(x') * w_2(x') \tag{4.31}$$

$w_2(x')$ continues infinite length response, thus the complete suppression is also difficult even with the band-stop filter shape.

Therefore, complete suppression is difficult although almost complete suppression can

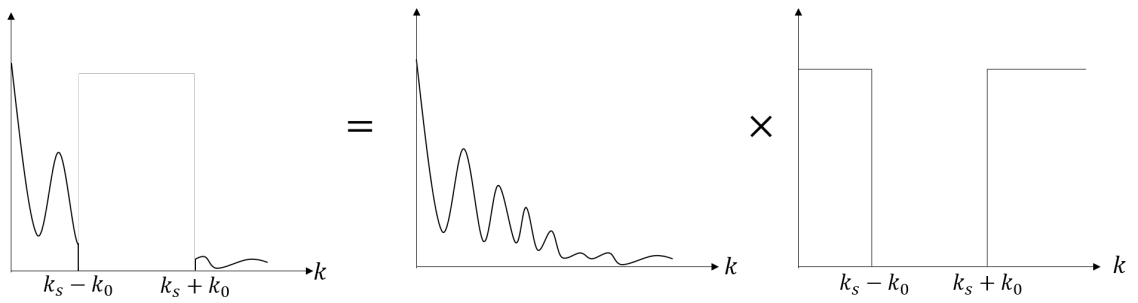

Fig. 4.22. k domain structure.

be achievable.

4.7 Experiment

In this section, prototype sheets that changing the amplitude-distribution are prototyped and evaluated to verify the proposed method. First, designs of the prototyped sheets and the performance estimation are described. Then, the suppression effect is evaluated and compared with the model and the simulation.

4.7.1 Sheet design

The former section clarified that the distribution of the electric-evanescent field amplitude is involved in the suppression of the radiation. In order to achieve a required distribution with an actual 2DC sheet, the relation between the distribution and the sheet structure is necessary. That relation is difficult to directly obtain, however, is acquired by using a sheet impedance σ [22], that is the electric property of the inductive layer of the 2DC sheet. This is because the evanescent field is determined by the sheet impedance and the sheet impedance is also changed by a sheet structure.

The sheet impedance is defined as below.

$$\sigma \equiv R + jX \equiv \frac{E_x}{I_x}, \tag{4.32}$$

where R and X denote a resistance component and a reactance one of a 2DC sheet whereas E_x and I_x are an electric-evanescent field and a current density in the x-direction, which is the direction where signals propagate. In the case of a good conductor, a resistance component R is nearly equal to zero. The sheet reactance X is changed by a mesh structure of the sheet. Therefore the relation between the mesh structure and the sheet reactance is necessary to design the low-emission sheet.

The sheet reactance X is calculated with the following equation [66].

$$X = \mu_0 h\omega(\frac{1}{\epsilon_r}\frac{{c_0}^2}{c^2} - 1), \tag{4.33}$$

where μ_0 and c_0 denote the magnetic permeability and the light-velocity in space whereas c is the light-speed in the sheet. h and ϵ_r also represent a thickness and a relative permittivity of the dielectric layer. c is calculated with a wavelength in the sheet λ that is numerically obtained by an EM simulation. The following simulations are conducted to obtain λ with a change of the mesh structure. Then the relation between the sheet impedance and the mesh structure is calculated.

Fig. 4.23 shows the simulation model. The model is one-period sheet model. The mesh pitch and width parallel to the y-axis is 4 mm and 1mm. A thickness and a relative permittivity of the dielectric layer is 1 mm and 2.1. An aperture width w of the mesh along the x-axis is changed from 0 mm to 1.5 mm. In other words, the width of the mesh line parallel to the x-direction is changed from 1 mm to 4 mm. When the aperture width w is 0 mm, the model is equivalent to a parallel plated waveguide. A signal source is set at the boundary of model in the x-direction and a perfect wave absorber is set at the opposite side.

Fig. 4.24 shows the simulation results. The sheet impedance X plotted in the vertical line is calculated with Eq. (4.33). In addition to the simulation results, higher-order functions are also plotted. The forth order function fits the results the best. Therefore, we approximately obtain the relation between the sheet impedance and the mesh structure as below.

$$X \approx 1.85w^4. \tag{4.34}$$

The relation between the sheet structure and the distribution of the electric-evanescent field is acquired based on Eq. (4.34) and the relation between the sheet impedance and

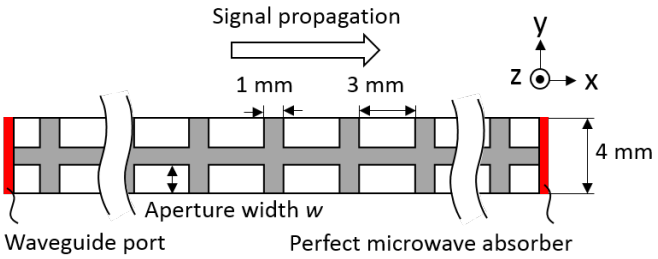

Fig. 4.23. Top view of the model One-period structure is modeled and aperture width w is changed from 0 mm to 1.5 mm. When $w = 0$ mm, the model is equal to a parallel plate waveguide. The signal source is set at the boundary of the model and a perfect microwave absorber is set at the opposite side. Therefore, no reflection happens.

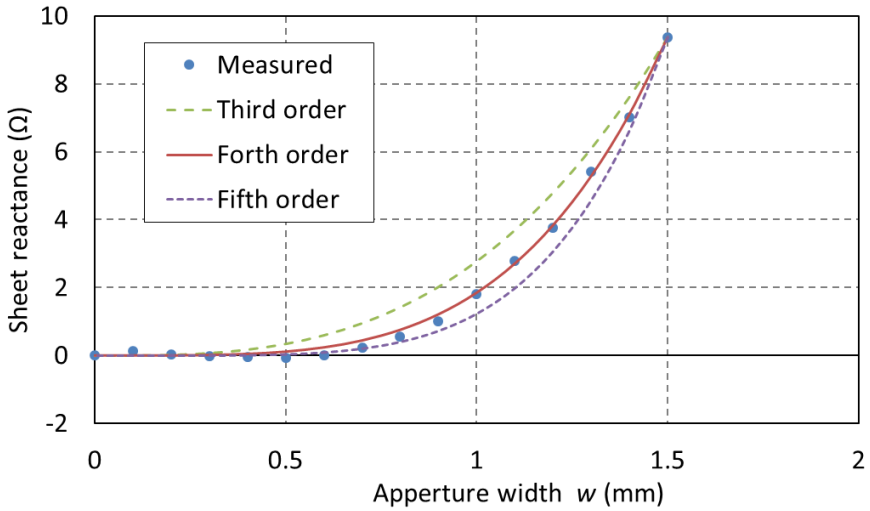

Fig. 4.24. Simulation result. A trend with a change of aperture width of the sheet fits the forth order function.

the evanescent electric-field [70] and enables the sheet design that achieves the evanescent electric-field distribution for low-emission. In this paper, the Tukey-window-shape distribution is examined. The simulation model with Tukey window shape taper is shown in Fig. 4.25.

Fig. 4.26 shows the evanescent electric-field distribution, which is calculated with the EM simulation data just above the sheet. Each plot is the averaged value over the mesh pitch, 4 mm as shown in Fig. 4.27 because the electric property of the 2DC sheet is equivalent to average property by the mesh pitch from the macroscopic viewpoint when a wavelength of signals in the sheet is longer than the mesh pitch. The simulation result roughly fits the theoretical line of Tukey-window-shape. The sheet design based on Eq. (4.34), thus achieves control of the evanescent electric-field distribution.

Based on these considerations, the design of the prototype sheet is determined as shown in Fig. 4.28: the sheet length is 500mm; a mesh pitch and a line width is 4 mm and 1 mm, respectively; the area 10.5 mm from the sheet edges are metal part, which is used as an area to attach a copper tape for boundary shorting; the area 100 mm from the metal part

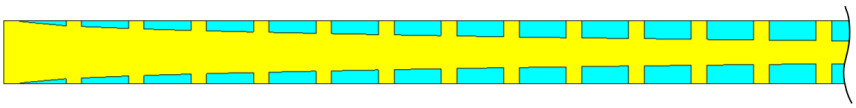

Fig. 4.25. Simulation model with Tukey window shape taper.

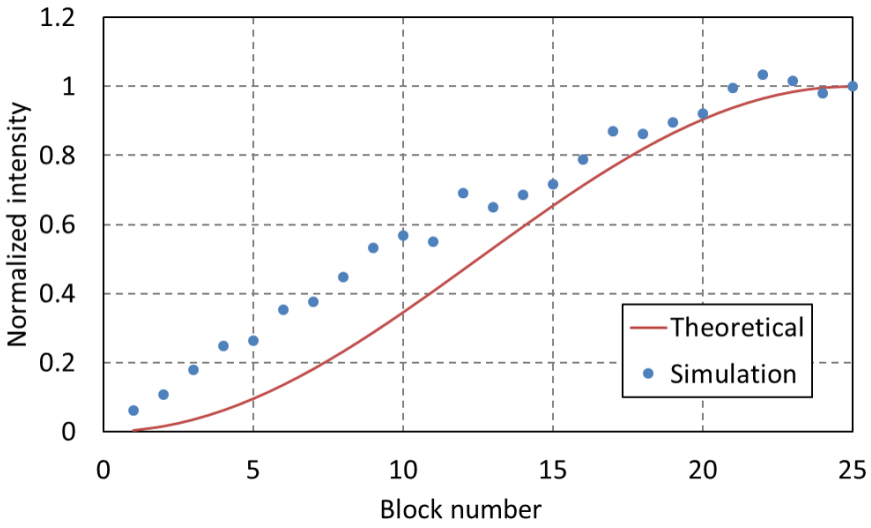

Fig. 4.26. Average electric-evanescent field of the Tukey-window-shape mesh strucutre.

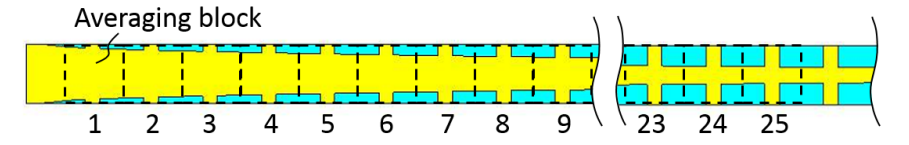

Fig. 4.27. Averaged block used in Fig. 4.26. From the macroscopic viewpoint, the 2DC sheet shows the average property by the mesh pitch when a wavelength in the sheet is longer than the mesh pitch.

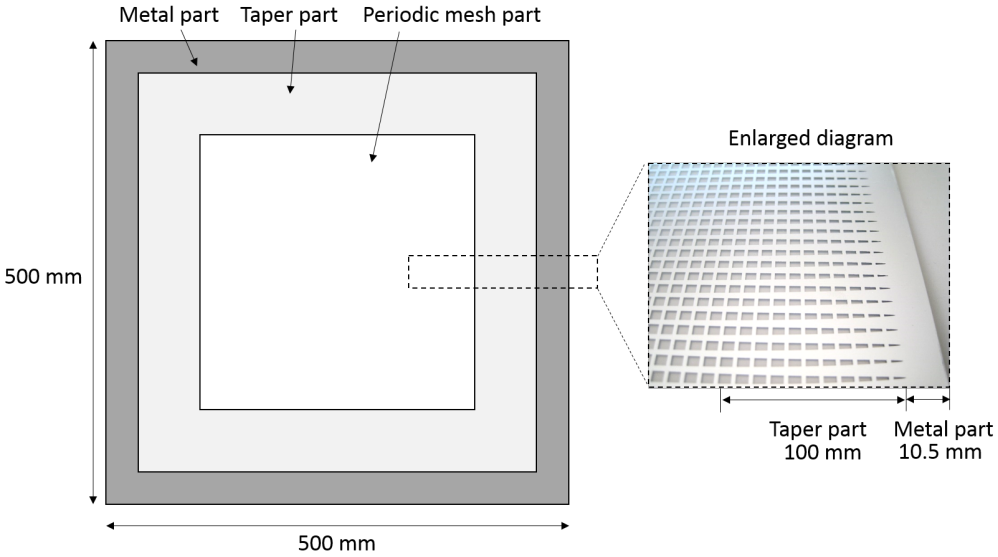

Fig. 4.28. Prototype sheet design. The added structure at the sheet edge achieves the Tukey-window-shape electric evanescent field. The enlarged diagram is the picture of the prototype sheet.

is a taper part. Tukey-window-shape, that has sufficient suppression effect with 100-mm length are implemented at the sheet edge.

EM simulations are condcuted to evaluate the performance of the proposed method with three type sheet: an open-edge sheet, a short-edge sheet, and a prototype sheet with the Tukey-window-shape taper. The common specification is as follows: the sheet size is 500 mm × 500 mm; the material of the two conductive layers and the dielectric layer is aluminum and polypropylene; the thickness of the dielectric layer is 1 1mm. The taper length is set as 100 mm. Fig. 4.29 indicates the simulation results regarding the radiation efficiency, which shows the ratio of radiated energy to input energy, and maximum antenna gain. The prototype sheet achieves the lowest value in both the indexes over almost all

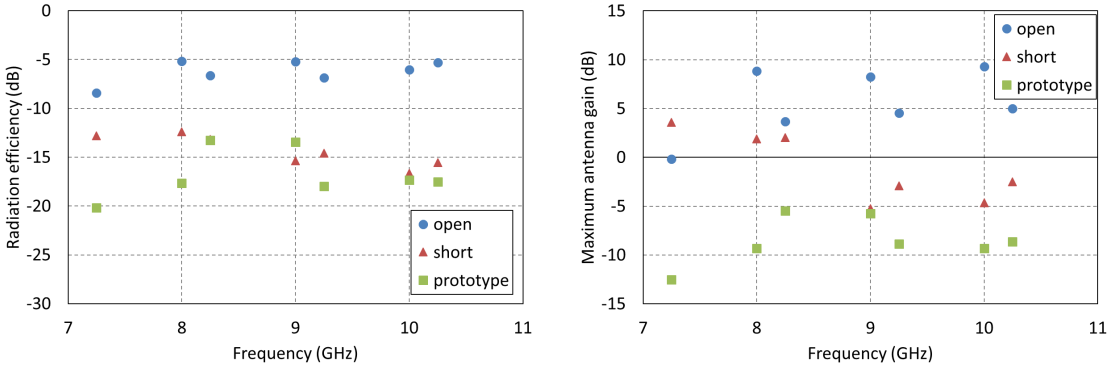

(a) (b)

Fig. 4.29. Performance comparison of 3D sheet models with EM simulations. (a). Radiation efficiency, which indicates the ratio of radiated energy to input energy. (b). Maximum antenna gain. Both the results show that the prototype sheet reduces the radiation from the sheet over almost all the UWB band.

the UWB bandwidth. This fact indicates that the proposed method is effective to reduce the radiation from the sheet.

4.7.2 Measurement method

The schematic diagram of the measurement setup is described in Fig. 5.6. The radiated power is measured in an anechoic chamber with a wideband antenna that is placed at 3 m away from the sheet. The sheet is set on a turntable and rotated by one degree regarding an elevation angle θ. An azimuth angle ϕ is set at 0 degree. The feeding to the sheet is conducted with the coupler set under the sheet like the former section.

4.7.3 Measurement result

Fig. 4.31 shows the antenna gain at four frequencies, 7.25 GHz, 8.25 GHz, 9.25 GHz, and 10. 25GHz. Compared to the simulation result of the same structure model, the antenna gain of the prototype sheet is similar to that of the simulation. The desired performance is considered to be achieved by the prototype sheet.

Fig. 4.32 shows the comparison of the antenna gain between the prototype sheet and the shorted sheet without the taper. Although the antenna gain of the prototype sheet is decreased more steeply than that of the shorted sheet at 7.25 GHz and 8.25 GHz, little difference between them is observed at 9.25 GHz and 10.25 GHz. The wavelength of both the two frequencies is comparable or smaller than the size of the feeding coupler set at the back of the sheet. This can influence the results.

From these experimental results, the usefulness of the proposed method is ensured.

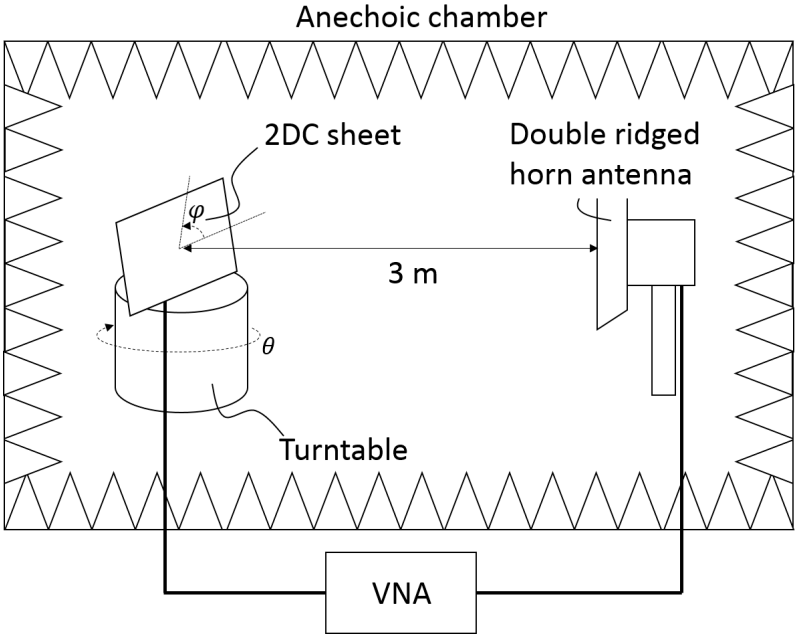

Fig. 4.30. Measurement setup. The prototype sheet and a receiver antenna is placed at the interval of 3 m in an anechoic chamber. The sheet put on a turntable is rotated by one degree. A short-edge sheet with no taper is also examined as a reference.

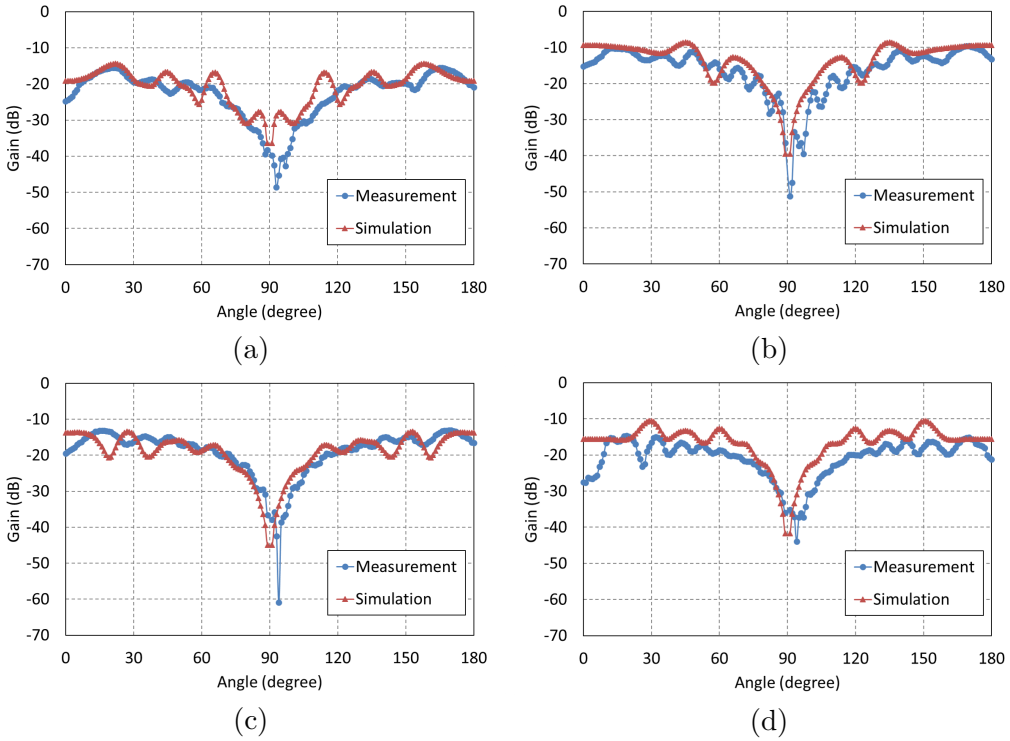

Fig. 4.31. Measurement results of the antenna gain of the prototype sheet along an elevation angle θ, 0-180 degree at an azimuth angle $\phi = 0$. (a). 7.25 GHz. (b). 8.25 GHz. (c). 9.25GHz. (d). 10.25 GHz. The measured antenna gains are similar to the simulation results of the prototype sheet model.

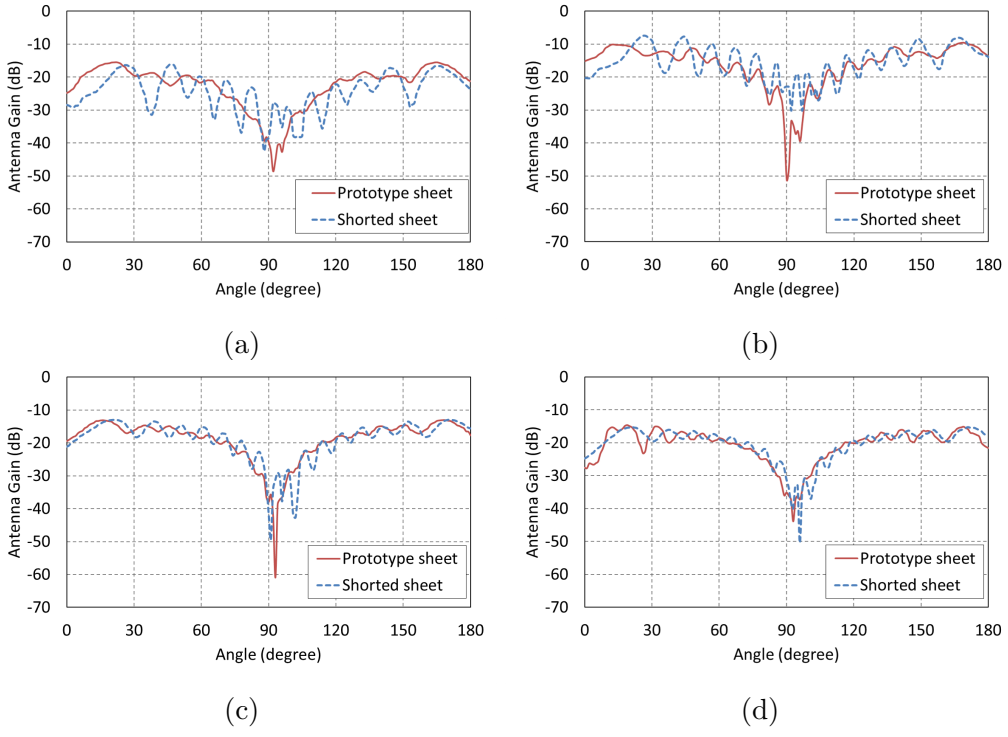

Fig. 4.32. Comparison of the antenna gain between the prototype sheet and the shorted sheet.

4.8 Conclusion

In this chapter, we proposed the suppression method of the radiation from the 2DC sheet. First, the radiation measurement showed that an antenna gain of the sheet with only a periodic mesh pattern is about −13 dB. This result shows that the 2DC sheet is immune against aerial radio signals, but receives them to a certain extent. Since multiple tiles are implemented in an actual tile system, the tile system becomes less immune.

To solve the radiation problem, we modeled the radiation mechanism from the 2DC sheet. The model indicates the electro-magnetic field is generated by the evanescent electric-field.

Then, the suppression method was presented. The proposed radiation model can be interpreted as a Fourier transform of the distribution of the evanescent electric-field along the direction where signals propagate on the basis of approximation that the observation point is distant from the source point. The magnetic field observed at a far-field is a part of the distribution in wavenumber domain. Therefore, decreasing the intensities over the range enables suppress of the radiation from the sheet. These model was well matched to EM simulation result. When the amplitude transition of 10 cm along cosine curved distribution at the sheet edge, the radiation is suppressed by 30 dB. Such a low emission sheet enables higher immune to aerial radio signals and reliable communication.

To verify suppression effect, we fabricated the prototype sheet that equipped with the Tukey-window-shape taper at the edge. The measurement results shows that the antenna gain becomes smaller than that of the shorted sheet without the taper. Therefore, the sheet with the proposed method enables the tile system to be more immune against radio signals in space.

Chapter 5

Positioning method with the tile system

5.1 Significance of indoor positioning

Recently moving devices like robots and smart phones have been increasing. Given that information related to the position of a device is offered, applications like navigation and route tracing are possible. In an outdoor environment, the global positioning system (GPS) has already offered the device position with sufficient accuracy, however, it generates large errors in an indoor environment because line-of-sight transmission between receivers and satellites are not ensured. In addition, signal propagation inside a room is more complex than in an outdoor environment due to multipath effects by objects like walls and furniture, and change of propagation characteristics by moving objects and people. Therefore, an indoor positioning system is strongly demanded and has attracted research interests in recent years.

5.2 Related works

At the present, many positioning methods are presented for example infrared, ultrasound, WLAN, Bluetooth, radio-frequency identification (RFID), and UWB [71]. Traditional principle of positioning is triangulation, with which the device calculates its position with information like time-of-flight(TOF) or received signal strength (RSS) from at least three devices whose position is known. In Wi-Fi fingerprint-based method [72], the device estimates its position by comparing the received signal to the received-signal database that is recorded beforehand at the same environment. RFID based method provides the position directly.

Positioning techniques are classified into three types with regard to the architecture. One is self-positioning architecture. In this system, the device connected to a system calculates its own position with receiving signals, for example, the fingerprint technique. Other is infrastructure positioning in which the infrastructure like APs detects the position of devices in their coverage. The other is self-oriented and infrastructure-assisted. In this architecture, device positioning is conducted only when the device send a request to the infrastructure.

Another classification perspective is whether an additional hardware is necessary or not. For example, no additional hardware is required in Wi-Fi-based positioning whereas necessary in positioning with ultrasound to both a device and an infrastrucuture. From the viewpoint of cost and implementation, the techniques that require no additional hardware are favorable.

There are many criterion to evaluate positioning techniques, for example, cost, accuracy, and robustness [71], especially, accuracy is important. Although positioning accuracy depends on an application, generally the meter-level accuracy is required in commercial

use [72]. Each system has advantages and disadvantages. The positioning system is designed depending on requirements of an application. In some cases, a single technology is employed and in other cases multiple technologies are combined. Although at least three access points (AP) are necessary for a triangulation technique and a fingerprint one with Wi-Fi signal, the positioning technique named Chronos [73], with which position detection with decimeter-level accuracy is achieved with a single AP, has been developed.

5.3 Strategy

The tile system consists of multiple tiles, in other words the system is separated into the same size units. The strategy in this thesis is to distinguish tiles where a device is placed on, that is, to assign an identification to each tile, named tile ID as shown in Fig. 5.1(a), and recognize the device position by relating an identification of the device, device ID, with a tile ID. The accuracy of this strategy is the inverse of square root of a tile length, for example, about 35 cm with 50-cm square tile. This value is better than that of Wi-Fi-based technique and is comparable to that of Chronos. Other advantage of this technique is that the effect of a room environment like objects is negligible because signals propagate in the tile system. That contributes to the robustness of positioning. In addition, the tile system achieves both positioning detection and high-speed communication. The restriction of this strategy is that position is detected discretely.

As mentioned in 5.2, there are the three architectures for position detection. The self-oriented and infrastructure-assisted architecture is considered as a kind of self-positioning one because position calculation is conducted by a device. The two architectures, self-positioning and infrastructure positioning, applied to the tile system are shown in Fig. 5.2. A circuit for positioning (CP) is added to the base layer in both cases. This reason is in the following. Since signals are amplified to keep intensity, the AP is unable to distinguish the tile position only with RSS. Therefore, the additional circuit is necessary in the base layer to add the difference to the tiles.

In the self-positioning as shown in Fig. 5.2 (a), the CP transmits its tile ID to the 2DC sheet then the device on the tile receives signals and obtain their position. Although this architecture is simple, the CP is required to always transmit signals even if no devices are put on the tile. The device on the tile is also necessary to be equipped with the specialized protocol to interpret the ID signal. In the case of the infrastructure positioning as shown

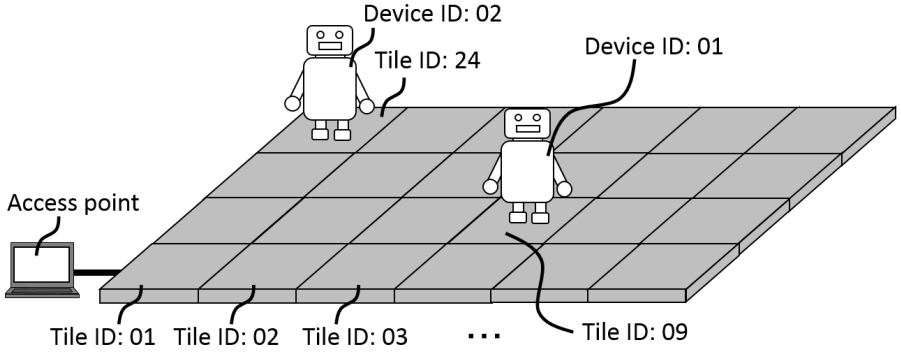

Fig. 5.1. Concept of position detection with the tile system. Since the tile system is separated into multiple tiles, device position can be detected by assigning an identification to each tile (Tile ID) and relating the ID of the device with tile ID where the device is placed on.

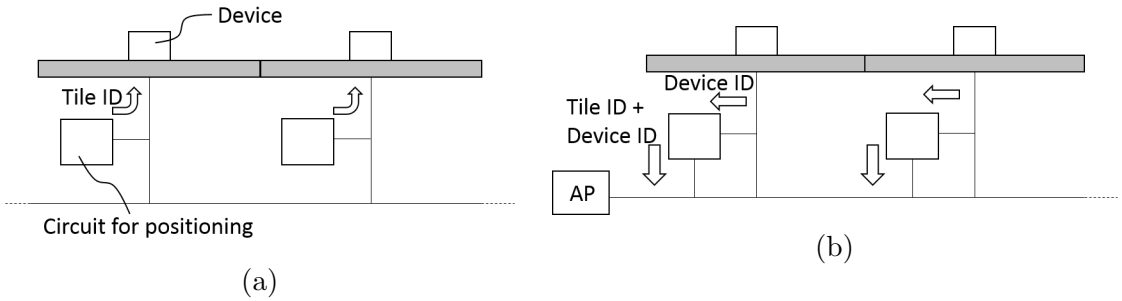

Fig. 5.2. Positioning architectures with the tile system. (a) Self-positioning. (b) Infrastructure positioning.

in Fig. 5.2 (b), signals from the device are separated into two routes and one is connected to the CP. The CP procures the device ID and transmits information of the tile ID and the device ID to the AP. Then, the AP obtain the device position. The specialized protocol is not required to the device on the tile. In this thesis, the infrastructure-positioning system is developed from the viewpoint of easiness to utilize the system.

5.4 Structure

5.4.1 Tile ID assignment

When the number of the tiles are a little, the tile-IDs can be assigned beforehand with realistic cost and the structure shown in Fig. 5.2 (b) is available. In the case of a large scale tile system, however, prior ID-assignment costs much, thus an algorithm for the assignment is necessary. In the tile system, the algorithm that the AP is required to send ID information to a specific tile that does not have an ID is possible. Under the structure in [59], such a transmission is difficult because the tiles receive identical signals. Thus an additional propagation path for ID assignment is necessary.

Fig. 5.3 shows one possible structure based on [59]. The thick line in Fig. 5.3(a) is the additional path for ID related signals. The CP receives a part of the signals from the 2DC sheet and transmits signals to the path for ID. As shown in Fig. 5.3, the AP and the CPs on the path are linked together via power splitters. When the destination tile is distant from the AP, signals are hopped by the tiles. The procedure of ID assignment is in the following. It is assumed that the number of tile is N and the IDs are from one to N.

1. The AP transmits the ID assignment signal for ID = n with hop limits of n where $n - 1 \leq N$.
2. If the CP receives the signals with hop limits of more than one, it decreases the hop limits by one and transmits the signals.
3. If the CP receives the signals with hop limits of zero, the CP recognize its tile ID = n.
4. The CP whose ID has been determined as n transmits the signal with hop limits of n-1 as an acknowledgement to the AP.
5. The AP receives the respond from the tiles, then repeat (1)-(4).
6. If the CP whose ID has not been determined yet receives the respond signal, it discards the signal.

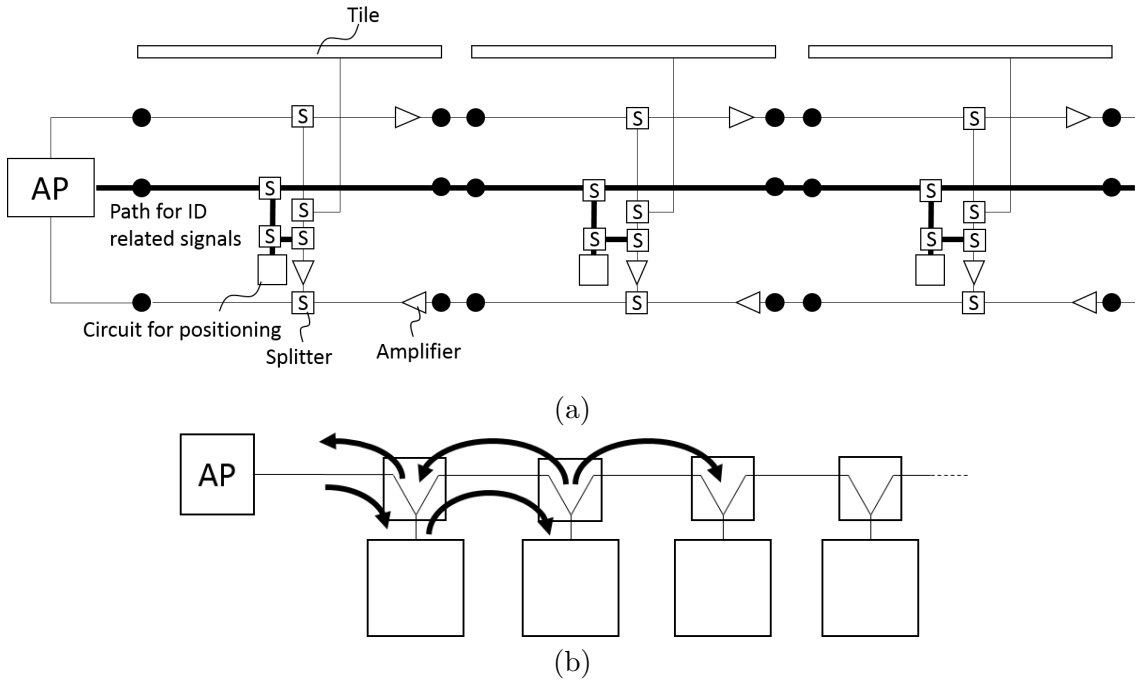

Fig. 5.3. Tile system structure with the path for ID related signals. (a). Overall structure based on [59]. The thick line indicates the additional path. (b). Connection among the AP and the CPs. The AP and the CPs are linked together via power splitters and signals are hopped by each CP when the destination tile is far from the AP. The AP assigns tile ID regularly from the tile nearer to the AP by sending tile-ID assignment request including hopping limits. The CP that receives the request responds to the AP by hopping signals, then the ID is fixed. (b) is the case of ID = 2.

5.4.2 Requirement terms

One of the evaluation criteria [71] is precision, which includes false detection. Since the AP, the tile, and the CPs are connected via power splitters, false detection would occur unless signal intensity is designed properly.

A n-port splitter splits signals to n output ports. Fig. 5.4 shows the case of $n = 2$. Although the isolation between port 2 and port 3, S23, is ideally negative infinity, it is about -20–-30 dB in practice. This fact indicates that a part of signals are propagated through an unintentional path, from one output port to the other output port. If the SNR of signals passing through the undesirable path like a red dashed line shown in Fig. 5.5 is more than the minimum receive sensitivity of a communication module, the CP in the neighboring tile successfully receives the signals and false detection is caused. Therefore, SNR of signals for position detection is necessary to be adjusted to less than

$$3\mathrm{S21} + \mathrm{S23}. \tag{5.1}$$

If this criterion allows only a low SNR, which causes high bit error rate that leads to false device-ID detection, the position detection with the tile system is not practical. Measurement of the criterion value with a preliminary setup is conducted. The measurement setup is shown in Fig. 5.6. Only the connection related to the path for ID, which is

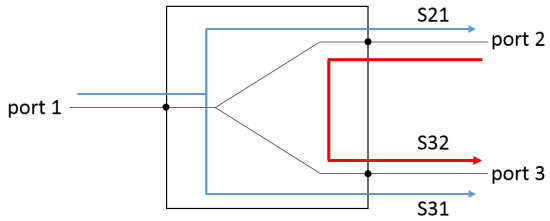

Fig. 5.4. Isolation property of a power splitter. Although the isolation S23 is ideally negative infinity, in practice S23 is −20−−30 dB. A part of the signals are propagated from port 2 to port 3 or vice versa.

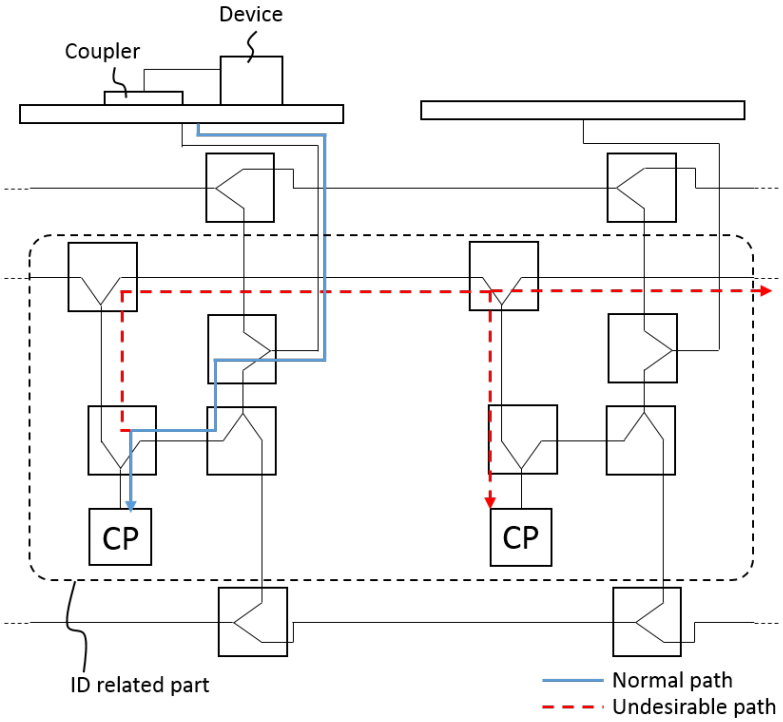

Fig. 5.5. Detailed connection of the tile system with ID signal path. Since a part of signals are propagated from one output port (port2 or port 3 in Fig. 5.4) to the other output port, an undesirable path is formed as shown in a red dahsed line. If the SNR of the signal that reaches the CP in the neighboring tile is more than a minimum receiving sensitivity, false detection is caused.

described with a dashed line in Fig. 5.5 is implemented. A power splitter manufactured by Mini-Circuits, the model number ZX10-2-98-S+, is used. The input port that is connected to the 2DC sheet is connected to port 1 of the VNA, Rohde & Schwarz ZNB-20; port 2 and port 3 of the VNA are connected to the CP and the CP in the neighboring tile, respectively. Transmittances, S21 and S31 are measured from 7.25 GHz to 10.25 GHz. Unnecessary ports are terminated.

Fig. 5.7 shows the measurement result. Since the minimum value between S21 and S31 is −27.6 dB at 10.2 GHz, the SNR of signals that propagate to the path for ID related signals is necessary to be lower than 27.6 dB. The SNR of 27.6 dB achieves sufficiently low bit error rate, 10^{-6}, with the modulation of 16 QAM. Therefore, position detection

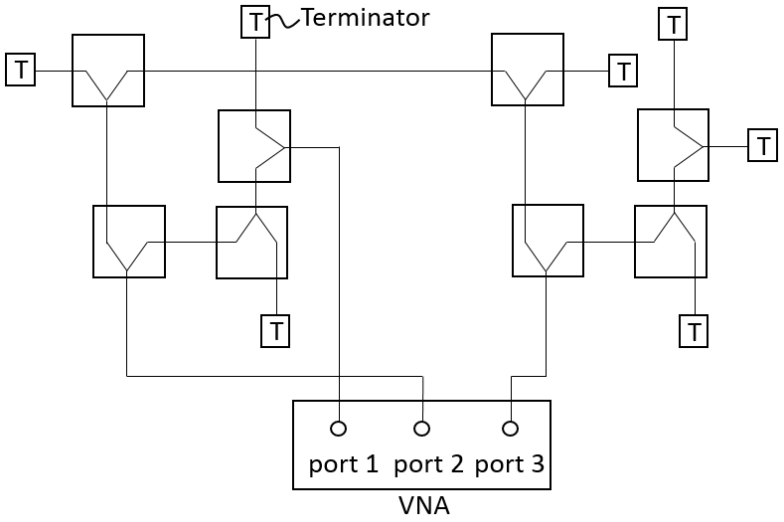

Fig. 5.6. Measurement setup. Only ID related part, which is described with the dashed line in Fig. 5.5, is implemented.

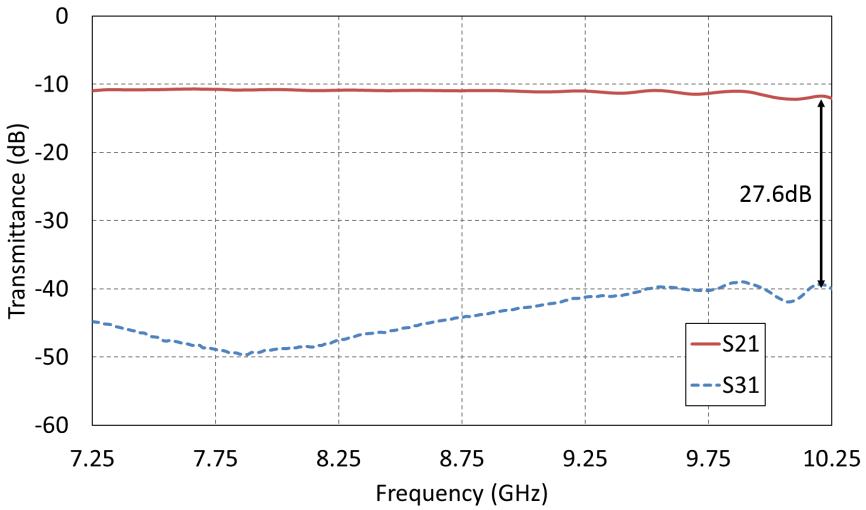

Fig. 5.7. Transmittance from the input port to the two CPs. Port 1 corresponds to the port from the tile and port2 and port 3 correspond to the CP.

with the tile system is viable. The SNR of signals transmitted from the CP also have to be lower than 25 dB to prevent hopped signals from reaching over the neighboring tile.

5.5 Experiment

The positioning method is examined to ensure the feasibility of the principle. The experimental setup consists of the AP and two tile-units without the repeater circuit and the communication path as shown in Fig. 5.8. The tile size is 50-cm square meter; the materials of the 2DC sheet is the same as that of the former section; the 2DC sheet edge is shorted with copper tapes. The experiment was conducted with 2.4 GHz signals, not UWB signals because establishment of the experimental setup is easier with 2.4 GHz

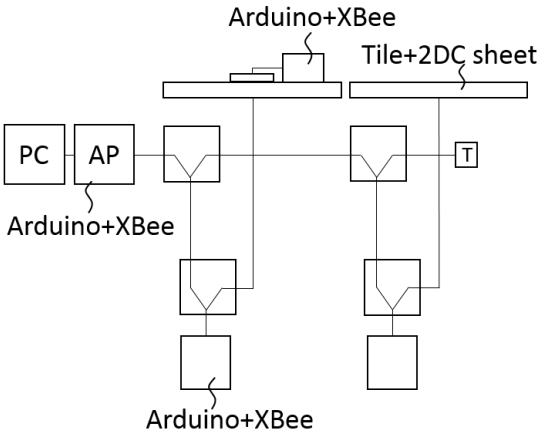

Fig. 5.8. Experimental setup.

devices. This difference is not the critical problem regarding principle verification. The coupler for 2.4 GHz [22] is employed. Arduino is used as the device on the tile, the CP, and the AP; XBee-PRO manufactured by Digi International K.K., which is a commercial wireless module operating with 2.4 GHz and operates with ZigBee protocol, is used to enable Arduinos to communicate among them with radio frequency signals.

The device on the tile transmits the signals including data and its ID to the tile by three seconds, then the CP receives the signal and transmits a signal to the AP. Finally the AP receives the signal from the CP and the PC displays both the device ID and the tile ID.

Fig. 5.9 shows the transmittances under the experimental setup from the coupler of the device to the CP in the tile where the device is put on and from the coupler to the CP of the neighboring tile. The highest transmittance of the undesirable path and the minimum difference value between the transmittance of the normal path and that of the undesirable path is −67 dB and 12.6 dB, respectively. Since output power of XBee is 10 dBm in the weakest case, the SNR of the signal reaching the neighboring circuit through the undesirable path would be −57 dB, which is higher than the receiving sensitivity of −101

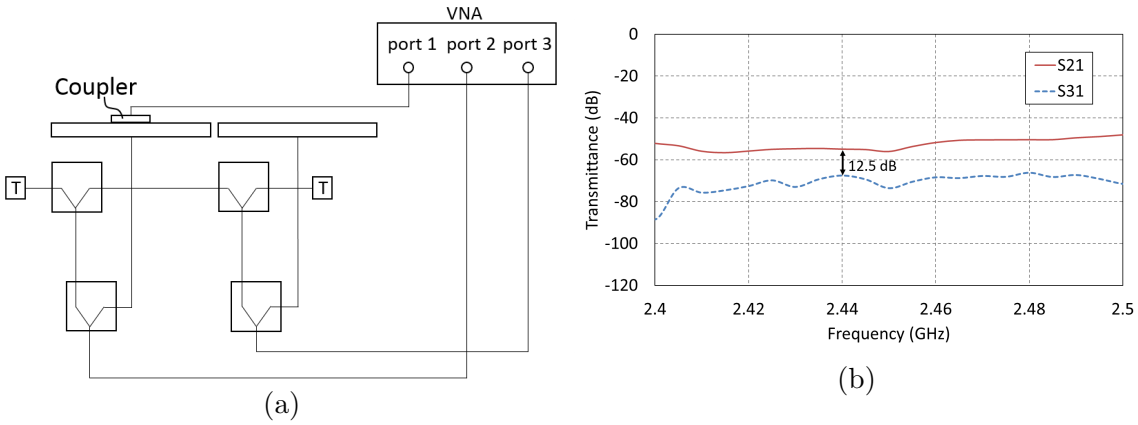

Fig. 5.9. Transmittance measurement with the experimental setup. (a). Schematic diagram of connection. (b). Measurement Result.

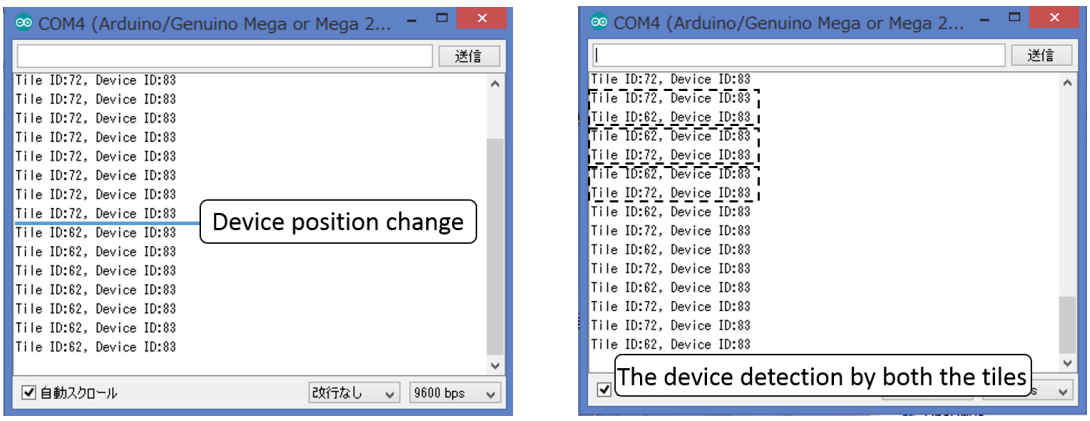

(a) (b)

Fig. 5.10. Experimental result. (a). Successful case. The tile ID changes when the device moves to the other tile. (b). Failure case. Both the tiles detect the device simultaneously.

dBm [74]. Thus the attenuator of 46 dB was equipped with the coupler to decrease the SNR of the signal at the circuit in the neighboring tile less than the receiving sensitivity.

Fig. 5.10 shows the experimental result. In the successful case, the tile system correctly detects the tile ID where the device is put on and the tile ID changes when the device moves to the other tile. On the other hand, when the attenuation at the coupler is 20 dB, that is, the SNR becomes higher than the receiving sensitivity, the two CPs detect the device simultaneously as shown in Fig. 5.10(b). Therefore, the position detection with the tile system is feasible by designing the signals intensity property.

5.6 Conclusion

In this section, we proposed the positioning method with the UWB 2DC tile system. The proposed method utilizes the physical property of the tile system that the networked area is separated regularly. The discrete position detection with the accuracy of inverse of square root of a tile length is feasible by distinguishing the tile where the device is placed on.

Since the tiles are an identical composition, a circuit for position detection is necessary to add the distinction to the tile. The requirement of the proposed method is to adjust the signal intensity to prevent the neighboring tile from receive signals from the device put on the tile. An additional signal path is also necessary to assign ID to each tile when automatic ID assignment function is necessary. The experiment indicated that the device position was successfully detected by adjusting the signal intensity properly. Therefore, the position detection with the tile system is feasible.

Chapter 6

Conclusion

In this thesis, we proposed an indoor communication system by a UWB 2DC tile. This tile system enables a 2DC network area to be freely extended by placing the tiles side by side without special skills and tools. The properties of 2DC and a shorted-edge waveguide that generates standing waves enables stable UWB communication despite low transmission power density. Moreover, high data rate and reliable communication is ensured by clarifying signal transmission properties and establishing a suppression method of radiation from the sheet. In addition, device positioning with high accuracy of the inverse of square root of a tile length is feasible.

In Chapter 2, the concept of a UWB 2DC tile was presented and factors to achieve the system was listed. Preliminary experiments showed that transmittances measured at six points on the 2DC sheet are -40 dB or more in more than 90% bandwidth of the UWB high-band. Effect of thickness is also evaluated and up to 10mm-thick dielectric layer, SNR is kept more than 20 dB. Since thickness of some commercial carpets are 6 mm, communication via the tile system is possible with a generally available material. From these results, feasibility of the tile system is ensured.

In Chapter 3, we clarified and modeled signal transmission properties of the 2DC sheet, which are necessary to design a physical layer protocol. Since a sheet shape is a precise square, propagation paths of multi-reflected signals are identified by placing imaginary sheets side by side. A RMS delay spread calculated based on the model was well matched to that of an EM simulation. Measurement results of the properties of a single tile showed that the RMS delay spread is mainly distributed from 4.2 ns to 5.76 ns. These values are shorter than that of a proposed UWB channel model of NLOS (non line-of-sight) that is inevitable in an indoor environment. Then we evaluated the delay property of the entire tile system. From signal propagation model, signals theoretically propagate at most two tiles. Numerical calculation showed that a RMS delay spread of the entire system is 1.41 times longer than that of one tile regardless of the system size. This relation is consistent with measurement results. These results enable a physical layer protocol design of the tile system. Since the delay spread value is shorter than that of aerial wireless communication, higher data rate is achievable by optimizing a symbol rate.

In Chapter 4, a suppression method for radiation from the sheet was proposed. We clarified that a magnetic field at a far-field zone corresponds to a part of a Fourier transform of an amplitude of an electric-evanescent field and an observable range is determined with the wavenumbers in space and the sheet. Therefore, decreasing intensities of the power spectrum of the amplitude over the range yields suppression of the radiation. This model shows reasonable agreement with an EM simulation. Two kinds of the amplitude transition are examined. Both transition reduce the intensities within the range. The examined cosine curved transition decreases the radiation by 30 dB when its length is 100 mm. From the results, control of the amplitude distribution suppresses the radiation and

enables reliable communication.

In Chapter 5, positioning principle with the tile system was presented. The physical property that the tile system consists of multiple separated tiles is utilized. Although the additional circuit and signal path are necessary, device positioning with the accuracy of the inverse of square root of the tile length is possible. The principle was verified with the preliminary experiment.

From these results, high-speed and reliable indoor communication system that includes positioning function is achievable with 2DC tiles. This system enables a stable communication even with the vast number of devices and can provide more convenient services.

Through the thesis, a prototype specialized coupler were used to evaluate the system. When another coupler with different properties is used, obtained data are changed from this thesis. However, the results of the thesis show that even the system that is established with the available components has favorable properties for high-speed communication and is useful as a reference for further development.

Acknowledgement

I have been given much thoughtful support from many people in my doctor course period and sincerely appreciate them. First of all, I would like to appreciate professor Shinoda's supports and instructions. He always welcomed me, patiently listened to me, and gave me proper suggestions from both the technical and broad viewpoint. His constructive commnets encourged me to progress the research. In addition, his attitude to a research and an education helped me to improve my management skill in the company I belong to.

Project assistant professor Noda also always gave me insightful and essential suggestions when discussing with me. His skill of logical thinking and sincere attitude to a research disclose weak points of my researhch and really help me to improve my thesis. It is not too much to say that I have finished the dissertation oweing to him.

I also appreciate that East Japan Railway Company provided me the opportunity to work toward Ph. D with the circumstance where I could concentrate on the research. Dr. Fukuta's support have encouraged me to research my thesis and give me the industrial viewpoint. Thank to such a precious time, I have learned expertises and improve research skills. I believed that what I learned in the doctor course period helps in various kinds of works as well as researches. My colleagues, Mr. Teramoto and Mr. Ambe have shared the works that I am originally in chage.

I also thank to Mr. Masuda, Mr. Fukui and all the Shinoda-Makino Lab. members for treating me friendly even though I am a little older than them. Discussions, talks, drinkings, and so on with them brought me much fun and spurred me to research.

I genuinely thank again all the people that supported me, Prof. Shinoda, Dr. Noda, All the Shinoda-Makino lab's members, stuffs of the University of Tokyo, my colleagues, my families and so on. I really enjoyed fruitful three-years.

Bibliography

[1] Ministry of Internal Affairs and Communications, Japan, "WHITE PAPER Information and Communications in Japan," 2015.

[2] Wi-Fi alliance, [Online]. Available: http://www.wi-fi.org/.

[3] 1394 Trade Association, [Online]. Available: http://1394ta.org/.

[4] Bluetooth, [Online]. Available: http://www.bluetooth.com/.

[5] ZigBee Alliance, [Online]. Available: http://www.zigbee.org/.

[6] Federal Communications Commission, "First report and order, revision of part15 of the commission's rules regarding ultra-wideband transmission systems," ET Docket No. 98-153, 2002.

[7] Association of radio industries and business, "ARIB STD-T91 ver. 2.0, UWB(ULTRA-WIDEBAND) RADIO SYSTEM ARIB STANDARD," Mar. 2015.

[8] P. H. Pathak, X. Feng, and P. Mohapatra, "Visible Light Communication, Networking, and Sensing: A Survey, Potential and Challenges," *IEEE Commun. Surveys Tuts.*, vol. 17, no. 4, Fourth quarter, 2015.

[9] IEEE 802.15.7 WPAN Task Group 7, [Online]: Available: http://www.ieee802.org/15/pub/TG7.html.

[10] A. Sewaiwar, P. P. Han, Y. H. Chung, "3-Gbit/s Indoor Visible Light Communications Using Optical Diversity Schemes," *IEEE Photon. J.*, vol.7, no. 6, Dec. 2015,

[11] A. T. Hussein and J. M. H. Elmirghani, "High-Speed Indoor Visible Light Communication System Employing Laser Diodes and Angle Diversity Receivers," in *Proc. 17th Int. Conf. Transparent Optical Networks*, 2015. pp. 1-6.

[12] A. Frotzscher, U. Wetzker, M. Bauer, M. Rentschler, M. Beyer, S. Elspass, and H. Klessig, "Requirements and current solutions of wireless communication in industrial automation," in *Proc. IEEE Int. Conf. communications workshops*, 2014, pp. 67-72.

[13] H. Korber, H. Wattar, and G. Scholl, "Modular Wireless Real-Time Sensor/Actuator Network for Fatory Automation Applications," *IEEE Trans. Ind. Informat.*, vol. 3, no. 2, pp. 111-119, May 2007.

[14] H. Beikirch, M. Voss, and A. Fink, "Redundancy Approach to Increase the Availability and Reliability of Radio Communication in Industrial Automation," in *Proc. IEEE Conf. Emerging Technologies and Factory Automation*, 2009, pp. 1-4.

[15] X. Chen and M. R. Lyu, "Reliability Analysis for Various Communication Scheme in Wireless CORBA," *IEEE Trans. Rel.*, vol. 54, no. 2, pp. 232-242, Jun. 2005.

[16] R. Fujiwara, M. Miyazaki, and M. Katagishi, "Low-Latency Wireless LAN System using Polling Based MAC," in *Proc. IEEE Int. Symp. Circuits and Systems*, 2014, pp. 1504-1507.

[17] M. Weiner, M. Jorgovanovic, A. Sahai, and B. Nikolie, "Design of a Low-Latency, High-Reliability Wireless Communication System for Contorol Applications," in *Proc. IEEE Int. Conf. Communications*, 2014, pp. 3829-3835.

[18] M. Jonsson, and K. Kunert, "Towards Reliable Wireless Industrial Communication With Real-Time Guarantees," *IEEE Trans. Ind. Informat.*, vol. 5, no. 4, pp. 429-442, Nov. 2009.

[19] Industrie 4.0, [Online]. Available: http://www.plattform-

i40.de/I40/Navigation/EN/Home/home.html.
[20] Industrial internet, [Online]. Available: http://www.iiconsortium.org/," ET Docket No. 98-153, 2002.
[21] Y. Kudo, A. Noda, and H. Shinoda, "UWB Sensor Network on 2-D Waveguide Sheet," in *Proc. IEEE Sensors Appl. Symp.*, New Zealand, 2014, pp. 339-342.
[22] H. Shinoda, Y. Makino, N. Yamahira, and H. Itai, "Surface Sensor Network Using Inductive Signal Tranmission Layer," in *Proc. 4th Int. Conf. Networked Sensing Syst.*, 2007, pp. 201-206.
[23] H. Shinoda, et al., "Two-Dimensional Communication Technology Inspired by Robot Skin," in *Proc. IEEE TExCRA*, 2004, pp.99-100.
[24] A. Okada, Y. Makino, and H. Shinoda, "Cell Bridge: A Signal Transmission Element for Constructing High-Density Sensor Networks," in *Proc. Int. Conf. Networked Sensing Syst.*, 2005, pp.180-185.
[25] Y. Makino, K. Minamizawa, and H. Shinoda, "Two Dimensional Communication Technology for Networked Sensing System," in *Proc. 2nd Int. Workshop Networked Sensing System*, 2005, pp. 168-173.
[26] A. Noda, and H. Shinoda, "Selective Wireless Power Transmission Through High-Q Flat Waveguide-Ring Resonator on 2-D Waveguide Sheet," *IEEE Trans. Microw. Theory Techn.*, vol. 59, no. 8, pp. 2158-2167, Aug. 2011.
[27] T. Matsuda, T. Oota, Y. Kado, and B. Zhang, "An Efficient Wireless Power Transmission System Using Phase Control of Input Electrode Array for Two-dimensional Communication," in *Proc. 13th Int. Conf. Advanced Communication Technology*, 2011, pp. 610- 615.
[28] K. Nakatsuma, H. Shinoda, "Position and Orientation Sensor for Two-Dimensional Communication Network," in *Proc. SICE Annun. Conf.*, 2010, pp.3150-3154.
[29] T. Oota, T. Matsuda, Y. Kado, and B. Zhang, "High-Accuracy Positioning Using Phase Difference of Electrode Array for Two-Dimensional Communication Sensor Network (2DCSN)," in *Proc IEEE Sensors*, 2011, pp. 786-789.
[30] R. Elliott, "On the theory of corrugated plane surfaces," *IRE Trans. Antennas Propag.*, vol. AP-2, no. 2, pp. 71-81, Apr. 1954.
[31] S. Lee and W. Jones, "Surface waves on two-dimensional corrugated surfaces," *Radio Sci.*, vol. 6, pp. 811-818, 1971.
[32] N. Kobayashi, H. Fukuda, and T. Tsukagoshi, "Challenging EMC problems on Two-Dimensional Communication Systems," in *Proc. 7th Int. Conf. Networked Sensing Syst.*, 2010, pp. 130-137.
[33] W. P. Siriwongpairat, W. Su, M. Olfatm and K. J. R. Liu, "Multiband-OFDM MIMO Coding Framework for UWB Communication System," *IEEE Trans. Signal Process.*, vol. 54, no. 1, pp. 214-224, Ju. 2006.
[34] A. F. Molisch, M. Z. Win, and J. H. Winter, "Space-Time-Frequency (STF) Coding for MIMO-OFDM Systems," *IEEE Commun. Lett.*, vol. 6, no. 9, pp. 370-372, Sep. 2002.
[35] W. Su, Z. Safar, and K. J. R. Liu, "Towards Maximum Achievable Diversity in Space, Time, and Frequency: Performance Analysis and Code Design," *IEEE Trans. Wireless Commun.*, vol. 4, no. 4, pp. 1847-1857, Jul. 2005.
[36] L. C. Tran, and A. Mertins, "Space-Time-Frequency Code Implementation in MB-OFDM UWB Communications: Design Criteria and Performance," *IEEE Trans. Wireless Commun.*, vol. 8, no. 2, pp. 701-713, Feb. 2009.
[37] Q. Zou, A. Tarighat, and A. H. Sayed, "Performance Analysis of Multiband OFDM UWB Communications With Application to Range Improvement," *IEEE Trans. Vehicular Technology* , vol. 56, no. 6, pp. 3864-3878, Nov. 2007.
[38] A. Giorgetti, M. Chiani, and M. Z. Win, "The Effect of Narrowband Interference on

Wideband Wireless Communication Systems," *IEEE Trans. Commun.*, vol. 53, no. 12, pp. 2139-2149, Dec. 2005.

[39] S. A. Alawsh, A. H. Muqaibel, "Compressive Sensing for Blind NBI Mitigation in UWB Systems," in *Proc. IEEE Int. Conf. Signal and Image Processing Applications*, 2013, pp. 441-446.

[40] S. M. Ekome, G. Baudoin, M. Villegas, and J. Schwoerer, "Narrowband Interference Mitigation in UWB Communication with Energy Detector," in *Proc. IEEE Int. Conf. Ultra-Wideband*, 2012, pp 67-71.

[41] J. Scott, F. Hoffmann, M. Addleseet, G. Mappt, and A. Hopper, "Networked Surfaces: A New Concept in Mobile Networking," *ACM Mobile Networkes and Applications*, vol.7, no. 5, pp. 353-364, Oct. 2002.

[42] J, Lifton, and J, Paradiso, "Pushpin Computing System Overview: A Platform for Distributed, Embedded, Ubiquitous Sensor Networks," *Pervasive Computing, Lecture Notes in Computer Science*, vol. 2414, pp. 139-151, 2002.

[43] K. V. Laerhoven et al., "Pin & Play: The Surface as Network Medium," *IEEE Commun. Mag.*, pp. 90-95, Apr. 2003.

[44] M. Fukumoto, and M. Shinagawa, "CarpetLAN: A Novel Indoor Wireless(-like) Networking and Positioning System," in *Proc. 7th. Int. Ubicomp*, Tokyo, Japan, 2005, pp. 1-18.

[45] T. Kurakawa, K. Takahashi, and H. Nakanishi, "Yukamen RFID sensa "interimat" no kaihatsu [Development of a mat including RFID tags named "IntelliMat"]," *IPSJ SIG Technical Report*, 2007-HCI-124, pp. 49-56, Jul. 2007.

[46] K. Eom, H. Arai, "Flexible Sheet-shaped Waveguide for Body-centric Wireless Communications," in *Proc. IEEE Radio and Wireless Symp.*, 2010, pp.76-79.

[47] Y. Kado, and M. Shinagawa, "RedTacton Near-body Electric-field Communications Technology and Its Applications," *NTT Technical Review*, vol. 8, no. 3, Mar., 2010.

[48] A. Willig, "Polling-Based MAC Protocols for Improving Real-Time Performance in a Wireless PROFIBUS," *IEEE Trans. Ind. Electron.*, vol. 50, no. 4, pp. 806-817, Aug. 2003.

[49] K. Ahamd, U. Meier, H. Kwasnicka, A. Pape, and B. Griese, "A Cognitive Radio Approach to Realize Coexistence Optimized Wireless Automation Systems," in *Proc. IEEE Conf. Emerging Technologies and Factory Automation*, 2009, pp. 1-8.

[50] S. Y. Shin, H. S. Park, S. Choi, and W. H. Kwon, "Packet Error Rate Analysis of ZigBee Under WLAN and Bluetooth Interferences," *IEEE Trans. Wireless Commun.*, vol. 6, no.8, pp. 2825-2830, Aug. 2007.

[51] H. Hayashi, "Standardization of Coexistence Management for Industrial Wireless," in *Proc. SICE Annu. Conf.*, 2014, pp. 693-696.

[52] IEC 62280, "Railway applications - Communication, signalling and processing systems - Safety related communication in transmission systems," , , Feb. 2014.

[53] T. S. Rapaport, S. Y. Seidel ,and K. Takamizawa, "Statistical Channel Impulse Response Models for Factory and Open Plan Building Radio Communication System Design," *IEEE. Trans. Commun.*, vol. 39, no. 5, pp. 794-807, May. 1991.

[54] A. F. Molisch, "Ultrawideband Propagation Channels-Theory, Measurement, and Modeling," *IEEE Trans. Vehicular Technology*, vol. 54, no. 5, pp. 1528-1545, Sep. 2005.

[55] J. Karedal, S. Wyne, P. Almers, F. Tufvesson, and A. F. Molisch, "A Measurement-Based Statistical Model for Industrial Ultra-Wideband Channels," *IEEE Trans. Wireless Commun.*, vol. 6, no. 8, pp. 3028-3037, Aug. 2007.

[56] A. Noda, and H. Shinoda, "Active Tile for Room-Size UWB 2-D Communication," in *Proc. IEEE/SICE Int. Symp. System Integration*, 2015, pp. 668-671.

[57] Y. Masuda, A. Noda, and H. Shinoda, "Contactless Coupler for 2D Communication

Tile Connection," in *SICE Annual Conference 2015*, Hangzhou, China, 2015, pp. 522-527.
[58] A. Noda, A. Okada, Y. Fukui, Y. Masuda, and H. Shinoda, "Massive Multiple Access Wireless LAN Using Ultra-Wideband Waveguide Floor Tiles," in *Proc. IEEE Annu. Consumer Communication & Networking Conf.*, 2016, pp. 279-280.
[59] Y. Fukui, A. Noda, and H. Shinoda, "UWB Wireless LAN by 2D-Communication Tile Connection," in *Proc. IEEE/SICE Int. Symp. System Integration*, 2015, pp. 801-806.
[60] CST Microwave Studio, [Online]. Available: http://www.cst.com/.
[61] A. Noda, Y. Kudo, and H. Shinoda, "Circular Planar Coupler for UWB 2-D Communication," in *Proc. IEEE Int. Conf. Ultra-Wideband*, Paris, France, 2014, pp. 467-472.
[62] A. A. M. Saleh, R. A. Valenzuela, "A Statistical Model for Indoor Multipath Propagation," *IEEE J. Sel. Areas Commun.*, vol. SAC-5, no. 2, pp. 128-137, Feb. 1987.
[63] T.Kagawa, et al., "Power Provision Scheme Considering Shadowing Effect for Two-Dimensional Communication Systems," in *Proc. 19th Asia-Pacific Conf. Communications*, 2013, pp. 525-530.
[64] A. F. Molisch, J. R. Foerster, and M. Pendergrass, "Channel models for ultrawideband personal area networks," *IEEE Wireless Commun.*, vol. 10, pp. 14-21, Dec. 2003.
[65] T.S. Rappaport, "Mobile Radio Propagation: Small-Scale Fading and Multipath," in *Wireless Communications: Principle and Practice (2nd Edition)*, Prentice Hall, 2002, pp. 202-203.
[66] H. Fukuda, N. Kobayashi, K. Nakase, and T. Tsukagoshi, "Methods for suppressing edge radiation from two-dimensional communication sheet," in *Proc. 8th INSS*, 2010, pp. 1-4.
[67] A. Noda, A. Okada, and H. Shinoda, "Radiation from surface of two-dimensional communication sheet," *IEICE Communication Expresss (ComEx), Advance Publication*, , Feb. 2016.
[68] R. F. Harrington, "Two-dimensional Radiation," *Time-Harmonic Electromagnetic Fields (Reissue),* ch. 5-7, pp. 228-230, Wiley-IEEE Press, New York, 2001.
[69] F. J. Harris, "On the use of Windows for Harmonic Analysis with the Discrete Fourier Transform," *Proc. IEEE*, vol. 66, issues. 1, pp.51-83, Jan. 1978.
[70] A. Noda, "A Study on Safe Power Transmission Using Two-Dimensional Waveguide," Ph. D. dissertation, Department of Information Physics and Computing, the University of Tokyo, Tokyo, Japan, 2013.
[71] Y. Gu, A. Lo, and I. Niemegeers, "A Survey of Indoor Positioning Systems for Wireless Personal Networks," *IEEE Commun. Surveys Tuts.*, vol. 11, no. 1, First Quater 2009.
[72] S. He, and S. H. Gary Chan, "Wi-Fi Fingerprint-Based Indoor Positioning: Recent Advances and Comparisons," *IEEE Commun. Surveys Tuts.*, vol. 18, no. 1, First Quater 2016.
[73] D. Vasisht, S. Kumar, and D/ Katabi, "Decimeter-Level Localization with a Single WiFi Access Point," in *Proceedings of the 13th USENIX Symbosium on Networked Systems Design and Implementation*, 2016, pp.165-178.
[74] Digi International K.K., Specifications of XBee [Online]. Available: http://www.digi.com/pdf/ds_xbee_zigbee.pdf.

Study on OFDM Signal Transmission with UWB 2D Communication Tile, Proceedings of IEEE/SICE International Symposium on System Integration, Dec. 2014.

Publications

Journal papers

1. A. Okada, A. Noda, and H. Shinoda, “Signal transmission properties of Ultra-wideband 2D Communication tile,” IEEE Transaction on Microwave theory and technique (submitted for publication).
2. A. Noda, A. Okada, and H. Shinoda, “Radiation from surface of two-dimensional communication sheet,” IEICE Communication Express (ComEX), Advance Publication, Feb. 2016.

Refereed conference papers

1. A. Okada, A. Noda, and H. Shinoda, “Time Domain Characteristics of Multiple UWB 2D COmmunication Tiles,” Proc. 2015 IEEE/SICE Internationay Symposium on System Integration, pp. 817-822, Nagoya, Japan. Dec, 2015.
2. A. Okada, A. Noda, and H. Shinoda, “Evaluation of Isolation Property of UWB 2DC Tile for Coexistence with Radio Signals,” Proc. 41st Annual Conference on IEEE Industrial Electronics Society (IECON), pp. 2868-2873, Yokohama, Japan, Nov. 2015.
3. A. Okada, A. Noda, and H. Shinoda, “Feasibility study on OFDM signal transmission with UWB 2D communication tile,” Proc. 2014 IEEE/SICE International Symposium on System Integration, pp. 376-380, Tokyo, Japan, Dec. 2014.
4. A. Okada, A. Noda, and H. Shinoda, “ effectof the Surface Insulator on UWB 2D-Communication Sheet,” Proc. SICE Annual COnference 2014, pp. 1966-1969, Sapporo, Japan, Sep. 2014.
5. H. Shinoda, A. Okada, and A. Noda, “UWB 2D Communication Tiles,” Proc. 2014 IEEE International conference on ultra-wideband,” pp. 1-5, Paris, France, Sep., 2014.

Domestic presentations

1. 増田祐一，野田聡人，岡田明正，福井雄大，篠田裕之，“二次元通信タイルを介した他支店カメラシステム,” 第 16 回計測自動制御学会システムインテグレーション部門講演会論文集，pp. 216-218, 2015.
2. 岡田明正，野田聡人，篠田裕之，“二次元通信媒体の電磁漏洩評価のための給電手法,” 2015 年電子情報通信学会ソサイエティ大会通信講演論文集 1, p.257, 2015.
3. 野田聡人，岡田明正，篠田裕之，“床面敷設型二次元通信のためのアクティブタイル,” 2015 年電子情報通信学会 通信講演論文集 2, p. 641, 2015.
4. 岡田明正，野田聡人，篠田裕之，“二次元通信タイルの伝送特性評価,” 2015 年電子情報通信学会総合大会 基礎・境界講演論文集, p. 166, 2015.
5. 増田祐一，野田聡人，岡田明正，牧野泰才，篠田裕之，“二次元通信タイル間接続のための近接コネクタ,” 第 15 回計測自動制御学会システムインテグレーション部門講演会論文集, pp.503-504, 2014.

Demonstrations

1. A. Noda, A. Okada, Y. Fukui, Y. Masuda, and H. Shinoda, “Massive Multiple Access Wireless LAN Using Ultra-Wideband Waveguide Floor Tiles,” Proc. the 2016, 13th Annual IEEE Consumer Communications and Networking Conference (CCNC), pp.279-280, Las Vegas, USA, Jan. 2016.
2. A. Noda, A. Okada, Y. Fukui, Y. Masuda, and H. Shinoda, “Massive Multiple Access Wireless LAN Using Ultra-Wideband Waveguide Floor Tiles,” IEEE booth of the International Consumer ELectronics Show (CES) 2016, Las Vegas, USA, Jan. 2016.
3. CEATEC JAPAN 2015.